République Algérienne Démocratique et Populaire
Ministère de l'Enseignement Supérieur et de la Recherche Scientifique
Université Ibn Khaldoun de Tiaret
Faculté des Sciences Appliquées
Département de Génie Mécanique

MÉMOIRE DE FIN D'ÉTUDES

Pour l'obtention du Diplôme de Master

Domaine : Sciences et Technologie
Filière : Génie Mécanique
Spécialité : Énergétique

Thème

THE NUMERICAL INVESTIGATION OF FULLY DEVELOPED TURBULENT FORCED CONVECTION OF OSTWALD DE WAELE FLUIDS WITHIN A CYLINDRICAL PIPE BY EMPLOYING THE DIRECT NUMERICAL SIMULATION (DNS) AND LARGE EDDY SIMULATION APPROACHES.

Préparé par :

BOUHENNI Lalia Abir
BOUHENNI Fatima Zohra Nedjda

Soutenu publiquement le : 13/06/2023, devant le Jury composé de :

MM.

HADDOUCHE Kamel	Professeur (Université de Tiaret)	Président
SAD CHEMLOUL Nord-Eddine	Professeur (Université de Tiaret)	Examinateur
KARAS Abdelkader	Professeur (Université de Tiaret)	Examinateur
CHAIB Khaled	MCA (Université de Tiaret)	Encadrant
ABDI Mohamed	Docteur (Université de Tiaret)	Co-encadrant

Année universitaire : 2022 - 2023


بسم الله الرحمن الرحيم

DEDICATION

First of all, we would like to thank ALLAH the almighty for giving us the opportunity and guidance to achieving our goal. Than, we dedicate this dissertation to our parents for their unwavering love, support, encouragement and their tireless efforts throughout our life. We thank our parents for always believing in us and for giving us strength to reach our objectives.

This dissertation is dedicated to our incredible brother Ilyes BOUHENNI, and our fantastic sister Rania BOUHENNI, and our best friend Iness BEKKI. They have been our constant source of inspiration, motivation, and support from the beginning of our academic journey. Their unwavering belief in our abilities and unconditional love have propelled us forward, even during the most challenging times. Their presence in our life have reminded us that anything is attainable with hard work and dedication.

We want to express our deepest gratitude for their invaluable feedback, insightful discussions, and unwavering encouragement. Their keen eye for detail and ability to provide constructive criticism have greatly improved the quality of this work. Their thoughtful input and perspectives have broadened our understanding of the subject matter and have pushed us to think critically.

Beyond academia, their unwavering support and belief in us have given us the strength to overcome challenges and pursue our passions relentlessly. Their presence by our side have made this journey all the more meaningful and enjoyable.

We offer special thanks to all our colleagues Nour Elhouda BELADJINE, Manel AIT YAHIA, Amina OULD MOHAMED, and Belhouari BEKHTAOUI for their exceptional contributions, encouragement, and inspiration, and their ground breaking research and innovative ideas have influenced and shaped our work.

ACKNOWLEDGMENTS

All praises to ALLAH and his blessing for the completion of this dissertation. We thank God for all the opportunities, trials and strength that have been showered on us to finish writing the dissertation.

We would like to thank our supervisor Mr. Khaled CHAIB, for his guidance throughout this project. We sincerely thank our co-supervisor Mr. Mohamed ABDI for his advice, expertise, and constant motivation. His invaluable insights and encouragement have been instrumental in shaping this dissertation. We thank Mr. Slimane BENFERHAT for his mentorship, wisdom, and support throughout our academic journey.

We would like to express our sincere gratitude and appreciation to Ms. Meryem OULD-ROUISS, Professor at the University of GUSTAVE Eiffel (France) and member of the laboratory of "Modélisation et de Simulation à Multi-Echelles $(MSME)$". Her guidance and mentorship have been instrumental in shaping our research. This work would not have been feasible without her invaluable assistance and support.

We want to express our sincere thanks to all the Jury members for accepting and to evaluate this work.

Thanks to all the Laboratory of "Modélisation et de Simulation à Multi-Echelles $(MSME)$" members for their help and for sharing their skills. We also thank all the members of the Laboratory of "Génie Electrique et des Plasmas $(LGEP)$" - University of Tiaret.

We want to acknowledge our team unwavering support and love, who have been a constant source of motivation and inspiration. Without their encouragement and understanding, this achievement would not have been possible.

ARABIC ABSTRACT

ملخص

.

يسعى البحث الحالي إلى فحص تأثيرات عدد *Reynolds* و مؤشر التدفق على السلوك الريولوجي و الكميات المتوسطة للتدفق و احصائيات الاضطراب. كما يهدف البحث أيضًا إلى التأكد من دقة و موثوقية المحاكاة الحسابية المباشرة (*DNS*) و محاكاة الدوامة الكبيرة (*LES*) للتنبؤ فيما يخص مائع (*Ostwald de Waele*) .

تم إجراء المحاكاة الحسابية المباشرة (*DNS*) لدراسة التدفق المضطرب المطور بالكامل للموائع الشبه بلاستيكية و النيوتونية و الممددة عبر اسطوانة متساوية الحرارة عند عدد *Reynolds* للمحاكاة يساوي 6500 . تم إجراء محاكاة الدوامة الكبيرة (*LES*) باستعمال النموذج الممدد لـ Smagorinsky لدراسة التدفق المضطرب المطوّر بالكامل للحمل المستقل حرارياً عبر أسطوانة في حالة ثبات. تم إجراء هذا التحقيق على مؤشرات مختلفة لسلوك التدفق وأعداد *Reynolds* عند عدد *Prandlt* ثابت. تشير نتائج المحاكاة الحسابية المباشرة (*DNS*) ومحاكاة الدوامة الكبيرة (*LES*) إلى أن زيادة مؤشر سلوك التدفق تسبب في تعزيز واضح في توليد تقلبات السرعة المحورية مما يؤدي إلى تحسين نقل تقلبات السرعة المحورية من المنطقة المجاورة للجدار نحو المنطقة المركزية. تظهر نتائج (*DNS*) أن زيادة مؤشر التدفق يحسن آلية النقل لتقلبات السرعة الشعاعية و الماسية نتيجة تقلبات السرعة المحورية والانتقال من محيط الجدار نحو المنطقة المركزية. تشير نتائج (*LES*) إلى أن مؤشر التدفق المنخفض يؤدي إلى قمع واضح في الطاقة الحركية المضطربة بسبب انخفاض توليد ونقل شدة الاضطراب لتقلبات السرعة بعيدًا عن الجدار باتجاه المنطقة العازلة.

الكلمات الرئيسية : المحاكاة الحسابية المباشرة (*DNS*) ، محاكاة الدوامة الكبيرة (*LES*) ، نموذج Smagorinsky الممدد، تدفق مضطرب، شبه بلاستيكي، نيوتوني، ممدد، حمل حراري.

ABSTRACT

The present investigation examines the influences of the Reynolds number and the flow behavior index on the rheological behavior, mean flow quantities, and turbulence. The current study also tends to ascertain the accuracy and reliability of the results predicted by DNS and LES laboratory code of Ostwald de Waele fluids flow.

A DNS has been performed to study the fully developed turbulent flow of Pseudoplastic, Newtonian, and Dilatant fluids through an isothermal pipe at a simulation Reynolds number of 6500. The finite difference scheme performed the numerical integration with second-order accuracy in space and time, and a numerical resolution of $(129 \times 129 \times 193)$ gridpoints in axial, radial and circumferential directions. A Large Eddy Simulation (LES) with an extended Smagorinsky model has been conducted to investigate the fully developed turbulent flow forced convection of thermally independent Ostwald de Waele fluids through a heated stationary pipe. This investigation has been conducted on various flow behavior indices and Reynolds numbers at a fixed simulation Prandtl number with a grid resolution of 65^3 gridpoints in axial, radial and circumferential directions, respectively, and a domain length of $20R$ in the axial direction. The DNS results show that the increased flow behavior index ameliorates the transport mechanism of the radial and tangential velocity fluctuations from the axial velocity fluctuations and the transport from the wall vicinity towards the core region. The LES results suggest that the decreased flow behavior index induces a pronounced suppression in the turbulent kinetic energy along the pipe radius due to the reduction in the generation and transport of the turbulence intensities of the velocity fluctuations far away from the wall towards the buffer region.

Keywords : DNS, LES, extended Smagorinsky model, fully developed turbulence, Pseudoplastic, Newtonian, Dilatant, forced convection.

FRENCH ABSTRACT

La présente étude s'interesse aux influences du nombre de Reynolds et de l'indice d'écoulement sur le comportement rhéologique, les quantités moyennes d'écoulement et les statistiques de turbulence. Aussi elle vise également à vérifier la précision des résultats prédits par les codes DNS et LES lors de l'écoulement du fluide d'Ostwald de Waele. DNS a été utiliseé pour étudier l'écoulement turbulent pleinement développé de fluides Pseudo-plastiques, Newtoniens et Dilatants à travers un cylindre chauffé à un nombre de Reynold égale 6500. Le schéma de différences finies a permis l'intégration numérique avec une précision du second ordre dans l'espace et le temps, et une résolution numérique de $(129 \times 129 \times 193)$ points de grille dans les directions axiale, radiale et circonférentielle. Une simulation à grands échelles (LES) avec un modèle de Smagorinsky étendu a été menée pour étudier la convection forcée des fluides d'Ostwald de Waele thermiquement indépendants à travers un cylindre stationnaire chauffé. Cette étude a été menée sur différents indices d'écoulement et nombres de Reynolds avec une résolution numérique de 65^3 points de grille dans les directions axiale, radiale et circonférentielle avec une longueur du domaine de $20R$ dans la direction axiale. Les résultats obtenus par DNS montrent que l'augmentation de l'indice d'écoulement améliore le mécanisme de transport des fluctuations des vitesses radiale et tangentielle à partir des fluctuations de la vitesse axiale et le transport à proximité de la paroi vers la région centrale. Les résultats issus de l'approche LES suggèrent que la diminution de l'indice d'écoulement induit une suppression prononcée de l'énergie cinétique turbulente le long du rayon du cylindre en raison de la réduction de la génération et du transport des intensités de turbulence des fluctuations de vitesse loin de la paroi vers la région tampon.

Mots clés : DNS, LES, étendue de Smagorinsky, turbulence pleinement développée, Pseudo-plastique, Newtonien, Dilatant, convection forcée.

CONTENTS

FIGURES LIST

TABLES LIST

NOMENCLATURE

SYMBOLS

A	Area	$[m^2]$
C_p	Specific heat	$\left[J.\ kg^{-1}.K^{-1}\right]$
D	Pipe diameter	$[m]$
e	Gap	$[m]$
F	Steady-shear force	$[N]$
G	Shear elasticity modulus	$[Pa]$
K_t	Consistency index	$[Pa.s^{-n}]$
K	Turbulent kinetic energy	$[J]$
L	Domain length	$[m]$
N	Rotation rate $N = \Omega R/U_b$, with Ω is rotation velocity	
n	Flow behaviour index	
n_f	Degrees of freedom	
P	Pressure	$[Pa]$
q_W	Imposed flux at the wall	$[W.m^{-2}]$
R	Pipe radius	$[m]$
T	Fluid temperature	$[K]$
Tp	Wall temperature	$[K]$
T_{ref}	Reference temperature	$[K]$

T_τ	Friction temperature	$[K]$
t	Time	$[s]$
U_b	Mean axial velocity	
U^+	Mean axial velocity in wall units	
U_τ	Friction velocity	
U_i	Generic notation for the dimensionless velocity components	
U_{cL}	Axial velocity at the centre of the laminar analytical solution	
V	Velocity	$[m.s^{-1}]$

Greek symbols

α	Thermal diffusivity $\alpha = \lambda/\rho C_P$, with λ is thermal conductivity	$[m^2.s^{-1}]$
α_t	Turbulent diffusivity	$[m^2.s^{-1}]$
$\dot{\gamma}$	Shear-rate	$[s^{-1}]$
η	Apparent viscosity of the fluid	$[Pa.s]$
η_W	Apparent viscosity of the fluid at the wall	$[Pa.s]$
η_k	Length of Kolmogorov scale	$[m]$
ν_t	Turbulent viscosity	$[m^2/s]$
Θ	Dimensionless temperature	
ρ	Density	$[kg.m^{-3}]$
μ	Dynamic viscosity	$[Pa.s]$
ν	Kinematic viscosity	$[m^2/s]$
τ	Shear-stress	$[Pa]$
τ_W	Wall shear-stress $\tau_W = (D/4\ )\,\partial p/\partial z$	$[Pa]$
τ_0	Shear threshold	$[Pa]$
ε	Dissipation rate	$[m^2/s^3]$

Dimensionless numbers

Re	Reynolds number
Re_s	Simulation Reynolds number
Pr_s	Simulation Prandtl number

Pr	Prandtl number
Pr_t	Turbulent Prandtl number
Y^+	Wall distance $Y^+ = yU_\tau/\nu$
P_n	Pearson number $P_n = bT_{ref}$

Exhibitors

$\langle(.)\rangle$	Mean statistic
$(.)'$	Fluctuation
$(.)^+$	Normalized
$\overline{(.)}$	Filtered

Indexes

r, θ, z	Radial, circumferential and axial directions
c	Centre
L	Laminar
W	Wall
d	Dimensionless
s	Simulation

Abbreviations

DNS	Direct Numerical Simulation
LES	Large Eddy Simulation
SGS	Sub-Grid Scale
RMS	Root Mean Square
CFL	Current Friedrichs and Lewy state
QI	Quasi-Isotropic model
IP	Isotropisation of Production model
$IP-C$	Pressure-strain model

GENERAL INTRODUCTION

GENERAL INTRODUCTION

Turbulence is a complex phenomenon that occurs in many natural and artificial systems. It refers to a state of fluid flow in which the fluid motion is irregular and chaotic, with fluctuations in velocity, pressure, and other fluid properties occurring seemingly randomly. Turbulence can be observed in various contexts, from airflow over an aeroplane wing or river water movement to fluids in a chemical reactor or plasma dynamics in a fusion device. The study of turbulence is important in many fields of science and engineering, including fluid mechanics, meteorology, oceanography, and aerospace engineering. This complexity makes turbulence difficult to predict and model accurately, and it remains one of the major unsolved problems in physics and engineering. Turbulence can significantly improve the efficiency and performance of many systems, from aircraft engines to chemical reactors. Understanding the nature and behaviour of turbulent flow is important in many fields, including fluid mechanics, engineering, and physics.

Today DNS and LES have become an important tools for the turbulence research community. DNS and LES can provide accurate, complete, and detailed data, especially in the near-wall regions and/or separation regions. Despite improvements in experimental techniques, it is still difficult for experimental methods to get reliable data for certain variables, especially, for compressible flows. For example applying the DNS tool to flows of non-Newtonian fluids allows the rheology model to be treated with certainty.

For this dissertation, the first investigation devote to a Direct Numerical Simulation (DNS) of the fully developed turbulent flow of Ostwald de Waele fluid through an isothermal axially stationary pipe over the range of flow behaviour indices (0.75 to 1.2) and Reynolds number equal to 6500. Computations are carried out by a finite difference scheme with second-order accurate in space and time. The numerical resolution is $(129 \times 129 \times 193)$ gridpoints in radial,

tangential, and axial directions, respectively, with a domain length of $20R$.

The second study of this thesis report on the large eddy simulation (LES) with Smagorinsky extended model to investigate numerically the fully developed turbulent forced convection heat transfer of thermally independent Ostwald de Waele fluids through axially stationary pipe over the range of flow behaviour indices (0.75 to 1.6) and Reynolds numbers (4000 to 12000) at a fixed Prandtl number equal to 1. Uniform heat flux is imposed on the wall as a thermal boundary condition with an adequate grid resolution of 65^3 gridpoints in the streamwise, radial and spanwise directions, respectively, and a computational length of $20R$ in the streamwise direction.

Dissertation organization

CHAPTER 1 relates the rheological properties and classification of fluids as well as analog models that reflect the main behaviors (elastic, viscous and plastic). This chapter also provides a further understanding of turbulence phenomenon by presenting its characteristics

CHAPTER 2 concern the modeling of the turbulence phenomenon and the numerical procedures adopted in our study. In addition, it provides a comprehensive overview of the research on fluid flow through stationary and rotating pipes and explores various numerical approaches and techniques to predict turbulent flow, such as Direct Numerical Simulation (DNS) and Large Eddy Simulation (LES).

CHAPTER 3 analyses and discusses the DNS results of the turbulent flow of the Ostwald de Waele fluids through an isothermal pipe.

CHAPTER 4 analyses and discusses largely the emerged LES results of the forced convection turbulent flow of the thermally independent Ostwald de Waele fluids through a uniform heated pipe.

Finally, the conclusions are drawn from the findings of the research work, and recommendations for future work are made.

CHAPTER I

GENRALITY ON RHEOLOGY AND TURBULENCE

- Rheological properties
- Rheological classification of fluids
- Turbulence phenomenon



GENERALITY ON RHEOLOGY AND TURBULENCE

I

What is rheology ?

Rheology is the study of how materials deform and flow under the influence of external forces. The name rheology, from the Greek word rheo (= flow), was suggested by M. Reiner and E. C. Bingham, who are considered the founders of this scientific discipline. Rheological studies are important in the manufacture and applications of plastic materials, lubricating materials, coatings, inks, adhesives, food, pharmaceuticals, cosmetics, and toiletries.

Rheology is now well established as the science of the deformation and flow of matter. It is the study of the manner in which materials respond to applied stress or strain. All materials have rheological properties, which are established by rheometers [1] .

The rheological flow behaviour of any fluid is explained in terms of the relationship between shear-stress (τ) and shear-rate $(\dot{\gamma})$. The shear-stress is defined as the tangential force applied per unit area and the shear-rate is stated as the change of shear strain per unit time. The ratio of shear-stress to shear-rate is known as dynamic viscosity (μ), which can also be defined as a measure of resistance offered by the adjacent layers to one another during the flow of fluid. The fluid behavior can be categorized as Newtonian and non-Newtonian. For Newtonian behavior, the viscosity remains constant with shear-rate and the stress exhibits linear relation with shear-rate while for non-Newtonian behavior, the viscosity may vary with shear-rate [2].

I.1 Rheological properties of fluids

Dynamic viscosity (μ) is just one of several rheological properties that can be used for material characterisation in engineering application purposes. To define viscosity, consider an element of fluid sandwiched between two parallel plates of area (A), separated by a gap (e), being subjected to a steady-shear force (F) on its upper face (see Figure I.1).

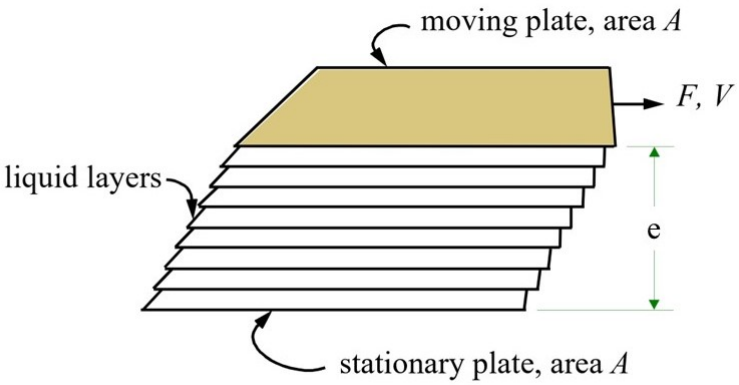

Figure I.1 – Fluid under steady-shear [3].

The steady-shear force will cause the upper plate to move with a velocity (V), relative to the lower plate. The element is said to be under a shear-stress (τ) and flows. The shear-stress is given by :

$$\tau = \frac{F}{A} \tag{I.1}$$

With a shear-rate :

$$\dot{\gamma} = \frac{V}{e} \tag{I.2}$$

Dividing the shear-stress by the shear-rate gives a measure of the resistance of the fluid to flow, that is its dynamic viscosity, defined as :

$$\mu = \frac{\tau}{\dot{\gamma}} \tag{I.3}$$

The viscosity is usually derived from the flow curve : plotting the ratio of shear-stress to shear-rate as a function of shear-rate will result in a viscosity curve. Instruments that measure viscosity are referred to as viscometers ; those measuring other rheological properties in addition to viscosity are known as rheometers [3].

I.2 Rheological classification of fluids

I.2.1 Newtonian fluids

Consider a thin layer of a fluid contained between two parallel planes a distance dy a part,

as shown in Figure I.2. Now, if under steady state conditions, the fluid is subjected to a shear by the application of a force (F) as shown, this will be balanced by an equal and opposite internal frictional force in the fluid. For an incompressible Newtonian fluid in laminar flow, the resulting shear-stress (τ) is equal to the product of the shear-rate $(\dot{\gamma})$ and the viscosity of the fluid medium. In this simple case, the shear-rate may be expressed as the velocity gradient in the direction perpendicular to that of the shear force.

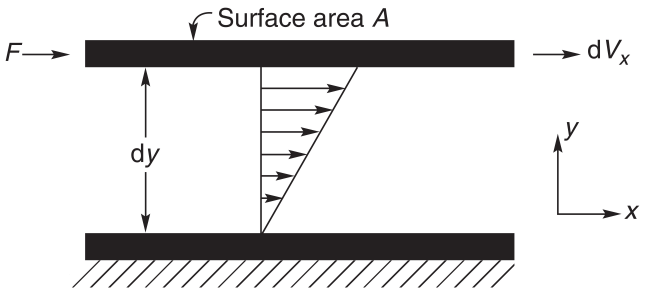

Figure I.2 – Simple shear of a Newtonian fluid between two parallel planes [4].

The ratio of the shear-stress to the shear-rate is called the Newtonian viscosity (μ). It is independent of shear-rate $(\dot{\gamma})$ or shear-stress (τ) and depends only on the material at given temperature and pressure. A plot of shear-stress (τ) and shear-rate $(\dot{\gamma})$, called the "flow curve" or rheogram, for a Newtonian fluid is therefore a straight line with a slope (μ) passing through the origin. The single constant (μ) completely characterises the flow behavior of a Newtonian fluid at a fixed temperature and pressure (Chhabra and Richardson, 2008), Equations I.2, I.3 [4].

I.2.2 Non-Newtonian fluids

More often in nature, a fluid will possess more than a single type of stress response. A fluid is deemed complex if it exhibits multiple types of behaviors. While this definition is largely vague, most complex fluids can be regarded as twofold ; a complex fluid usually exhibits two types of behaviors, such as a solid-liquid or liquid-gas mixtures. Modeling the dynamics of flow in complex fluids is convoluted due to the coexistence of multiple matter phases, and nonlinear effects may arise from the interaction between matter phases. In optical microrheology, micro-particles are used to track flows in complex fluids to better understand the microfluidics created by the interaction of multiple matter phases [5]. The role of state variables in the extended fluid mechanics that is suitable for complex fluids play the hydrodynamic fields supplemented with additional fields or distribution functions that are chosen to characterize the internal structure. In general, a different internal structure requires a different choice of the additional fields. The

state variables (called hydrodynamic fields) chosen in fluid mechanics are [6] :

$$x = x\left(\rho(\vec{r}), e(\vec{r}), u(\vec{r})\right) \tag{I.4}$$

I.2.2.1 Time-independent fluids

Time-independent fluids are those for which the rate of shear $(\dot{\gamma})$ at a given point is only dependent upon the instantaneous shear-stress (τ). The flow behavior of this class of materials can be described by a constitutive relation of the form :

$$\tau = f(\dot{\gamma}) \tag{I.5}$$

A Newtonian fluid is just a special case of a time-independent fluid where the function $f(\dot{\gamma})$ is linear at a given pressure and temperature. All fluids for which the function $f(\dot{\gamma})$ is not linear through the origin are time-independent non-Newtonian fluids [7].
Pseudoplastic and dilatant fluids can be described mathematically by the empirical Ostwald de Waele model, given by the following equation :

$$\tau = K_t \dot{\gamma}^n \tag{I.6}$$

The variables (K_t) and (n) are curve fitting parameters known as the fluid consistency index (K_t) and the flow behavior index (n).
Generally, the power-law model applies only over a limited range of shear-rates, and the fitted values of (K_t) and (n) depend on the range of shear-rates considered. The apparent viscosity η is given by [4] :

$$\eta = K_t \dot{\gamma}^{n-1} \tag{I.7}$$

I.2.2.1.a Pseudoplastic fluids

The majority of non-Newtonian fluids are to be found in this category. Those fluids are characterized, that they have no yield stress and that the apparent viscosity decreases with increasing shear-rate. The decreasing of the apparent viscosity occurs due a structure change in the fluid, so that the individual fluid-particles can be better slid along each other. Examples of Pseudoplastic fluids are biological fluids, paint, polymer solutions, and mayonnaise.

I.2.2.1.b Dilatant fluids

Dilatant fluids are similar to Pseudoplastic fluids in that they have no yield stress, but their apparent viscosity increases with increasing shear-rate. The increasing of the apparent viscosity in the case of suspensions occurs due a structure change in the fluid. This has the effect that individual fluid-particles interact stronger with each other, which results in increased friction and higher shear-stresses. The power-law model (but with n greater than 1) can be used for the mathematical description. Examples of materials with a dilatant flow behavior are starch, potassium silicate, many suspended solids such as mica and powdered quartz, iron powder in low viscosity liquids. The following figure show the flow behavior of Independent-time fluids.

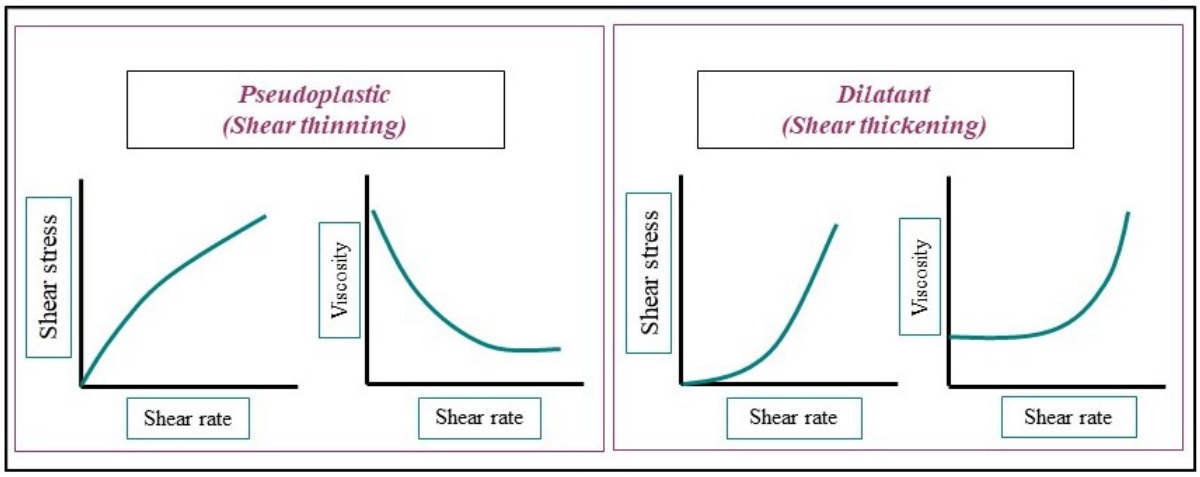

Figure I.3 – Flow behavior of Independent-time fluids.

I.2.2.2 Viscoplastic fluids

Viscoplastic fluids are characterized by their ability to sustain shear-stresses where a certain amount of stress must be exceeded before the flow initiates [8].

I.2.2.2.a Bingham plastic model

The Bingham plastic model is written as :

$$\begin{aligned} \tau &= \tau_0^B + \mu_B(\dot{\gamma}) \text{ for } |\tau| > \left|\tau_0^B\right| \\ \dot{\gamma} &= 0 \text{ for } |\tau| < \left|\tau_0^B\right| \end{aligned} \tag{I.8}$$

I.2.2.2.b Herschel-Bulkley model

A simple generalization of the Bingham plastic model to embrace the non-linear flow curve

$\left(\text{for } |\tau| > \left|\tau_0^B\right|\right)$ is the three constant Herschel–Bulkley fluid model. In one dimensional steady shearing motion, it is written as :

$$\begin{aligned} \tau &= \tau_0^H + K_t(\dot{\gamma})^n \text{ for } |\tau| > \left|\tau_0^H\right| \\ \dot{\gamma} &= 0 \text{ for } |\tau| < \left|\tau_0^H\right| \end{aligned} \tag{I.9}$$

I.2.2.3 Time-dependent fluids

These fluids are very difficult to model. Their behavior is such that for a constant shear-rate $\dot{\gamma}$ and at constant temperature the shear-stress τ either increases or decreases monotonically with respect to time, towards an asymptotic value $\tau(\dot{\gamma})$. The fluids regain their initial properties sometime after the shear-rate has returned to zero. The Time-dependent fluids are divided into two subgroups :

- **Thixotropic fluids :** At a constant shear-rate the shear-stress decreases monotonically.
- **Rheopectic (Antithixtropic) fluids :** At a constant shear-rate the shear-stress increases monotonically. These fluids are also called antithixotropic fluids [9].

The following figure summarizes the rheological classification of fluids.

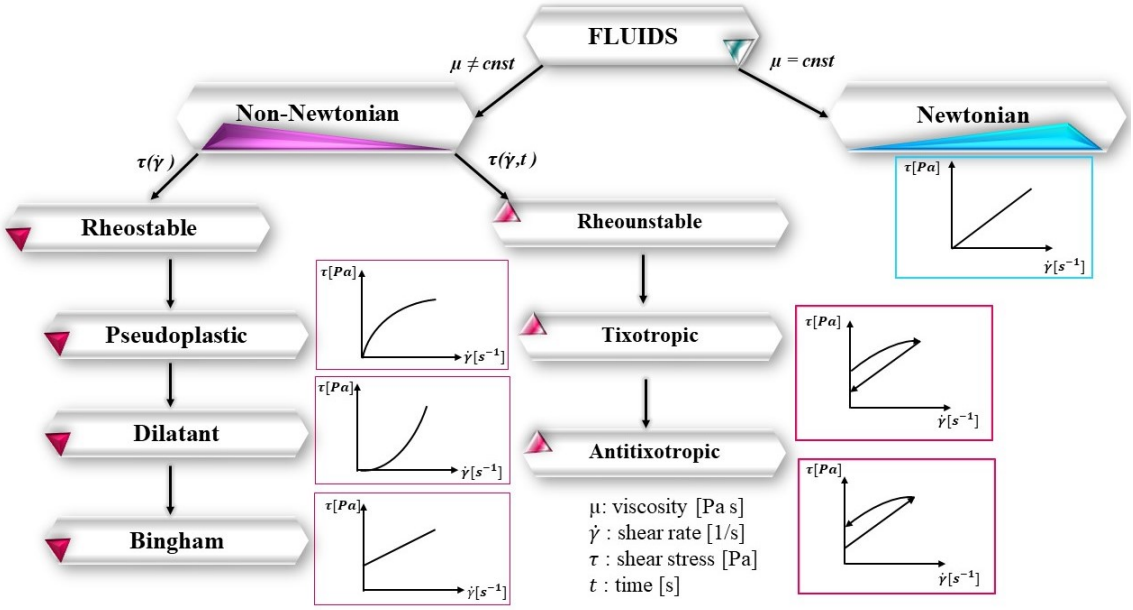

Figure I.4 – Rheological classification of fluids.

The following table present the definition of various types of non-Newtonian fluids with examples.

Type of fluid	Definition	Examples
Pseudoplastic	Fluids that depict a decrease in viscosity with increasing shear-rate and hence often referred to as shear-thinning fluids	Blood Filled polymer systems Polymer solutions Printing inks
Dilatant	Fluids that depict an increase in viscosity with increasing shear-rate and hence often referred to as shear-thickening fluids	Aqueous suspension of titanium dioxide Gum solutions Wet sand
Bingham	Fluids that do not flow unless the stress applied exceeds a certain minimum value referred to as the yield stress and then show linear shear-stress versus shear-rate relationship	Certain asphalts and bitumen Jellies Sewage sludges Thickened hydrocarbon greases Tomato ketchup Toothpaste
Pseudoplastic with a yield stress	Fluids that have nonlinear shear-stress versus shear-rate relationship in addition to the presence of yield stress.	Heavy crude oils with high wax content Filled polymer systems
Thixotropic	Fluids that exhibit the reversible decrease in shear-stress with time at a constant rate of shear and fixed temperature. The shear-stress, of course, approaches some limiting value	Coal-water slurries Crude oils Drilling muds Filled polymer systems Mayonnaise Salad dressing Yoghurt
Rheopectic	Fluids exhibit a reversible increase in shear-stress with time at a constant rate of shear and fixed temperature. At any given shear-rate, the shear-stress increases to approach an asymptotic maximum value	Some clay suspensions
Viscoelastic	Fluids that possess the added feature of elasticity apart from viscosity. These fluids exhibit process properties which lie in-between those of viscous liquids and elastic solids	Filled polymer systems Polymer melts Polymer solutions

Table I.1 – Various types of non-Newtonian fluids [3].

I.2.3 Analogic behavior models

I.2.3.1 Viscous behavior

The spring is considered representative of a linear elastic solid that obeys Hooke's law ; a viscous material can be modeled using a dashpot which obeys Newton's law. A dashpot is mechanical device consisting of a plunger moving through a viscous Newtonian fluid.

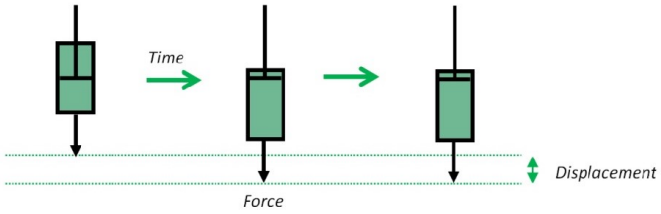

Figure I.5 – Response of an ideal liquid (dashpot) [10].

When a stress (or force) is applied to a dashpot, the dashpot immediately starts to deform and goes on deforming at a constant rate (strain rate) until the stress is removed. The energy required for deformation or displacement is dissipated within the fluid (usually as heat) and the strain is permanent [10].

I.2.3.2 Elastic behavior

Structured fluids have a minimum (equilibrium) energy state associated with their 'at rest' microstructure. This state may relate to inter-entangled chains in a polymer solution, randomly ordered particles in a suspension, or jammed droplets in an emulsion. Applying a force or deformation to a structured fluid will shift the equilibrium away from this minimum energy state, creating an elastic force that tries to restore the microstructure to its initial state. This is analogous to a stretched spring trying to return to its undeformed state.

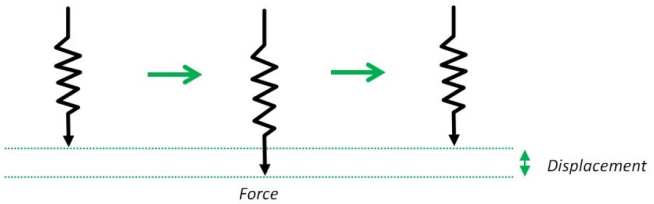

Figure I.6 – Response of an ideal solid (spring) [10].

I.2.3.3 Viscoelastic behavior

Two basic ingredients are used :

* **spring :** according to Hooke's law, the strain $(\dot{\gamma})$ is proportional to the applied stress (τ), which reads.

$$\tau = G\dot{\gamma} \tag{I.10}$$

Physically, elastic elements represent the possibility of storing energy. This storage can be achieved by different processes (e.g., polymer recoil).

* **dashpot :** the response of the dashpot, the plunger of which is pushed at the velocity $(\dot{\gamma})$ is :

$$\tau = \mu\dot{\gamma} \tag{I.11}$$

Physically, dashpots represent dissipative processes that occur as a result of the relative motion between molecules, particles, or polymer chains. This motion induce friction when there is contact between elements or viscous dampening if there is an interstitial fluid [11].

I.2.3.4 Plastic behavior

Skate (or Saint-Venant element) : this analogical model represents the rigid solid perfectly plastic ; it introduces nonlinearity into models and describes a plastic behavior (irreversible deformation) used for threshold fluids. The applied stress must exceed a plasticity threshold (also called threshold of deformability, friction, flow stress) to obtain a displacement.

Figure I.7 – Saint-Venant element.

What is turbulence ?

More than one century of experience has shown that the turbulence problem is inconveniently difficult. Though conceptually simple, the turbulence problem is an unsolved problem of classical physics. In other words, no simple analytical theory completely describes the physics of turbulence. Instead, engineers and scientists rely on the ever-increasing power of digital computers to model or simulate turbulence for a given application to calculate the relevant properties of turbulent flows [12]. For engineering applications, the diffusivity of turbulence is an important factor. The diffusivity leads to rapid mixing, increasing transfer rates of momentum, heat and mass through the flow domain. For example, turbulence can delay boundary layer separation on aerofoils at large angles of attack, increase heat transfer rates, provide resistance to flow in ducts, increase momentum transfer between currents, and so on [13].

I.3 Turbulence phenomenon

I.3.1 Turbulence understanding

Over the last 10 to 120 years, there have been huge changes in our understanding of the processes which lead from laminar flow to turbulence, processes now beginning to produce results directly impinging on our symposium objective of assessing fluxes. These changes first came about through increased awareness that the theory of linear stability, which had succeeded in describing the early stages of instability, was inadequate when looking further, particularly, when one was concerned with turbulence and its onset. A fundamental change came with the recognition that dynamical systems having a very limited number of modes of incommensurate frequency could exhibit a chaotic motion [14].

Man has evolved within a world where air and water are, by far, the most common fluids encountered. The scales of the environment around him and of the machines and structures his ingenuity has created mean that, given their relatively low kinematic viscosities, the relevant global Reynolds number, associated with the motion of both fluids is in most cases, sufficiently high that the resultant flow is of the continually time-varying, spatially irregular kind we call turbulent. However, our Reynolds number is chosen not by the overall physical dimension of the body of interest. [15].

Turbulence, the pseudo-random and apparently unpredictable state of a fluid, is one of the most challenging problems in fluid dynamics. Turbulent flows show a marked increase in mixing and friction ; predicting these phenomenon is of great importance in practical engineering applications. Consequently, numerous scientists have invested much effort in observing, describing, and understanding turbulent flows. One of the first attempts at quantifying turbulence was made by Reynolds, who showed that the flow regime changes from its orderly laminar state to a turbulent one when a critical parameter (Reynolds number) is exceeded. Another important discovery was that turbulent flows incorporate a hierarchy of eddies or whirls, which range from large scales to very small in size. Energy is transferred between these scales, generally from the larger to the smaller, until the smallest scales are finally dissipated into heat by molecular viscosity. The Russian scientist Kolmogorov formulated this energy cascade theory into physical laws for the various scales present in a turbulent flow [16].

Turbulent flows always occur at a large Reynolds number and often originate as the instability of laminar flows with increasing Reynolds numbers. Turbulent flows are rotational and three-dimensional. High levels of fluctuating vorticity characterise them. An important vorticity maintenance mechanism is 'Vortex stretching', not exhibited by two-dimensional flows, and hence turbulent fluctuations are essentially three-dimensional vorticity fluctuations. All turbulent flows are inherently dissipative. Dissipation is the deformation work of the viscous stresses, which increases the internal energy at the expense of the kinetic energy of the turbulence. Turbulent flows require a continuous energy supply, failing which the turbulence decays rapidly. Turbulence is a continuum phenomenon governed by the equations of fluid mechanics. Even the smallest scales in any turbulent flow are much larger than any molecular length scale [13].

I.3.2 Turbulence structure

One approach towards understanding turbulence is to attempt to break the complex, random field of turbulent motions into elementary recurring motions, which can then be considered as the key building-blocks or components of the turbulent flow. These motions are somewhat loosely and variously referred to as eddies, organised motions or coherent structures, and they have been the focus of many studies for over four decades (Townsend 1976 ; Cantwell 1981 ; Hussain 1986 ; Adrian 2007). This resembles the atomistic approach, which has enjoyed enormous success in chemistry and physics. But it is clear that it cannot be so simple when applied to continuous, random fluid motions, especially when they range over many scales. The difficulty presents itself in the very first step of defining what exactly constitutes an eddy or a coherent

structure, and it must be confessed that here there are no unequivocal definitions [17].

In most turbulent flows energy is transferred from the mean flow to the turbulence at the largest scales been refined by Onsager and Kolmogorov, amongst others. Richardson suggested that the energy transfer takes place in the form of (what is now called) a cascade of energy. The word cascade (probably first introduced in this context by Onsager) is meant to imply that the energy flux takes the form of a long chain of intertial transfers. That is to say, energy is first passed from the largest vortices to slightly smaller eddies, say from scale ℓ_0 to scale ℓ_1. The vortices of scale 1 then transfer some of their energy to slightly smaller vortices of size ℓ_2, where ℓ_2 is some fraction of ℓ_1 . And so, it goes on, with energy being passed down through a hierarchy of scales until, finally, we reach the microscale where the kinetic energy is converted into heat [18].

I.3.3 Characteristics of turbulence

- **Randomness :** Turbulent flow is unpredictable because small random perturbations during a particular period are amplified to that level. After a certain period of time, deterministic prediction of further development becomes impossible. This fact could seem to conflict with the fact that turbulent flow is described in thorough detail by Navier-Stokes equations, which are of a deterministic character.

- **Diffusivity :** Mixing of transported scalar quantities occurs relatively more quickly than during molecular diffusion. This characteristic obviously has important practical consequences, and turbulence is characterized by an increase in the mixing of fluids. The intensity of this mixing can be several orders of magnitude greater than mixing occurring due to molecular diffusion.

- **Vorticity :** Turbulent flows are characterized by high local values of vorticity related to the presence of Vortex structures. The field of vorticity is generally non-homogeneous and changes dynamically in time. Vortex structures tend to be called coherent vortices or, more generally, coherent structures.

- **Scale spectrum :** Vortex structures, which occur spontaneously in a turbulent flow field, are characterized by a wide scale of length measuring units. Their size is limited from the top by the dimensions of the shear areas in which they occurred and from the bottom by the size of vortices subject to dissipation in direct connection with the fluid viscosity.

Thus, the size of the structures is characterized by a dense spectrum typical for fractals. Related to this is that the turbulent flow field can be characterized as a dynamical system with a "very high" number of degrees of freedom.

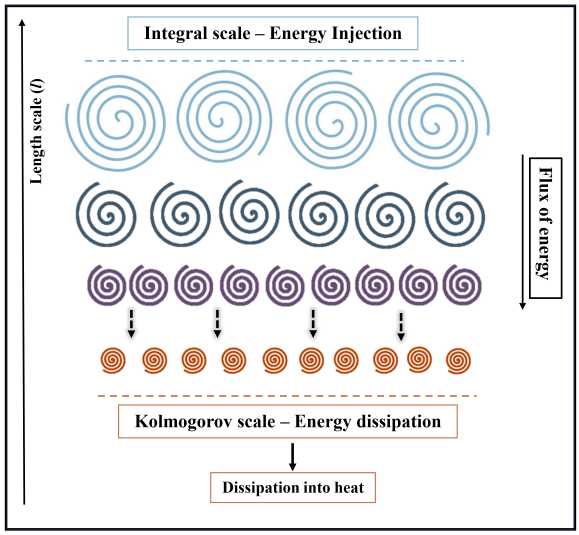

Figure I.8 – Energy cascade.

- **3D structure :** Vortex structures occur in the space of a turbulent flow field in random locations and with random orientation. The $3D$ structure of the vector field of velocity fluctuations originates from this situation. During certain boundary conditions, structures greater than a certain limit size can be spatially arranged ; for example, they can have a planar character.

- **Dissipation :** Turbulence is a dissipative process, which means that the kinetic energy of the motion of a fluid is dissipated at the level of small vortices and changes to heat. Therefore, for turbulent flows to be conserved over the long term, it is necessary to supply energy to the system from outside. This is done in the area of large scales ; energy is collected from the mainstream. The energy is then transferred towards smaller scales with the help of cascade transfer.

- **Non-linearity :** Turbulent flows are non-linear, and their occurrence is conditioned on applying non-linearities when small perturbations grow. The development and interaction of individual structures in the turbulent flow field can be described only with a non-linear mathematical model. Turbulence theory states that the eddies also vary in size. This is illustrated by the large and small scales shown in Figure I.9. The largest eddies break down into smaller eddies, which break down into even smaller eddies. This process of eddy

breakdown transfers kinetic energy from the mean flow to progressively smaller scales of motion. This process is known as the energy cascade. At the smallest scales of turbulent motion, the kinetic energy is converted to heat by means of viscous dissipation [19].

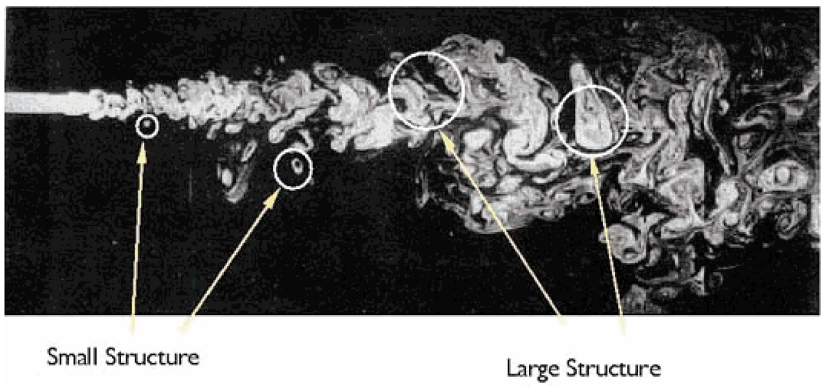

Figure I.9 – Large vs. small scale eddies of smoke flow [19].

I.3.4 Isotropic turbulence spectra

The topology of isotropic turbulent flow can be described in a statistical sense with the help of the energy spectrum $E(k)$, which is a performance spectral density of velocity fluctuations. This spectrum shows us the distribution of kinetic energy in individual wave numbers. Figure I.10 shows a model energy spectrum, which shows the typical form of an energy spectrum obtained from an experiment. In the graph, non-dimensional variables are used, which are defined with the help of Kolmogorov scales. The energy spectrum in log-log coordinates is characterized by an inclination of 2 in the energy area and an inclination of $-5/3$ in the inertial subrange. In the area of dissipation, there is quicker suppression of the spectrum. The inclination of the spectrum in the energy area is not entirely clear, and its actual value depends on specific boundary conditions ; the specified value expects isotropy [15].

In flows of practical interest, the turbulent stress tensor is non-isotropic, a state created partly by the deformation of the large eddies by mean strain or body forces, partly by flow inhomogeneities and partly by boundary conditions. If the stress tensor were isotropic, all the normal stresses would be equal, and there would be no shear-stresses (for otherwise, reorienting the axes would cause the normal stresses to be unequal). Thus, in isotropic turbulence : $\overline{u_i u_j} = 2\delta_{ij}k/3$. A departure from the isotropic state provides a measure of the stress anisotropy, which can be expressed in terms of the deviatoric part of the stress tensor [15].

$$\overline{u_i u_j} = \underbrace{\left(\overline{u_i u_j} - \frac{2}{3}k\delta_{ij}\right)}_{anisotropic} + \underbrace{\frac{2}{3}k\delta_{ij}}_{isotropic} \tag{I.12}$$

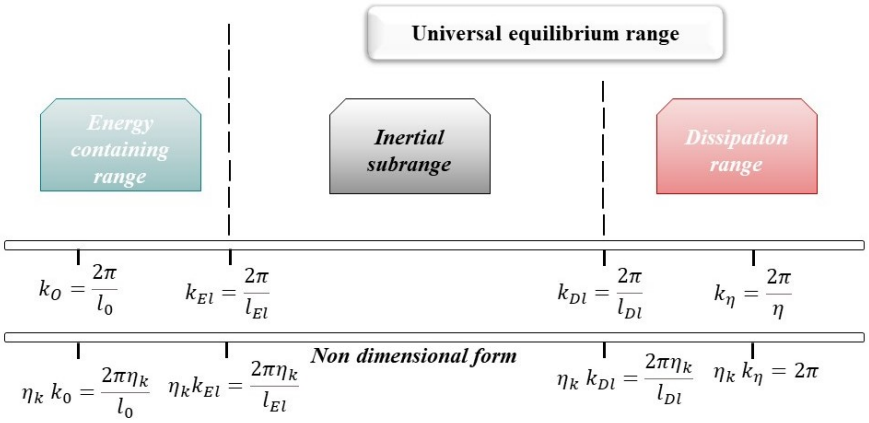

Figure I.10 – Isotropic turbulence spectra.

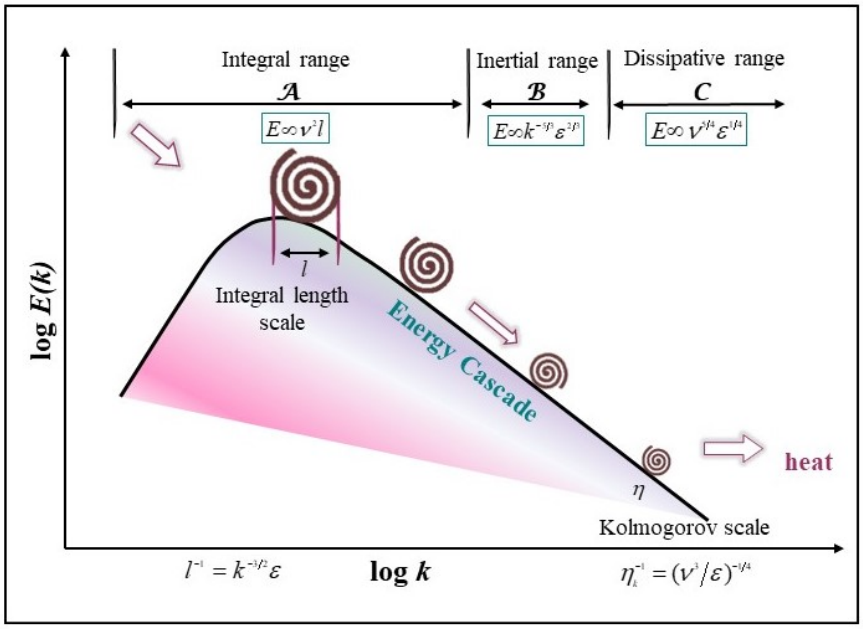

Figure I.11 – Kolmogorov cascade.

In 1941 Kolmogorov published a fundamental article that gives a mathematical apparatus to Richardson's idea of an energy cascade. Kolmogorov's theory is based on three hypotheses : a hypothesis of local isotropy, and the first and second similarity hypotheses.

The hypothesis of local isotropy relates to small-scale vortices. The largest vortices have approximately the dimension of shear area, and the topology of these vortices is anisotropic, which can be attributed to specific boundary conditions (often very regular). The mean size of energy vortices is smaller, which we will refer to as ℓ_0 . The more or less chaotic energy transfer towards small scales is leading to a gradual increase in the isotropy of smaller scales. This is the basis for the Kolmogorov hypothesis of local isotropy ; during sufficiently high Reynolds numbers, the

motions of small scales $\ell \ll \ell_0$ are statistically isotropic. The scale ℓ_{EI} is the boundary between small isotropic vortices and large non-isotropic vortices. For a better idea, let us consider $\ell_{EI} \approx 1/6\ell_0$. In the area of small isotropic vortices, $\ell < \ell_{EI}$ two mechanisms of energy transfer dominate transfers from large scales to small scales and viscous dissipation.

The parameters that manage these processes are the rate of energy transfer from large scales to small $\Im_{EI}$ and kinematic viscosity ν. In a settled state, the rate of dissipation ε[10] is in balance with the rate of production : $\varepsilon \approx \Im_{EI}$. It is apparent from this that the universal statistical state of small scales is determined by viscosity ν and the rate of the transfer of energy from the area of large scales $\Im_{EI}$. This outcome formulates Kolmogorov's first similarity hypothesis, which says that in a turbulent flow with a sufficiently high Reynolds number, the statistics of motions of small scales ($\ell < \ell_{EI}$) have a universal formulation and depend only on the scale ℓ, viscosity ν and dissipation rate ε [20]. For the dimension analysis, we can use ε and k, and then we get :

$$E(k) = \varepsilon^{2/3} k^{-5/3} \Psi(k\eta_k), \tag{I.13}$$

Where $\Psi\,(k\eta_k)$ is the compensated Kolmogorov spectrum function. The area of scale $\ell < \ell_{EI}$ is usually referred to as the universal equilibrium range. In this area, the scales $\ell/u\,(\ell)$ are small compared to ℓ_0/u_0 and small vortices can quickly adapt to conserve dynamic equilibrium with the rate of energy transfer $\Im_{EI}$, which is determined by large vortices $u(\ell)$ the typical value of fluctuations in velocity for perturbation of scales l and u_0 and then for ℓ_0 . From the dimensional analysis, it is possible to clearly specify the values of resulting Kolmogorov scales (except the non-dimensional constant). The relevant quantities are only the rate of dissipation $\varepsilon[m^2/s^3]$, and kinematic viscosity $\nu\,[m^2/s]$: length, velocity and time-based Kolmogorov scale $\eta_k\,[m]$, $\mathrm{u}_\eta\,[m/s]$ and $\tau_\eta\,[s]$, respectively, can be define the following equations :

$$\eta_k = \left(\frac{\nu^3}{\varepsilon}\right)^{1/4} \tag{I.14}$$

$$u_\eta = (\varepsilon\nu)^{1/4} \tag{I.15}$$

$$\tau_\eta = \left(\frac{\nu}{\varepsilon}\right)^{1/2} \tag{I.16}$$

Two identities are apparent from these definitions. First, the Reynolds number based on Kolmogorov parameters is a unit : $\eta_k u_\eta/\nu = 1$. This fact is in accordance with the claim that the cascade transfer continues in the direction towards continuously smaller scales until the

Reynolds number is so small that it enables dissipative processes. Also, from the Equations I.14 and I.15 we can express the rate of dissipation :

$$\varepsilon = \frac{\nu^3}{{\eta_k}^4} = \frac{u_{\eta_k}^4}{\nu} = \frac{\nu}{\tau_{\eta_k}^2} \tag{I.17}$$

In the inertial subrange, the effect of the viscosity is insignificant, and the coefficient $k\eta_k << 1$ is insignificantly small. Therefore, in the inertial area, the compensated Kolmogorov spectrum is defined Equation I.13 approximately by a constant $\Psi\left(k\eta_k\right) = C$. and the energy spectrum can be expressed by the relationship [21] :

$$E(k) = C\varepsilon^{2/3}k^{-5/3} \tag{I.18}$$

Where C is the universal constant (≈ 1.5).

CHAPTER II

MODELING OF TURBULENCE AND BIBLIOGRAPHIC REVIEW

- Turbulence modeling
- Scale resolving simulations
- Numerical procedures
- Bibliographic review

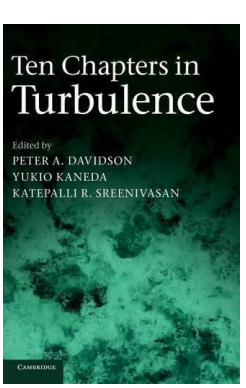

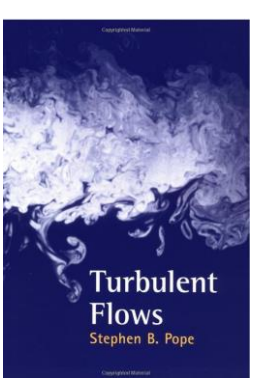

MODELING OF TURBULENCE AND BIBLIOGRAPHIC REVIEW

II

II.1 Turbulence modeling

The implementation of all methods used in turbulence is based on the use of numerical mathematics–discretization of the problem is performed in space and time. Generally, each method of mathematical modelling requires enough spatial and time discretization to model the values of the gradients of all variables, which are considered in this case. The maximum values of these gradients are based on the minimum sizes of structures. Their sizes depend on flow conditions (the geometry of the area, speed, and properties of the fluid) and the requirement for the results.

Using the *DNS* method, it is necessary to select discretization, so that Vortex structures of all sizes up to Kolmogorov length and Kolmogorov time scale are captured. In the *LES* discretisation method, the filter for spatial structures is defined. The turbulent fluctuations in the flow are usually resolved by employing either *DNS* or *LES*. The basic principle of *LES* is to resolve all the energy-carrying 'large eddies' while the dissipative 'small eddies' are modelled. In terms of computational requirements and time, *LES* occupies an intermediate position between *DNS* and *RANS*. Recent advances in computational technology have made *LES* more viable and affordable for industrial turbulence studies. Over the past decade, more and more and more attention has been paid to the reliability of using *LES* to analyse turbulent flows. However, it is yet to replace *RANS* as the most widely used industrial approach for predicting turbulence (see Figure II.1) [13].

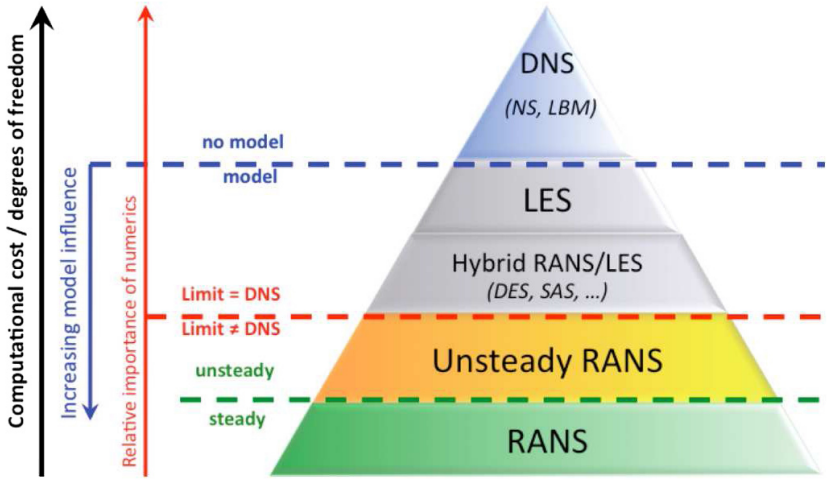

Figure II.1 – Classification of unsteady approaches according to levels of modeling and readiness [22].

II.1.1 Direct Numerical Simulation (DNS)

During the implementation of calculations with the help of *DNS*, spectral or pseudo-spectral methods are used. A solution is expected in the form of a Fourier series in space. This approach was processed in 1972 by Orszag with Patterson. As a result of the capacity of computer technology, the *DNS* method is still used for the calculation of geometrically simple areas of flow during extremely small Reynolds numbers. For increasing the Reynolds number, the number of discretized elements in the area is sharply growing, and the necessary time step is declining. The flow calculations with the help of *DNS* are extremely demanding on the performance of computer technology and last a very long time. It can be proved that computer demands considering the discretization in space and time, grow with the sixth power of the Reynolds number. Today best computers, with the performance of dozens of gigaflops, can resolve tasks with the help of *DNS* characterized by a Reynolds number of order of a maximum of 10^3. From an application point of view, tasks of turbulent flow in machines are characterized by Reynolds numbers of 10^5 and greater, and flow in the atmosphere and hydrosphere is several times greater. For achieving a ten times greater Reynolds number, it will be necessary to increase the performance of computers a million times.

The *DNS* method is currently used and, obviously, for a long time in the future, will be used to solve fundamental tasks related to turbulence theory. It is limited to geometrically simple areas and very low Reynolds numbers. However, it provides us with a perfect picture of the physics of flow fluid. From a correctly performed *DNS* simulation, obtaining random variables in a random location and time is possible. The results of such simulations are generally regarded as

equivalent to the results of experiments, but experiments are far ahead in terms of reliability and comprehensiveness of information [20].

Direct Numerical Simulation represents the modeling of Navier-Stokes equations with the help of numeric mathematical processes. Such that all persisting eddies are resolved. Small flow structures will develop if the Reynolds number of a flow becomes very large. But, due to viscous forces in the flow, very small eddies die rather quickly. The Kolmogorov law gives the size of the persisting eddies, It is $\left(Re^{-3/4}\right)$ in $3D$ and $\left(Re^{-1/2}\right)$ in $2D$. To capture all persisting eddies in, one would need a mesh size of $\sim Re^{-3/4}$.

In relation to this, the number of degrees of freedom n_f of the particular problem is usually defined, which is related to the number of elements of the discretization network. It is based on the relationship between the size of the largest l_0 and the smallest η. structures in the flow field.

From the Kolmogorov theory for isotropic turbulence, there is apparent dependence of this relationship on the Reynolds number in the formulation $l_0/\eta_k \sim \mathrm{Re}^{3/4}$. The number of degrees of freedom of the problem is related to the number of elements in the 3-dimensional space [20]. Therefore, the following proportion applies :

$$n_f \sim (l_0/\eta_k)^3 \sim \mathrm{Re}^{9/4} \tag{II.1}$$

II.1.2 Large Eddy Simulation (LES)

LES is currently a very popular approach for turbulent flow simulation. The basic idea starts by decomposing the quantities which describe the flow (velocity, pressure, body forces) into two parts : one part containing the large flow structures (large scales) and the remainder containing the small scales, this approach makes sense in applications. Considering again the example of a hurricane, one is primarily interested in predicting the behavior of the large eddies. These eddies are the most dangerous ones and it is important to predict their way and their velocity in order to take steps to offer protection. The actual behavior of the millions of small eddies is not of interest. But these small eddies of course influence the behavior of the large eddies. There is a direct interaction between the small and the large eddies.

In addition, the interaction of the small eddies among each other influences the large eddies. That means, a prediction of the behavior of the large eddies is not possible without taking into account the interactions coming from the small eddies. The distinction of what are the large

scales and the small scales might be given by the application. The following figure show the classification of unsteady approaches as show the following figure.

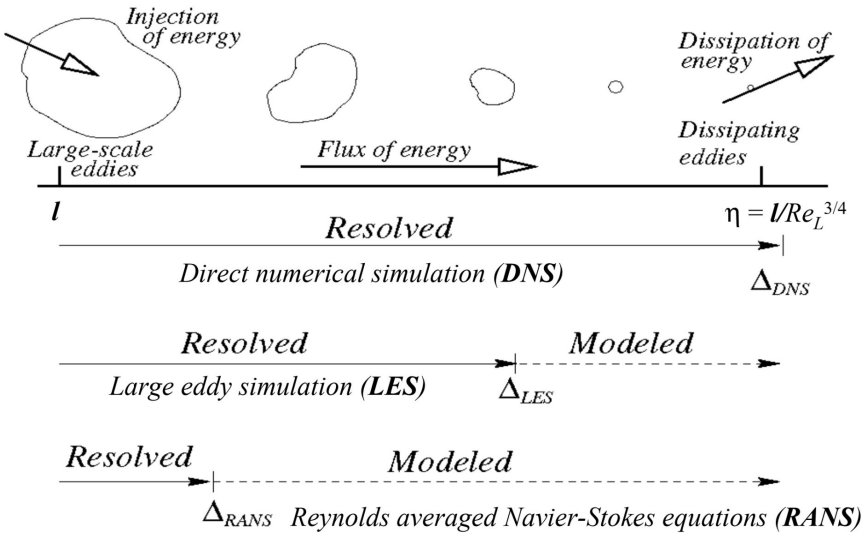

Figure II.2 – Dissipation in DNS and LES [5].

II.2 Numerical procedures

The adequacy of the computational domain is assessed later by examining the streamwise two-points correlations which must be large enough to include the largest length scale structures, periodic boundary conditions for the velocity components were applied in streamwise and circumferential directions whereas no-slip boundary conditions were imposed at the wall ; in additional to the Neumann boundary conditions were used for the pressure. Periodic boundary conditions were imposed in the streamwise and the spanwise directions since the turbulent flow is fully developed. The periodic boundary in the streamwise direction can be justified provided that the flow can be considered homogeneous in that direction and that the length of the computational domain was sufficiently large to include the largest scale of the turbulent motions in the flow. This can be checked by ensuring the streamwise two-points correlation coefficients are uncorrelated at a separation of one-half period in the homogeneous directions and this is when these correlations fall of to zero value, according to the given equation :

$$R_a(1/2\,L_z\,) = \frac{\langle a'(r,\theta,z,t)a'(r,\theta,z+1/2\,L_z\,,t)\rangle}{\langle a'(r,\theta,z,t)a'(r,\theta,z,t)\rangle} \approx 0 \tag{II.2}$$

A domain independence study has largely carried out for the moderate Reynolds number : the main findings indicate that the adequate domain length is $L = 5D$ in the Newtonian fluid. For the shear-thinning power-law fluids, according to Singh et al. [23], the flow index affects the

long helical structures near the wall and at the centre of pipe, where the range of length scales in the flow increases with decreasing flow index, where Singh et al. chose $4\pi D$ as domain length for the flow index $0.6 < n < 1$, and $16D$ for $n = 0.4$.

In order to achieve a realistic numerical simulation of a turbulent flow, the adequacy of numerical resolution in the direct numerical resolution is still one of the greatest challenges, where the spatial and temporal resolutions must be sufficient fine to resolve the smallest length scale structures in turbulent flow. In other word, the Kolmogorov length and time scales must be resolved by the spatial and temporal network distribution : the distance between two sequential points in space and time should be proportional to the Kolmogorov scales. In this end, a number of criteria have been deduced to estimate this required numerical resolution. As mentioned above, the Grötzbach [24] criteria are one of the large commonly used techniques for evaluating the spatial resolution, where he formulated three criteria :

The first one concerns the computational domain which should be large enough to include the largest length scale structures ; the second one requires that the vertical grid width distribution must be able to fully resolve the thin vortical layers in the vicinity of the wall responsible for the wall friction and for the turbulence production, which can be met by ensuring that at least three gridpoints within the viscous sublayer. The last one requires the mean grid widths must be smaller than the smallest relevant turbulence elements. As for the temporal resolution, a more restrictive criterion must be applied to ensure that the time step is enough to resolve the smallest time scale structures in turbulent flow and to avoid numerical instabilities : This can be achieved by assuring that the imposed time step must be smaller than the Kolmogorov time scale.

Our present DNS investigation have been carried out on a finite difference scheme, second-order accurate in space and time. The numerical resolution is $(129 \times 129 \times 193)$ gridpoints in (radial, tangential, and axial) directions, respectively, with a domain length of $20R$.

In LES, numerical spatial resolution is always one of the biggest challenges. Indeed, the mesh imposed on the computational domain should be enough fine to capture and resolve the smallest scale structures in the turbulent flow, and limit the influence of the mesh on the accuracy of the results. A uniform distribution of gridpoints must be applied in the axial and circumferential directions (periodic directions) in order to use the trigonometric developments elements in the pressure equation. A non-uniform distribution must be imposed in the normal direction of the wall where a refinement of the mesh near wall region is necessary for a better resolution in the zone close to the wall. In fact, in the viscous sub-layer, at least three gridpoints must be

arranged so that the first gridpoint must be located at $(Y^+ < 1)$.

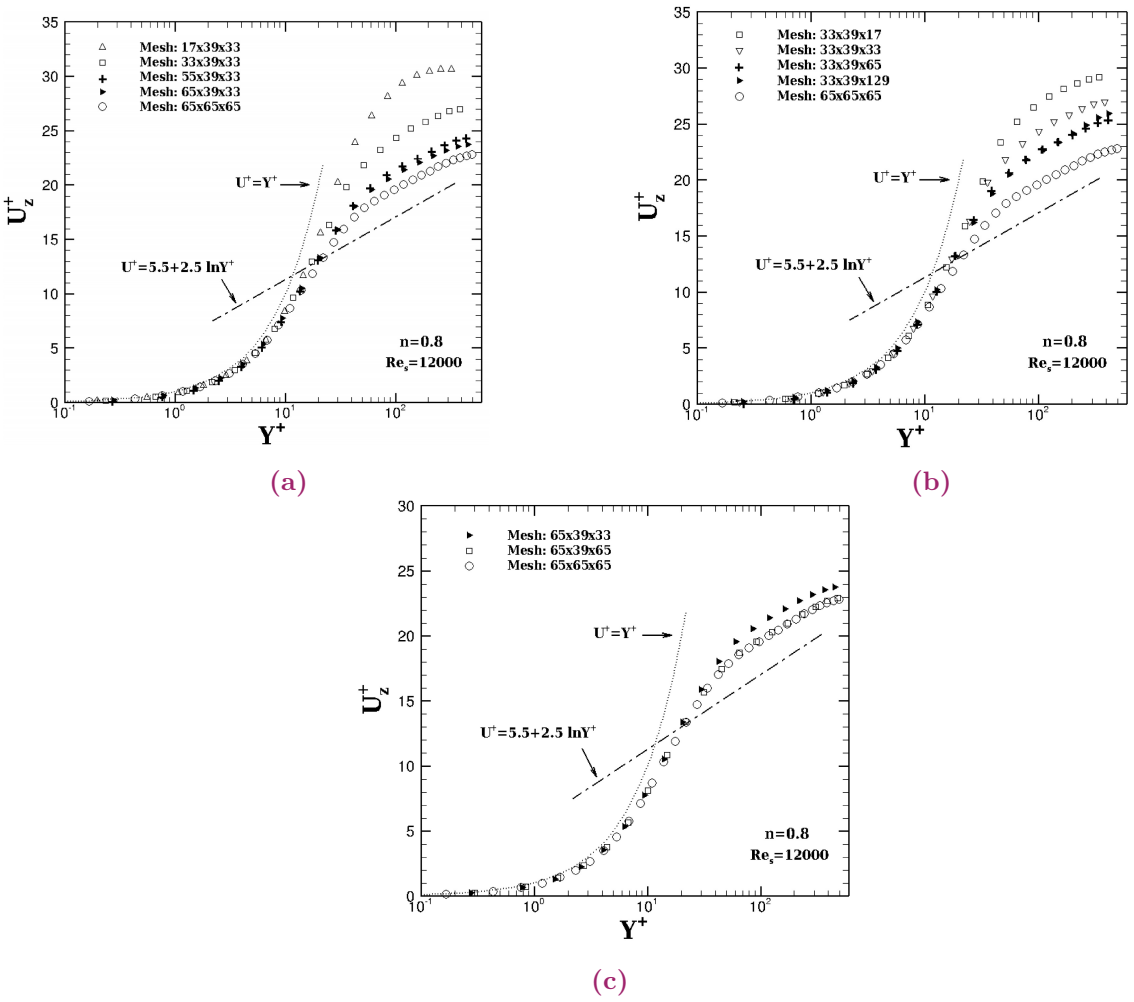

Figure II.3 – Gnambode mesh independence study.

In order to ensure the precision of the spatial grid resolution, a study of the mesh independence is necessary. To this end, Gnambode et al. performed their study with the *LES* code used in the present study for an Ostwald de Waele fluid with a flow index of 0.8 at a simulation Reynolds number of 12000, with different numbers of gridpoints in the circumferential, axial, and radial directions, presented respectively in (a), (b) and (c) in Figure II.3.

They found that the grid of $(65 \times 65 \times 65)$ gridpoints in the axial, radial, and circumferential directions respectively and admitting an adequate resolution is considered as a good compromise between the required precision and the *CPU* time. Note that in their investigations, Gnambode et al. [25] used a length domain in the flow direction (axial direction) of $20R$. The primitive variables will be calculated at different points, located on the faces of the cells for the velocity

components or in the center of the cells for the scalars in Figure II.4. The variables $q_\theta = rV_\theta, q_r = rV_r$ and $q_z = V_z$ and they are considered in order to avoid the problem of the singularity on the axis of the driving. The positions of the variables are defined by the following spatial coordinates :

$$\bar{q}_\theta \rightarrow \left(i, j+\frac{1}{2}, k+\frac{1}{2}\right) \; where \; (\theta_c(i), r_m(j), z_m(k)) \tag{II.3}$$

$$\bar{q}_r \rightarrow \left(i+\frac{1}{2}, j, k+\frac{1}{2}\right) \; where \; (q_m(i), r_c(j), z_m(k)) \tag{II.4}$$

$$\bar{q}_\theta \rightarrow \left(i+\frac{1}{2}, j+\frac{1}{2}, k\right) \; where \; (\theta_m(i), r_m(j), z_c(k)) \tag{II.5}$$

$$\bar{p}, \bar{\Theta} \rightarrow \left(i+\frac{1}{2}, j+\frac{1}{2}, k+\frac{1}{2}\right) \; where \; (\theta_m(i), r_m(j), z_m(k)) \tag{II.6}$$

$$\theta_c = (i-1)\Delta\theta, i = 1....n_1, \; \theta_m = (i-1/2)\Delta\theta, i = 1....(n_1-1), \; \Delta\theta = \frac{2\pi}{n_1-1} \tag{II.7}$$

$$r_c = (j-1)\Delta r, j = 1....n_2, \; \mathrm{r}_m = (j-1/2)\Delta r, j = 1....(n_1-1), \; \Delta r = \frac{R.f(r)}{n_2-1} \tag{II.8}$$

$$z_c = (k-1)\Delta z, k = 1....n_3, \; \mathrm{z}_m = (k-1/2)\Delta z, k = 1....(n_3-1), \; \Delta r = \frac{L}{n_3-1} \tag{II.9}$$

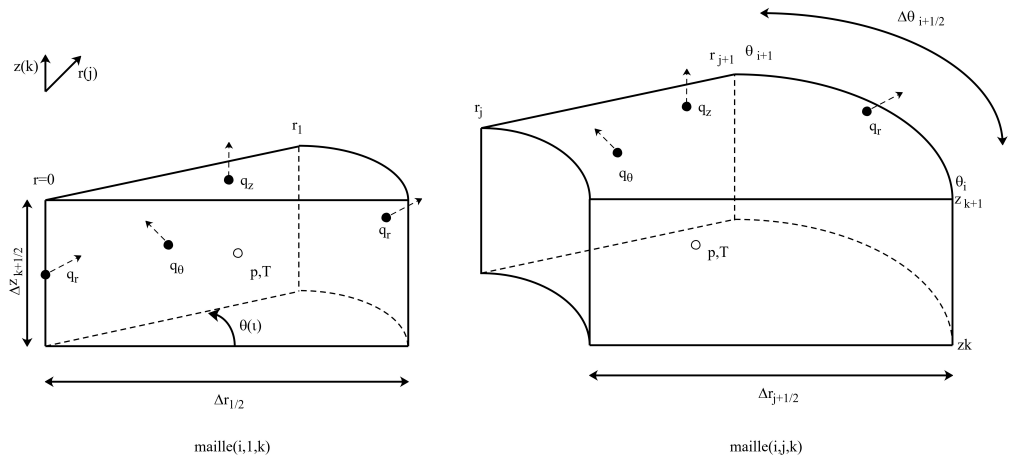

Figure II.4 – Staggered mesh.

Note that in the radial direction, a non-uniform grid resolution specified by a hyperbolic function has been applied in the radial (r) direction, where the gridpoints in this direction are closest together at the cylinder wall and progressively spaced away from the wall towards the center of

the cylinder as shown the following figure :

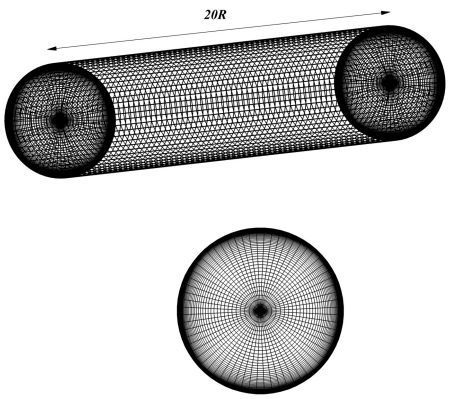

Figure II.5 – Grid mesh.

The mesh refinement is given by the hyperbolic equation :

$$y_j = |r_j| \sin\left[\pi + (j-1)\theta\right] \ \text{(j=1,.....,m}_j\text{)} \tag{II.10}$$

$$z_j = |r_j| \cos\left[\pi + (j-1)\theta\right] \tag{II.11}$$

$$\theta = \frac{\pi}{40(m_k - 1)} \tag{II.12}$$

$$r_j = r_a \frac{\tanh(\alpha\xi_i)}{\tanh(\alpha_a)} \tag{II.13}$$

$$\xi_j - 1 + 2\frac{j-1}{m_j - 1} \tag{II.14}$$

$$\alpha_a = \frac{1}{2} \ln\left(\frac{1+b}{1-b}\right) \tag{II.15}$$

$$r_{\alpha_a} = \frac{1}{2}(r_{outer} - r_{inner}) \tag{II.16}$$

Parameter (b) is used to control the extent of the grid to the walls and typical values for this study are between 0.7 and 0.95. The parameters m_i, m_j, m_k are the number of vertices in the axial, radial, and tangential directions respectively. α_a is the adjustable parameter to determine the concentration of gridpoints in the flow region near the wall.

Time is rendered dimensionless using the cylinder radius R and the maximum laminar flow velocity U_{cL}. The calculations were carried out at a constant CFL (Current, Friedrichs and Lewy state) and not at a constant time step. Gnambode, performed a time-step independence study of the Ostwald de Waele fluid with a flow index of 0.75 through a no rotating pipe. The study considers CFL of $0.04R/U_{cL}$ or $0.01R/U_{cL}$ for stabilize the solutions and avoid the divergence problem. However, the time step which varies is limited by the value $\Delta t = 0.01$ for $n = 0.75$.

The statistics are calculated by averaging in the periodic directions and over time. The final data are obtained by ensemble average over the time interval from the scaled time $t = 250$ to $t = 8000$ for the smallest rotation rate. At the highest rotation rate, statistics are sampled from scaled time $t = 250$ to $t = 10000$ [5].

II.3 Bibliographic review

Turbulence flow is one of the fundamental issues in fluid mechanics; fluid mechanics is the study of how fluids move and the forces that develop as a result. Turbulence is a significant issue that has previously received much attention in the mechanical and engineering fields. Fluid flow can be either laminar, turbulent, or transitional. For laminar flow, there is only one component of velocity. Concerning turbulent flow, the predominant component of the velocity is also along the pipe, but it is unsteady and accompanied by random components normal to the pipe axis. In the transitional flow, both laminar and turbulent features occur. The most critical dimensionless parameter for pipe flow is the Reynolds number, the ratio of inertia to viscous effects in the flow [26].

Reynolds made one of the first efforts to quantify turbulence, demonstrating that when a critical parameter (Reynold number) is exceeded, the flow regime changes from orderly laminar to turbulent. The turbulent flows contain a hierarchy of eddies or spirals ranging in size from the largest scales to the smallest. The transfer between these scales from the larger to the smaller creates energy until molecular viscosity finally dissipates the minor scales into heat. This theory was formulated by the Russian scientist Kolmogorov [16].

Both natural processes and numerous industrial processes involve turbulent flows. For instance, a high-velocity wind can abruptly change direction, and speed is present during a storm. When an aeroplane takes off, the air above the runway becomes agitated. This air must be calmed

before the next aircraft takes off. This is essential because there is a time limit on how long the plane can wait between take-offs. Numerous other applications for turbulent flows include oceanography and wind channels used in automobile design. Often, chemical reactions like those in gas engines involve turbulent flows. There are numerous significant and fascinating physical phenomenon [27].

A significant industrial issue that has recently attracted a lot of attention is the turbulent flow of Newtonian fluids in an axial pipe. A range of engineering applications, including flow in turbo engines, heat exchangers, combustion chambers, nuclear reactors, etc. include turbulent flow in pipes, which is significant in the mechanical and engineering sectors. A considerable amount of literature has been investigated to perform the fully developed turbulent flow characteristics of Newtonian fluids flowing inside isothermal cylindrical pipes either experimentally or numerically by the references : [16], [27] [28], [29], [30].

Nishibori and Kikuyama (1987) [31] experimentally investigated the turbulent flow of the Newtonian fluid inside an axially rotating pipe utilising the laser Doppler velocimeter and flow visualization techniques. To shed further light on the laminarization phenomenon. It is observed that the rotating boundary layer is initially strongly stabilized by the centrifugal force due to the rotating velocity component, resulting in a laminarization of flow ; when the rotation speed of the pipe is increased to a certain value, a laminarization phenomenon is observed in the rotating layer in the inlet region near the entrance. Interestingly, when laminarization occurs in the rotating layer near the pipe wall, the axial velocity profile becomes flat near the pipe axis, similar to that observed in the laminar inlet flow developing in a stationary pipe. Thus, the flow pattern inside the boundary layer near the pipe wall can be estimated using the shape factor based on the axial velocity profile. Moreover, under the same rotation rate conditions, the laminarization of flow in the inlet region is promoted as the axial Reynolds number is decreased.

A modified two Reynolds stress transport closure model was created by Malin and Younis (1997) [32] for simulating fully developed turbulent flow and heat transfer of Newtonian fluid through an axially rotating conduit. The turbulence-energy dissipation rate, turbulent stresses, heat fluxes, and modeled transport equations are all solved. The investigation findings demonstrated that both models mimic the significant reduction of turbulent transport caused by rotation. The model results are generally consistent with both published data and large eddy simulations. They discovered that the SSG model produced a closer agreement with the observed tangential

velocities than the QI, IP, and $IP-C$ models. Their calculations demonstrated an encouraging understanding of the measured data and LES findings. The discovery suggests that the rotation rate significantly influences the hydrodynamic and thermal properties.

Ould-Rouiss and Feiz [33] performed Direct Numerical Simulation and Large Eddy Simulation of fully developed turbulent pipe flow in an axially rotating pipe for various Reynolds numbers and rotation rates. The DNS has been carried out at two Reynolds numbers $Re = 4900$ and $Re = 7400$ for different rotation rates ranging from 0 to 18. Large Eddy Simulation with the dynamic model have been conducted for a Reynolds number up to 20600. Different statistical turbulence quantities, including the mean and fluctuating velocity components, friction coefficient, Reynolds shear-stresses, and higher order statistics, are obtained and analyzed. Their study investigates the effects of the Reynolds number and the rotation number on the turbulent flow characteristics. The governing equations are discretised on a staggered mesh in cylindrical coordinates. The numerical integration is performed by a finite difference scheme, second-order accurate in space and time. The time advancement employs a fractional step method. Their results show that the axial velocity profile gradually approaches a laminar shape when increasing the rotation rate due to the stability effect caused by the centrifugal force.

(DNS) and (LES) of turbulent channel flow of various non-Newtonian fluids were carried out using the viscosity of the power-law and Casson models. In their investigation, Ohta and Masahito Miyashita. (2014) [34]. used a low Reynolds number of wall turbulence of non-Newtonian viscous fluid close to Newtonian fluid. Based on the DNS results, the turbulence structures of these viscous fluids might be generally normalized but with locally changing viscosity as for Newtonian fluid. Moreover, the LES results showed that the Smagorinsky model of turbulent flow for non-Newtonian fluids might be treated universally by spatially scaling the locally changing viscosity.

According to Eggels (1994), Yang (2000) [35] argued that suppressing radial fluctuations leads to the Taylor-Proudman theorem, which is manifested in the suppression of turbulent fluctuations perpendicular to the plane of rotation, where rotating flow tends to become two-dimensional in its plane of rotation. These investigations have shown that the swirl of the forced vortex has a stabilising influence which suppresses the turbulent radial exchange of heat and momentum. In particular, the pipe rotation reduced the hydraulic loss and wall heat transfer rate.

A constant viscosity characterises the Newtonian behavior concerning shear-rate. Non-Newtonian fluids do not directly link shear-stress and shear-rate. This class of fluids has an infinite number of possible rheological relationships. No single equation has yet been proven to precisely define the shear-stress-shear-rate relationships of all such materials over all ranges of shear-rates-the turbulent flow of non-Newtonian systems [36].

In technical applications, non-Newtonian fluids often exhibit Pseudoplastic behavior. Shear thinning fluids have an apparent viscosity that decreases with an increasing shear-rate. The viscosity of power-law fluids (a specific class of shear-thinning fluids) decreases as the rate of fluid deformation increases [37]. When the shear-stress is very small, flow begins to occur (the flow curve passes through the origin), and the growth rate in shear-stress increases with increasing shear-rate. This behavior is called shear thickening [3].

Bogue and A.B. Metzener (1963) [38] presented velocity profiles of viscous Newtonian and non-Newtonian fluids flowing through smooth, circular tubes recorded in the turbulent core area. The flow behavior indexes ranged from 0.45 to 0.90, while the Reynolds numbers ranged from transitional levels to above 100000. When normalized concerning the mean velocity or compared based on the velocity defect parameter, turbulent core profiles were identical to those for Newtonian fluids. The apparent viscosity measured at the wall shear-stress is a useful parameter from a mechanical perspective. Its use lessens the dependence of the friction factor correlation on model-based parameters at low Reynolds numbers (i.e, on the flow behavior index n). Extrapolation raises the intriguing possibility that, at high Reynolds numbers, the apparent viscosity would suffice as a characterization. Since the parameter must be calculated through trial and error, it is less interesting from a design perspective.

Malin (1997) [39] used the modified version of an existing two-equation turbulence model to represent the turbulence of power-law fluids in smooth circular tubes to examine the effect of the power-law index and generalised Reynolds number. In the same year, Malin (1997) [32] used the same study with another computation of Bingham-plastic fluids. The LB $k-\varepsilon$ and Wilcox $k-\omega$ turbulence models were tested against experimental data on the friction factor and mean velocity profile for various Bingham different Reynolds numbers, with different values of the Hedstrom number. Where the numerical results of the power-law of friction factor and velocity profile are compared to experimental data, the model produces reasonably good agreement with the experiment. Furthermore, the results show that latency in transition to turbulence

was predicted only for strongly non-Newtonian fluids with $n = 0.6$.

Malin (1998) [40] presented other numerical results using a two-equations turbulence model to compute the turbulent flow of Herschel-Bulkley fluids in smooth pipes. The model generates flow resistance curves over a range of power-law indices and generalized Reynolds and Hedstrom numbers. The computed results for the laminar regime were in excellent agreement with the analytical data.

In 2015, Gnambode et al. [25] implemented a (LES) technique with an extended Smagorinsky model to perform a numerical investigation into the turbulent flow of power-law fluids. Their study is one of the first investigations to examine in detail the turbulent flow of Pseudoplastic and Dilatant fluids through a pipe at different Reynolds numbers (4000, 8000, and 12000) and over a flow behavior index of $(0.5 \leq n \leq 1.4)$.

Gnambode et al. [25] offered an extensive analysis of flow behavior index and Reynolds number effects on the rheological and turbulence characteristics. The findings of their study suggest that the decreased flow behavior index induces a marked enhancement in the mean axial velocity profiles in the logarithmic flow region (Figure II.6a). This is due to the higher viscosity in the core flow region. It is worth mentioning that increased Reynolds number results also an increase in the velocity profiles along the pipe radius, especially in the logarithmic flow region (Figure II.6b).

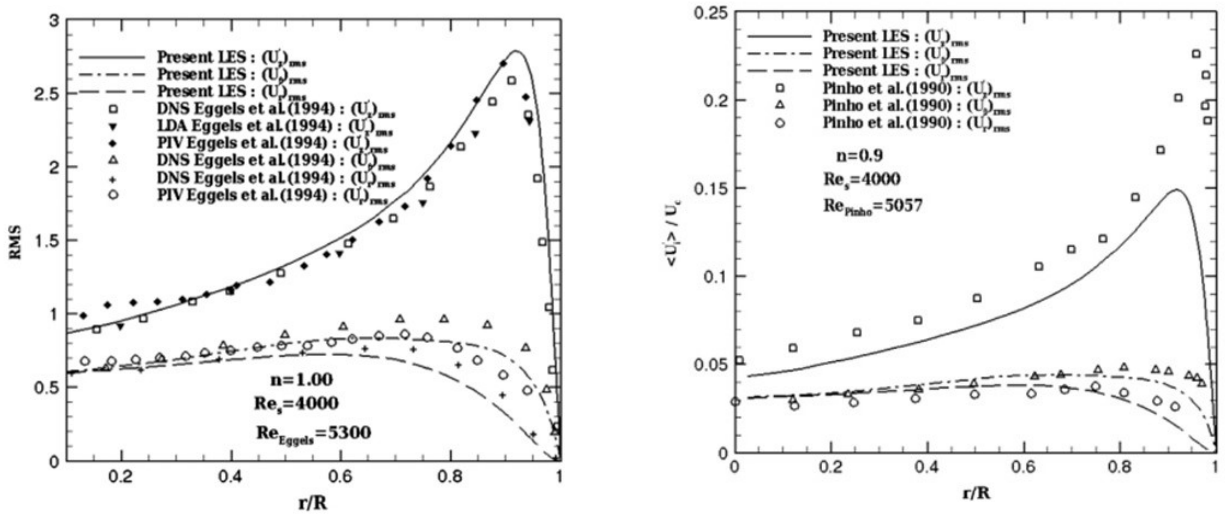

(a) (b)

Figure II.6 – RMS of axial velocity fluctuations [25].

Gavrilov and Rudyak (2016) [41] developed power-law fluid turbulent pipe flow using *DNS*. Two calculations were performed at generalized Reynolds values of 10^4 and 2×10^4, and the power-law indices n varied from 0.4 to 1. The researchers found that the predicted friction coefficient agreed with the experimental correlation. Moreover, the results showed that when compared to the flow of Newtonian fluid, the anisotropic Reynolds stress tensor is stronger in power-law fluid flows. As the flow index n decreases, the turbulence anisotropy becomes more prominent.

Recently, Abdi et al. 2019 [42] offered extensive investigations of the turbulent flow of non-Newtonian fluids using the *LES* approach; these investigations provided an important opportunity to advance the understanding of the rheological behavior heat transfer mechanism on the non-Newtonian fluids. The authors employed the *LES* with an extended Smagorinsky model to investigate numerically the fully developed turbulent flow of Ostwald de Waele fluid through a straight cylindrical pipe with a length of the domain of $20R$ in the axial direction and a numerical resolution of 65^3 grid points in the axial, radial, and circumferential directions.

Abdi et al. 2019 [42] provided the first extensive investigation of the heat transfer of a shear-thinning using *LES* with an extended Smagorinsky model. They numerically investigated the forced convection fully developed turbulent flow of the Pseudoplastic $(n = 0.75)$ and Newtonian fluids through a heated axially rotating pipe over a rotation rate range $(0 \leq N \leq 3)$ at simulation Reynolds and Prandtl numbers equals 4000 and 1, respectively.

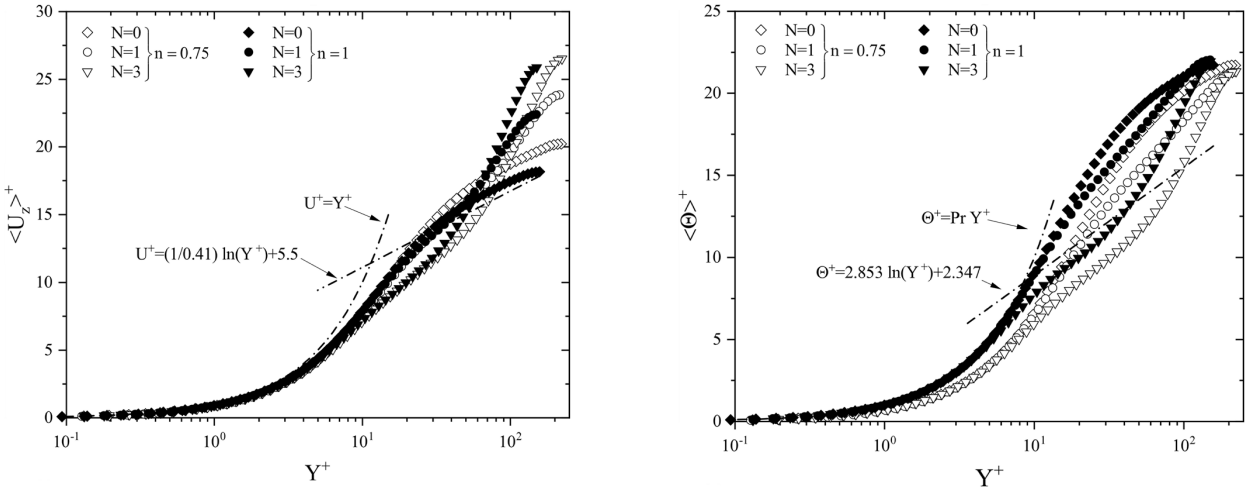

(a) Turbulent Axial Velocity. **(b)** Mean temperature profile.

Figure II.7 – Results of Abdi et al. [42].

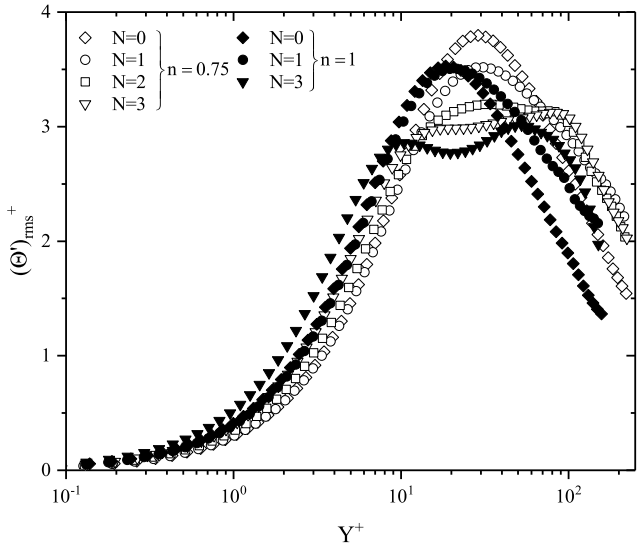

Figure II.8 – RMS of temperature fluctuations [42].

In this study, a Direct Numerical Simulation (DNS) was conducted to examine the turbulent flow characteristics of Pseudoplastic, Newtonian, and dilatant fluids through an isothermal pipe. The simulation was performed at a Reynolds number of 6500. The numerical resolution employed a grid consisting of $129 \times 129 \times 193$ points in the axial, radial, and circumferential directions, respectively.

Furthermore, a Large Eddy Simulation (LES) with an extended Smagorinsky model was employed to investigate the forced convection of a thermally independent Ostwald de Waele fluid through a heated stationary pipe in a fully developed turbulent flow regime. This investigation encompassed different flow behavior indices and Reynolds numbers (4000, 8000, and 12000).

CHAPTER III

DNS OF TURBULENT FLOW OF OSTWALD DE WAELE FLUIDS

- Introduction
- Problem description
- Mathematical formulation
- Results and discussion
- Conclusion

RESOLVED

DNS OF TURBULENT FLOW OF OSTWALD DE WAELE FLUIDS

III

III.1 Introduction

Non-Newtonian fluids have complex rheological properties, so their flow behavior is difficult to predict using traditional experimental methods or analytical models. Direct numerical simulation (DNS) is a powerful tool for understanding the complex flow behavior of fluids. In particular, it is a highly accurate method for resolving turbulence and its impact on fluid flow. One important parameter affecting fluid flow behavior is the flow behavior index. The flow behavior index is commonly used to describe the rheological properties of fluids in various industrial applications, including oil and gas production, chemical processing, and food production.

The fully developed turbulent flow of non-Newtonian fluids through a smooth stationary pipe is a problem of considerable significance and has received much attention in the past ; the literature contains several well-documented experimental and numerical investigations. These studies have given special consideration to describing this kind of fluid rheological and hydrodynamic behavior by revealing the effects of various rheological parameters on flow patterns and the turbulence features.

III.2 Problem description

The present study deals with numerical simulation with a fully developed turbulent flow of Pseudoplastic $(n = 0.75)$, Newtonian $(n = 1)$, and Dilatant $(n = 1.2)$ fluids trough isothermal cylindrical pipe at a simulation Reynolds number of 6500 by using the DNS approach with computational domain length of $20R$. The numerical resolution employed a grid consisting of $129 \times 129 \times 193$ points in the axial, radial, and circumferential directions, respectively.

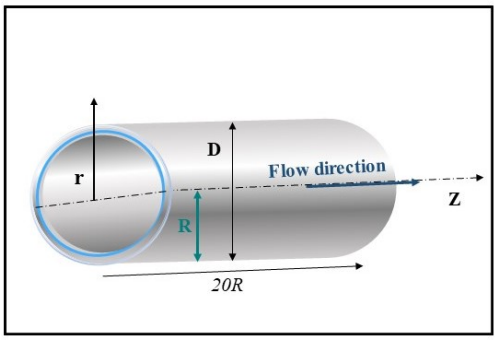

Figure III.1 – Geometry and computational domain of DNS.

III.3 Mathematical formulation

The conservation of mass, momentum and energy equations govern the flow of a non-Newtonian fluid are presented and written in dimensionless form as :

Continuity equation :

$$\frac{\partial u_i}{\partial x_j} = 0 \tag{III.1}$$

Momentum equations :

$$\frac{\partial u_j}{\partial t} + \frac{\partial (u_i u_j)}{\partial x_i} = -\frac{1}{\rho}\frac{\partial p}{\partial x_i} + \frac{\partial}{\partial x_i}\left[\nu\left(\frac{\partial u_i}{\partial x_j} + \frac{\partial u_j}{\partial x_i}\right)\right] \tag{III.2}$$

Energy equation :

$$\frac{DT}{Dt} = \frac{\lambda}{\rho C_P}\frac{\partial^2 T}{\partial x_i \partial x_j} + \frac{\mu}{2\rho C_p}\left(\frac{\partial u_i}{\partial x_j} + \frac{\partial u_j}{\partial x_i}\right) \tag{III.3}$$

The developments relating to the equations, which governing the phenomenon are reported in CHAPTER 4.

III.4 Results and discussion

III.4.1 Validation

The mean axial velocity profile for the Newtonian fluid have been compared reasonably with those available in the literature for validation purposes. Figure III.2 compares the results

of mean turbulent axial velocity profiles of the Newtonian $(n = 1)$ fluid with those of experimental PIV Eggels (1994) [43] and DNS of Redjem et al. (2007) [44] at $Reg = 5500$. As shown in Figure III.2, the predicted velocity profile of the Newtonian fluid agrees with the universal linear laws $U^+ = Y^+$ and $U^+ = 2.5lnY^+ + 5.5$ in the viscous sublayer $(0 \leq Y^+ \leq 5)$ and logarithmic region $(5 \leq Y^+ \leq 30)$, respectively.

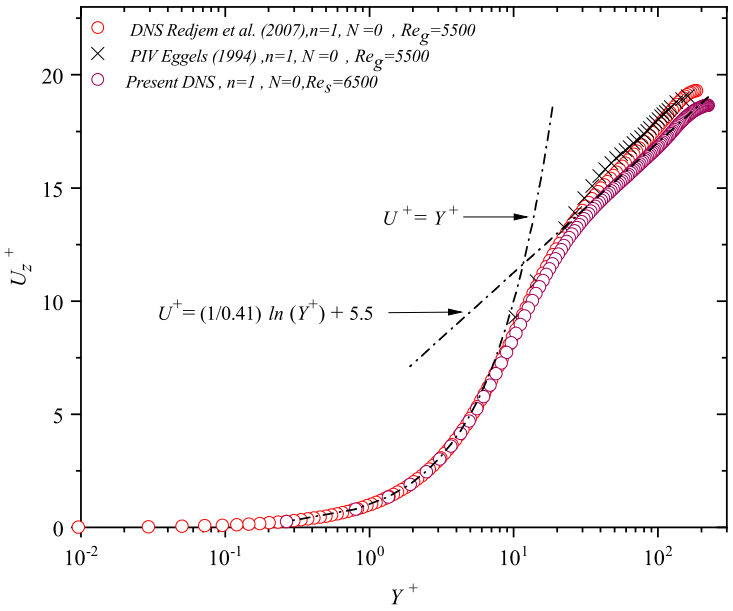

Figure III.2 – Validation of mean velocity profile in DNS.

The following paragraphs assess to reveal the effects of the behavior index on the mean characteristics to describe the flow patterns of the Ostwald de Waele fluids via analyzing and discussing the turbulent streamwise, radial and, tangential velocity distributions of the Pseudo-plastic $(n = 0.75)$, Newtonian $(n = 1)$, and Dilatant $(n = 1.2)$ fluids at a simulation Reynolds number of 6500 largely.

III.4.2 Mean axial velocity profile in DNS

Figure III.3 illustrates the turbulent axial velocity profiles along the pipe radius (R), scaled by the friction velocity $\left(U_\tau = \sqrt{\tau_W/\rho}\right)$ against the distance from the wall in wall units Y^+. The dashed lines represent the universal velocity distributions in the viscous sublayer $(0 \leq Y^+ \leq 5)$ and in the logarithmic layer $(30 \leq Y^+ \leq 200)$.

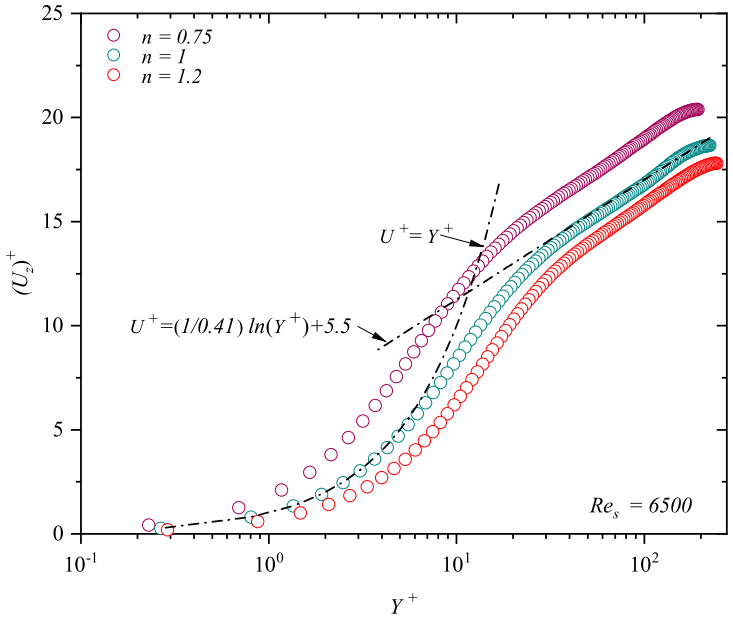

Figure III.3 – Mean axial velocity profile in DNS.

As shown in Figure III.3, the turbulent axial velocity profile of the Newtonian fluids is consistent with the universal velocity distributions in the viscous sublayer ; denoting a linear axial velocity distribution over the viscous sublayer is ascribed to the molecular shear-stress as the dominant force compared to the turbulent one in this region. Moreover, the Newtonian profile collapses very well with the universal law $U^+ = 2.5lnY^+ + 5.5$ in the core region. According to Figure III.3, the flow behavior index effect is nearly limited in the near-wall region ; it can be said that the turbulent streamwise velocity is almost independent of the flow behavior index (n) in the vicinity of the wall. The turbulent axial velocity profiles of Pseudoplastic and Dilatant fluids are almost identical in the near-wall region ; these profiles are consistent with each other in the viscous sublayer $(1 \leq Y^+)$. Moreover, these profiles collapse very well with the universal law $(U^+ = Y^+)$ in the vicinity of the wall $(0 \leq Y^+ \leq 5)$.

Further away from the near-wall region, the mean flow quantities strongly depend on the rheological properties of the Ostwald de Waele fluids ; the flow behavior index significantly affects the streamwise velocity distributions beyond the buffer region over the abovementioned conditions. It can be seen from Figure III.3 that beyond approximately $(Y^+ = 1)$, the axial velocity profiles begin to deviate gradually from each other with the distance from the wall (Y^+) ; this deviation is more pronounced far away from the wall towards the core region where the influence of the flow behavior index on the axial velocity distribution becomes more significant in the buffer

and logarithmic regions.

Beyond the buffer region, the streamwise velocity profile of the dilatant fluid lies down the Newtonian and Pseudoplastic profiles along the radial coordinate. In contrast, the velocity profile of the Pseudoplastic fluid is somewhat larger than the Newtonian and Dilatant fluids, which lie down the universal logarithmic law over the logarithmic layer. It should be noted that the decreased flow behavior index results in an increase in the turbulent axial velocity profile with the distance from the wall (Y^+) away from the wall towards the core flow region, where this trend is more pronounced in the logarithmic region $(30 \leq Y^+ \leq 200)$. It is interesting to note that this discrepancy is due to the influence of the apparent viscosity and shear-rate of the Ostwald de Waele fluids in this region ; the shear-rate of shear-thinning fluid $(n = 0.75)$ is higher than the Dilatant and Newtonian ones along the pipe radius, the enhancement in fluid shear-rate induces a noticeable increase in the movement of the fluid layers past each other away from the wall towards the core region with the wall distance, resulting a pronounced increase in the mean axial velocity along the pipe radius especially in the buffer layer and core region.

III.4.3 Turbulence intensities of velocity fluctuations in DNS

The current subsection evaluates the effect of the rheological behavior of the Ostwald de Waele fluids on the generation and transport of the turbulence intensities from the viscous sublayer towards the core region via analyzing and discussing the effects of the flow behavior index on the turbulence intensities of the velocity fluctuations.

Figure III.4a, Figure III.4b, and Figure III.4c depict the distribution of axial, radial and tangential velocity fluctuations, respectively, of Pseudoplastic $(n = 0.75)$, Newtonian $(n = 1)$, and Dilatant $(n = 1.2)$ fluids scaled by the friction velocity $U_\tau = \sqrt{\tau_W/\rho}$ along the pipe radius (R), versus the distance from the wall in wall units Y^+ at a simulation Reynolds number of 6500. As seen in Figure III.4a, the distribution of turbulence intensities of the axial velocity fluctuations of Pseudoplastic and Dilatant fluids exhibit a similar trend along the pipe radius, where there is a clear trend of oscillating in these profiles over the radial direction. The turbulence intensities of the axial component gradually enhance away from the wall with the wall distance. The profiles of the Pseudoplastic and Dilatant fluids differ considerably in the buffer $(5 \leq Y^+ \leq 30)$ and logarithmic $(30 \leq Y^+ \leq 200)$ regions where this discrepancy becomes more distinct in the core region. At large wall distance, RMS of the axial velocity fluctuations of the Pseudoplastic and Dilatant fluids begin to drop rapidly and fall off to lower values in the core region ; this means that the axial fluctuations begin to vanish gradually in this flow region.

As seen in Figure III.4a, the turbulence intensities profiles of the axial velocity fluctuations begin to deviate from each other further away from the wall towards the core region ; this deviation becomes more distinct with the distance from the wall (Y^+), especially in the logarithmic region. The RMS profiles of the Dilatant fluid lie above those of the Pseudoplastic and Newtonian fluids along the pipe radius. The increased flow behavior index results in a pronounced enhancement in the RMS of the axial velocity fluctuations beyond the buffer region $(5 \leq Y^+ \leq 30)$. It is evident that this increase in the flow behavior index also leads to a slight shift in the peak location of the profile away from the wall towards the core region. Moreover, the axial velocity fluctuations are generated near the wall. They are transported from the near-wall region towards the core region, it can be said that with an increasing flow behavior index, the generation of the axial velocity fluctuations enhances considerably. The increased flow behavior index also ameliorates the transport of the axial velocity fluctuations from the wall vicinity towards the core region.

As shown in Figure III.4b, the turbulence intensities of the radial velocity fluctuations are identical and are consistent with each other in the viscous sublayer for both flow behavior indices in the viscous sublayer $(0 \leq Y^+ \leq 5)$ up to approximately $Y^+ = 3$; these profiles are nearly linear and equal to zero value along the near-wall region $(Y^+ \leq 3)$. It can be said that the RMS of the radial component is almost independent of the flow behavior index in this flow region. These profiles begin to deviate from each other out of the viscous sublayer, where this deviation becomes more distinct further away from the wall towards the core region with wall distance ; where beyond $Y^+ = 3$, the profiles of the radial turbulence intensities exhibit a significant enhancement further away from the wall towards the core region. Moreover, the radial turbulence intensity profiles begin to decrease noticeably after reaching their peak values in the logarithmic region $(30 \leq Y^+ \leq 200)$.

It can be seen from Figure III.4b that the RMS of radial fluctuations profiles of the Dilatant fluid lies above those of the Pseudoplastic and Newtonian along the radial coordinate. It can be said that with increasing flow behavior index, the radial fluctuations enhance significantly along the pipe radius, and the predicted peak locations shift away towards the core region. It can be said that the increased flow behavior index results in a pronounced enhancement in the turbulence intensities of the radial velocity fluctuations along the pipe radius. In other words, the increased flow behavior index induces a noticeable enhancement in the transport mechanism of the turbulence intensities of the radial velocity fluctuations from the axial ones.

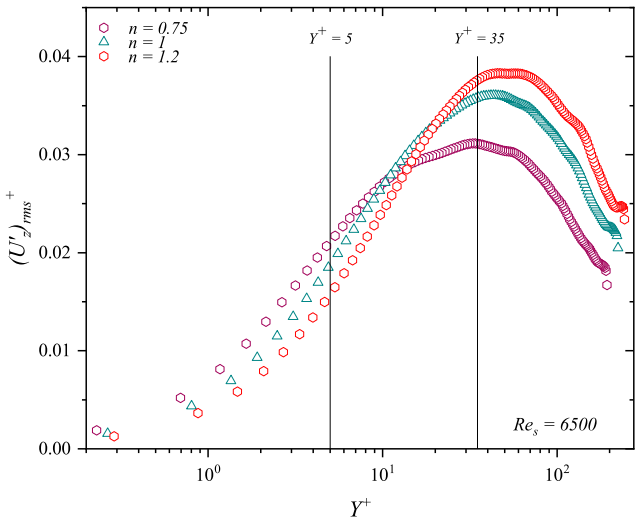

(a) RMS of axial velocity fluctuations

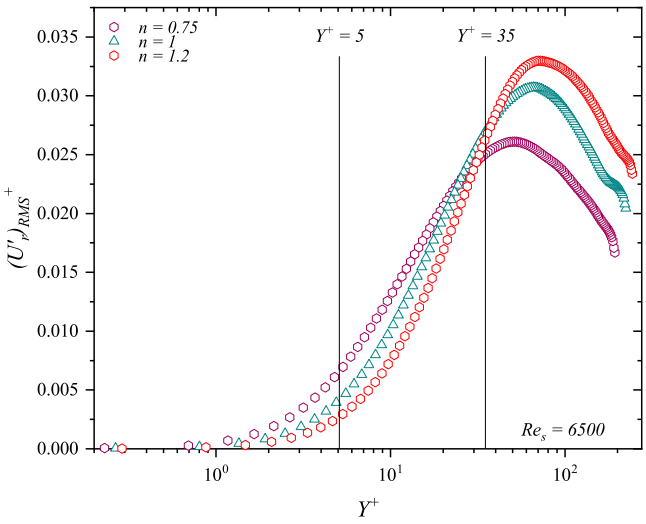

(b) RMS of radial velocity fluctuations

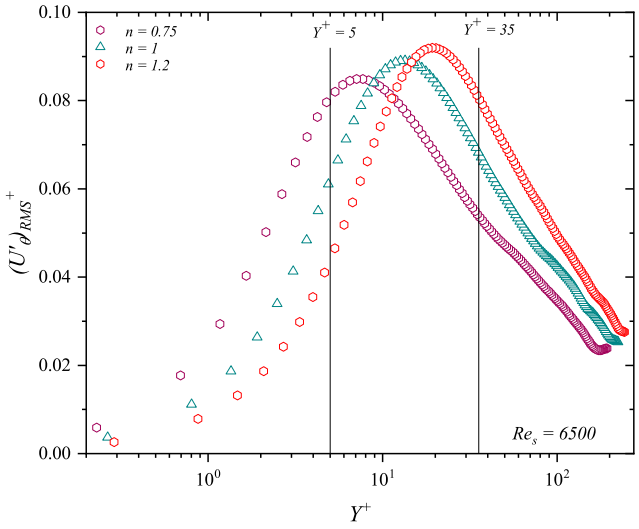

(c) RMS of tangential velocity fluctuations

Figure III.4 – Turbulence intensities of velocity fluctuations in DNS.

As shown in Figure III.4c, the same trend of RMS of tangential fluctuations is observed along the pipe radius for Pseudoplastic ($n = 0.75$), Newtonian ($n = 1$), and Dilatant ($n = 1.2$) fluids. The tangential fluctuations are almost neglected in the near-wall region, where this is ascribed to the molecular shear-stress being the dominant force compared to the turbulent one in this region. It can be seen from Figure III.4c that the RMS profiles of the Dilatant fluid lie above those of the Pseudoplastic and Newtonian along the radial coordinate, as the flow behavior index increases as the RMS of tangential fluctuations is enhanced along the pipe radius and their peak locations shift towards the core region. It is evident that the increased flow behavior

index induces a noticeable enhancement in the transfer of the tangential velocity fluctuations from the axial ones.

III.5 Conclusion

The present study aimed to investigate the effects of the flow behavior index of the Ostwald de Waele fluids on the rheological behavior, flow pattern, and turbulence statistics.
The results of this study will be summarized :

- The streamwise velocity increased gradually with decreasing flow behavior index along the pipe radius, especially in the core region.

- The increased flow behavior index resulted in a pronounced amelioration in the mechanism of generation of the axial fluctuations and a noticeable enhancement in the mechanism of the transport of the axial velocity fluctuations from the wall vicinity towards the core region.

- The increased flow behavior index led to ameliorating the transport mechanism of the radial and tangential velocity fluctuations from the axial velocity fluctuations and also to ameliorating the transport from the wall vicinity towards the core region.

CHAPTER IV

LES OF TURBULENT FLOW OF PSEUDOPLASTIC, NEWTONIAN AND DILATANT FLUIDS

- Introduction
- Problem description
- Mathematical formulation
- Results and discussion
- Conclusion

LES OF TURBULENT FLOW OF PSEUDOPLASTIC, NEWTONIAN, AND DILATANT FLUIDS

IV

IV.1 Introduction

The transfer of heat in a fluid flowing through a pipe is a fundamental problem in many engineering applications. In industrial processes, the transfer of heat is often accompanied by the transfer of mass, which can significantly affect the overall efficiency of the process. The rheological properties of the fluid play a crucial role in determining the heat transfer characteristics. Power-law fluids are a class of non-Newtonian fluids that exhibit a nonlinear relationship between the shear-stress and the shear-rate, and they are commonly encountered in many industrial applications. In recent years, Computational Fluid Dynamics (CFD) has emerged as a powerful tool for studying the flow behavior of power-law fluids. Large Eddy Simulations (LES) are a CFD technique used to simulate turbulent flows. LES divides the flow into large-scale and small-scale motions, and only resolves the large-scale motions while modelling the small-scale motions.

This study investigates the effect of Reynolds number on the rheological behavior of Ostwald–de Waele fluids in a straight pipe using Large Eddy Simulation (LES). The simulations are performed for three Reynolds numbers (4000, 8000 and 12000) and for different flow behavior indices (0.75, 1 and, 1.2), covering turbulent flow regimes. To compare the results of Newtonian and non-Newtonian fluids at the different Reynolds numbers a numerical resolution of 65^3 gridpoints was used in the r, θ, and z dimensions for the calculations, which employed a finite difference method. Significant variations were observed in the apparent viscosity and shear-rate, particularly at high Reynolds numbers, where the fluids exhibited non-Newtonian behavior with a pronounced decrease in apparent viscosity. Additionally, the study numerically analyzed the heat transfer characteristics of power-law fluids flowing in a heated horizontal pipe at isoflux conditions, using Large Eddy Simulations (LES) with an extended Smagorinsky model.

IV.2 Problem description

In this study, Large Eddy Simulation (LES) was used to investigate turbulent flow in a pipe with domain length of $(20R)$. To discretize the Navier-Stokes equations, a finite difference scheme that was second-order accurate in both space and time was employed. The convective and diffusive terms were evaluated using a combination of a third-order Runge-Kutta explicit scheme and a Crank-Nicholson implicit scheme. This approach allowed for an efficient and accurate simulation of the turbulent flow. To account for the effects of turbulent eddies that were smaller than the grid size, a dynamic model was employed as the sub-grid scale model.

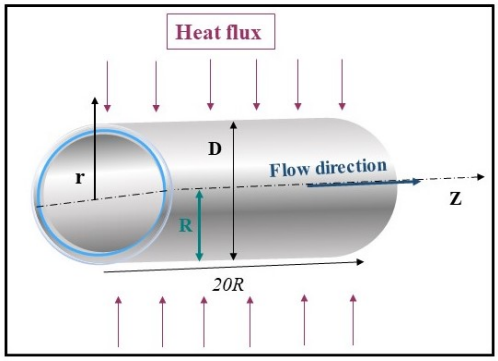

Figure IV.1 – Geometry and computational domain of LES.

IV.3 Governing equations

The conservation of mass, momentum, and energy equations governing the thermal flow of a non-Newtonian fluid are presented by Equations III.1, III.2 and III.3.

The kinematic viscosity is determined from the Ostwald de Waele model defined by :

$$\nu = \eta/\rho \text{ with } \eta = K_t \dot{\gamma}^{n-1} \tag{IV.1}$$

The filtered momentum Equation IV.1 governing incompressible Non-Newtonian fluid are written in a cylindrical coordinate system and are made dimensionless using the centreline axial velocity of the analytical fully developed laminar profile, $(U_{cL} = (3n+1)\,.U_b/(n+1))$ as a reference velocity.

$$x = \frac{x^*}{R}\ ,\ y = \frac{y^*}{R} \text{ and, } z = \frac{z^*}{R} \tag{IV.2}$$

$$u = \frac{u^*}{U_{cL}} \tag{IV.3}$$

$$p = \frac{p^*}{\rho U_{cL}} \tag{IV.4}$$

$$t = \frac{t^*}{t_{ch}} \text{ where } t_{ch} = \frac{R}{U_{cL}} \tag{IV.5}$$

$$\dot{\gamma} = \frac{U_{cL}}{R}\dot{\gamma}^* \tag{IV.6}$$

By introducing the dimensionless quantities as defined :

$$\frac{\partial u_j}{\partial t} + \frac{\partial (u_i u_j)}{\partial x_i} = \frac{\partial p}{\partial x_i} + \frac{1}{\mathrm{Re}_s}\frac{\partial}{\partial x_i}\left[\dot{\gamma}^{n-1}\left(\frac{\partial u_i}{\partial x_j} + \frac{\partial u_j}{\partial x_i}\right)\right] \tag{IV.7}$$

Where Re_s is the Reynolds number defined by :

$$\mathrm{Re}_s = \frac{\rho {U_{cL}}^{2-n} R^n}{K_t} \tag{IV.8}$$

Where $\dot{\gamma}$, S_{ij} are the shear-rate and the strain rate respectively :

$$\dot{\gamma} = \sqrt{2 S_{ij} S_{ij}} \tag{IV.9}$$

$$S_{ij} = \frac{1}{2}\left(\frac{\partial u_i}{\partial x_j} + \frac{\partial u_j}{\partial x_i}\right) \tag{IV.10}$$

Equations IV.7 is filtered using a generic spatial average filter on a cylindrical control volume :

$$\bar{q}(r,\theta,z) = \frac{1}{r\Delta r \Delta\theta \Delta z}\iiint q(r',\theta',z') r' \Delta r' \Delta\theta' \Delta z' \tag{IV.11}$$

The filtered equations are written :

$$\frac{\partial \overline{u_i}}{\partial x_i} = 0 \tag{IV.12}$$

$$\frac{\partial \bar{u}_j}{\partial t} + \frac{\partial \bar{u}_i \bar{u}_j}{\partial x_i} = -\frac{\partial \bar{p}}{\partial x_i} + \frac{1}{\mathrm{Re}_s}\frac{\partial}{\partial x_i}\left[\overline{\dot{\gamma}^{n-1}}\left(\frac{\partial \bar{u}_i}{\partial x_j} + \frac{\partial \bar{u}_j}{\partial x_i}\right) + \frac{\partial \bar{T}_{ij}}{\partial x_i}\right] - \frac{\partial \bar{\tau}_{ij}}{\partial x_i} \tag{IV.13}$$

Where $\bar{\tau}_{ij} = \overline{q_i q_j} - \overline{q_i q_j}$ is the sub-grid tensor and $\overline{T_{ij}} = \overline{\dot{\gamma}^{n-1}\frac{\partial q_i}{\partial x_j}} - \overline{\dot{\gamma}_{ij}^{n-1}\frac{\partial q_j}{\partial x_i}}$ is the additional sub-grid tensor for a non-Newtonian fluid.

The above dimensionless Equations IV.8, IV.9, and IV.10 are written in cylindrical coordinate

system with the following change of variables :

$$q_r = rv_r \ , \ q_\theta = rv_\theta \text{ and, } q_z = v_z \tag{IV.14}$$

This change of variables, taken from the work of Verzicco and Orlandi (1996), was chosen to avoid the singularity on the axis of the pipe ($r = 0$). Explaining Equations IV.14 and IV.13 in terms of the variables q_r, q_θ and q_z , we obtain :

$$\frac{\partial \bar{q}_r}{\partial r} + \frac{\partial \bar{q}_\theta}{\partial \theta} + r\frac{\partial \bar{q}_z}{\partial z} = 0 \tag{IV.15}$$

$$\begin{aligned}\frac{D\bar{q}_z}{Dt} = &\frac{\partial \bar{p}}{\partial z} + \frac{1}{\mathrm{Re}_s}\left[\frac{1}{r}\frac{\partial}{dr}\left(r\overline{\dot{\gamma}^{n-1}}\frac{\partial \bar{q}_z}{dr}\right) + \frac{1}{r^2}\frac{\partial}{d\theta}\left(r\overline{\dot{\gamma}^{n-1}}\frac{\partial \bar{q}_z}{d\theta}\right) + \frac{\partial}{\partial z}\left(r\overline{\dot{\gamma}^{n-1}}\frac{\partial \bar{q}_z}{dz}\right) + \right.\\ &\left.\frac{1}{r}\frac{\partial}{\partial r}\left(r\overline{T_{rz}}\right) + \frac{1}{r^2}\frac{\partial \overline{T_{\theta z}}}{\partial \theta} + \frac{\partial \overline{T_{zz}}}{\partial z}\right] - \frac{1}{r}\frac{\partial \bar{\tau}_{rz}}{\partial r} - \frac{1}{r^2}\frac{\partial \bar{\tau}_{\theta z}}{\partial \theta} - \frac{\partial \bar{\tau}_{zz}}{\partial z}\end{aligned} \tag{IV.16}$$

$$\begin{aligned}\frac{D\bar{q}_r}{Dt} = &-r\frac{\partial \bar{p}}{\partial r} + \frac{1}{\mathrm{Re}_s}\left[\frac{\partial}{dr}\left(r\overline{\dot{\gamma}^{n-1}}\frac{\partial \bar{q}_z/r}{dr} + \bar{T}_{rr}\right) - \left(\overline{\dot{\gamma}^{n-1}}\frac{\partial \bar{q}_r}{r^2} + \bar{T}_r\right) - \frac{2}{r^2}\right.\\ &\left.\left(\overline{\dot{\gamma}^{n-1}}\frac{\partial \bar{q}_\theta}{d\theta} + \bar{T}_{\theta\theta}\right) + \frac{1}{r^2}\frac{\partial}{\partial \theta}\left(\overline{\dot{\gamma}^{n-1}}\frac{\partial \bar{q}_r}{d\theta} + \bar{T}_{\theta r}\right) + \frac{\partial}{\partial z}\left(\overline{\dot{\gamma}^{n-1}}\frac{\partial \bar{q}_r}{dr} + \bar{T}_{zr}\right)\right] -\\ &\frac{\partial}{\partial r}\left(\frac{\partial \bar{\tau}_{rr}}{r}\right) - \frac{\partial \bar{\tau}_{\theta r}}{\partial \theta} - \frac{\partial \bar{\tau}_{rz}}{\partial z} + \frac{\partial \bar{\tau}_{\theta\theta}}{r^2}\end{aligned} \tag{IV.17}$$

$$\begin{aligned}\frac{D\bar{q}_\theta}{Dt} = &-\frac{\partial \bar{p}}{\partial \theta} + \frac{1}{\mathrm{Re}_s}\left[\frac{\partial}{\partial r}\left(r\overline{\dot{\gamma}^{n-1}}\frac{\partial\left(\bar{q}_\theta/r\right)}{\partial r}\right) - \left(\overline{\dot{\gamma}^{n-1}}\frac{\bar{q}_\theta}{r^2}\right) + \frac{1}{r^2}\frac{\partial}{\partial \theta}\left(\overline{\dot{\gamma}^{n-1}}\frac{\partial \bar{q}_\theta}{\partial \theta}\right) + \right.\\ &\left.\frac{\partial}{\partial z}\left(\overline{\dot{\gamma}^{n-1}}\frac{\partial \bar{q}_\theta}{\partial z}\right) + \frac{2}{r^2}\left(\overline{\dot{\gamma}^{n-1}}\frac{\partial \bar{q}_r}{\partial \theta}\right)\right] - \frac{\partial}{\partial r}\left(\frac{\partial \bar{\tau}_{r\theta}}{r}\right) - \frac{1}{r^2}\frac{\partial \bar{\tau}_{\theta\theta}}{\partial \theta} - \frac{\partial \bar{\tau}_{\theta z}}{\partial z} + \frac{\bar{\tau}_{\theta r}}{r}\end{aligned} \tag{IV.18}$$

With the temporal derivatives :

$$\frac{D\bar{q}_z}{Dt} = \frac{\partial \bar{q}_z}{\partial t} + \frac{1}{r}\frac{\partial\left(\bar{q}_z\bar{q}_r\right)}{\partial r} + \frac{1}{r^2}\frac{\partial\left(\bar{q}_\theta\bar{q}_z\right)}{\partial \theta} + \frac{\partial\left(\bar{q}_z\bar{q}_z\right)}{\partial r} \tag{IV.19}$$

$$\frac{D\bar{q}_r}{Dt} = \frac{\partial \bar{q}_r}{\partial t} + \frac{1}{r}\frac{\partial\left(\bar{q}_r\bar{q}_r/r\right)}{\partial r} + \frac{1}{r^2}\frac{\partial\left(\bar{q}_\theta\bar{q}_r\right)}{\partial \theta} + \frac{\partial\left(\bar{q}_r\bar{q}_z\right)}{\partial z} - \frac{\bar{q}_\theta\bar{q}_\theta}{r^2} \tag{IV.20}$$

$$\frac{D\bar{q}_\theta}{Dt} = \frac{\partial \bar{q}_\theta}{\partial t} + \frac{1}{r}\frac{\partial\left(\bar{q}_r\bar{q}_\theta/r\right)}{\partial r} + \frac{1}{r^2}\frac{\partial\left(\bar{q}_\theta\bar{q}_\theta\right)}{\partial \theta} + \frac{\partial\left(\bar{q}_\theta\bar{q}_z\right)}{\partial r} + \frac{\bar{q}_\theta\bar{q}_r}{r^2} \tag{IV.21}$$

The sub-grid stress tensor derived from convective terms :

$$\bar{\tau}_{rz} = \overline{q_r q_z} - \underset{\cdot r \cdot}{\bar{q}}\ \underset{z}{\bar{q}}\ , \bar{\tau}_{\theta z} = \overline{q_\theta q_z} - \bar{q}_\theta\bar{q}_z, \bar{\tau}_{zz} = \overline{q_z q_z} - \bar{q}_z\bar{q}_z \tag{IV.22}$$

$$\bar{\tau}_{r\theta} = \overline{q_r q_\theta} - \bar{q}_r\bar{q}_\theta, \bar{\tau}_{\theta\theta} = \overline{q_\theta q_\theta} - \bar{q}_\theta\bar{q}_\theta, \bar{\tau}_{rr} = \overline{q_r q_r} - \bar{q}_r\bar{q}_r \tag{IV.23}$$

The additional sub-grid stress tensor for non-Newtonian fluid (derived from viscous terms) :

$$\bar{T}_{rz} = \overline{\dot{\gamma}^{n-1}\frac{\partial q_z}{\partial r}} - \overline{\dot{\gamma}^{n-1}}\,\overline{\frac{\partial q_z}{\partial r}}, \bar{T}_{\theta z} = \overline{\dot{\gamma}^{n-1}\frac{\partial q_z}{\partial \theta}} - \overline{\dot{\gamma}^{n-1}}\,\overline{\frac{\partial q_z}{\partial \theta}} \tag{IV.24}$$

$$\bar{T}_{zz} = \overline{\dot{\gamma}^{n-1}\frac{\partial q_z}{\partial z}} - \overline{\dot{\gamma}^{n-1}}\,\overline{\frac{\partial q_z}{\partial z}}, \bar{T}_{rr} = \overline{\dot{\gamma}^{n-1}\frac{\partial \left(q_z/r\right)}{\partial r}} - \overline{\dot{\gamma}^{n-1}}\,\overline{\frac{\partial \left(q_z/r\right)}{\partial r}} \tag{IV.25}$$

$$\bar{T}_{\theta r} = \overline{\dot{\gamma}^{n-1}\frac{\partial \left(q_r/r\right)}{\partial \theta}} - \overline{\dot{\gamma}^{n-1}}\,\overline{\frac{\partial \left(q_r/r\right)}{\partial \theta}}, \bar{T}_{zr} = \overline{\dot{\gamma}^{n-1}\frac{\partial \left(q_r/r\right)}{\partial z}} - \overline{\dot{\gamma}^{n-1}}\,\overline{\frac{\partial \left(q_r/r\right)}{\partial r}} \tag{IV.26}$$

$$\bar{T}_{r\theta} = \overline{\dot{\gamma}^{n-1}\frac{\partial q_\theta}{\partial r}} - \overline{\dot{\gamma}^{n-1}}\,\overline{\frac{\partial q_\theta}{\partial r}}, \bar{T}_{\theta\theta} = \overline{\dot{\gamma}^{n-1}\frac{\partial q_\theta}{\partial \theta}} - \overline{\dot{\gamma}^{n-1}}\,\overline{\frac{\partial q_\theta}{\partial \theta}} \tag{IV.27}$$

$$\bar{T}_{z\theta} = \overline{\dot{\gamma}^{n-1}\frac{\partial q_\theta}{\partial z}} - \overline{\dot{\gamma}^{n-1}}\,\overline{\frac{\partial q_\theta}{\partial z}}, \bar{T}_{r} = \overline{\dot{\gamma}^{n-1}\frac{\partial q_r}{r^2}} - \overline{\dot{\gamma}^{n-1}}\,\frac{\bar{q}_r}{r^2} \tag{IV.28}$$

$$\bar{T}_{\theta} = \overline{\dot{\gamma}^{n-1}\frac{q_\theta}{r^2}} - \overline{\dot{\gamma}^{n-1}}\,\frac{\bar{q}_\theta}{r^2} \tag{IV.29}$$

Ohta and Miyashita (2014) [34] showed that $\bar{T}_r$ and $\bar{T}_\theta$ terms are very small and can be neglected in front of the terms that are the sub-grid tensors that model almost all the small scale effects. With this approximation, equations IV.15, IV.16 and IV.17 are in the following form :

$$\frac{\partial \bar{q}_r}{dr} + \frac{1}{r}\frac{\partial \bar{q}_\theta}{d\theta} + r\frac{\partial \bar{q}_z}{dz} = 0 \tag{IV.30}$$

$$\frac{D\bar{q}_z}{Dt} = \frac{\partial \bar{p}}{\partial z} + \frac{1}{\mathrm{Re}_s}\left[\frac{1}{r}\frac{\partial}{\partial r}\left(r\overline{\dot{\gamma}^{n-1}}\frac{\partial \bar{q}_z}{\partial r}\right) + \frac{1}{r^2}\frac{\partial}{\partial \theta}\left(r\overline{\dot{\gamma}^{n-1}}\frac{\partial \bar{q}_z}{\partial \theta}\right) + \frac{\partial}{\partial z}\left(r\overline{\dot{\gamma}^{n-1}}\frac{\partial \bar{q}_z}{\partial z}\right)\right] - \frac{1}{r}\frac{\partial \bar{\tau}_{rz}}{\partial r} - \frac{1}{r^2}\frac{\partial \bar{\tau}_{\theta z}}{\partial \theta} - \frac{\partial \bar{\tau}_{zz}}{\partial z} \tag{IV.31}$$

$$\frac{D\bar{q}_r}{Dt} = -r\frac{\partial \bar{p}}{\partial r} + \frac{1}{\mathrm{Re}_s}\left[\frac{\partial}{\partial r}\left(r\overline{\dot{\gamma}^{n-1}}\frac{\partial \left(\bar{q}_z/r\right)}{\partial r}\right) - \left(\overline{\dot{\gamma}^{n-1}}\frac{\bar{q}_r}{r^2}\right) - \frac{2}{r^2}\left(\overline{\dot{\gamma}^{n-1}}\frac{\partial \bar{q}_\theta}{\partial \theta}\right) + \frac{1}{r^2}\frac{\partial}{\partial \theta}\left(\overline{\dot{\gamma}^{n-1}}\frac{\partial \bar{q}_r}{\partial \theta}\right) + \frac{\partial}{\partial z}\left(\overline{\dot{\gamma}^{n-1}}\frac{\partial \bar{q}_r}{\partial r}\right)\right] - \frac{\partial}{\partial r}\left(\frac{\partial \bar{\tau}_{rr}}{r}\right) - \frac{\partial \bar{\tau}_{\theta r}}{\partial \theta} - \frac{\partial \bar{\tau}_{rz}}{\partial z} + \frac{\bar{\tau}_{\theta\theta}}{r^2} \tag{IV.32}$$

$$\frac{D\bar{q}_\theta}{Dt} = -\frac{\partial \bar{p}}{\partial \theta} + \frac{1}{\mathrm{Re}_s}\left[\frac{\partial}{\partial r}\left(r\overline{\dot{\gamma}^{n-1}}\frac{\partial \left(\bar{q}_\theta/r\right)}{\partial r}\right) - \left(\overline{\dot{\gamma}^{n-1}}\frac{\bar{q}_\theta}{r^2}\right) + \frac{1}{r^2}\frac{\partial}{\partial \theta}\left(\overline{\dot{\gamma}^{n-1}}\frac{\partial \bar{q}_\theta}{\partial \theta}\right) + \frac{\partial}{\partial z}\left(\overline{\dot{\gamma}^{n-1}}\frac{\partial \bar{q}_\theta}{\partial z}\right) + \frac{2}{r^2}\left(\overline{\dot{\gamma}^{n-1}}\frac{\partial \bar{q}_r}{\partial \theta}\right)\right] - \frac{\partial}{\partial r}\left(\frac{\partial \bar{\tau}_{r\theta}}{r}\right) - \frac{1}{r^2}\frac{\partial \bar{\tau}_{\theta\theta}}{\partial \theta} - \frac{\partial \bar{\tau}_{\theta z}}{\partial z} + \frac{\bar{\tau}_{\theta r}}{r} \tag{IV.33}$$

The energy equation as well as the thermal boundary conditions of the non-Newtonian fluid flow with heat transfer is written :

$$\frac{\partial T}{\partial t} + v_r\frac{\partial T}{\partial r} + \frac{v_\theta}{r}\frac{\partial T}{\partial \theta} + v_z\frac{\partial T}{\partial z} = \alpha\left[\frac{\partial^2 T}{\partial r^2} + \frac{1}{r}\frac{\partial T}{\partial r} + \frac{1}{r^2}\frac{\partial^2 T}{\partial \theta^2} + \frac{\partial^2 T}{\partial z^2}\right] \tag{IV.34}$$

Where α is the thermal diffusivity of the fluid is considered constant and independent of shear and temperature. This is because variations in thermal diffusivity with temperature or shear-rate are small compared to those of viscosity.

A heat flux density is imposed on the wall. This heat flux density condition requires that the wall temperature averaged in the azimuthal direction (θ) increases linearly in the flow direction (z).

The energy Equation IV.34 of the non-Newtonian fluid is made dimensionless using the reference temperature $T_{ref} = q_W/\rho C_p U_{cL}$. The dimensionless temperature is defined as :

$$\Theta = (\langle T_p(z)\rangle - T(\theta, r, z, t))/T_{ref} \tag{IV.35}$$

T_{ref} presents the reference temperature and is defined as T_{ref} where $\langle T_p(z)\rangle$ is an average in time and periodic directions.

Using the definition of temperature (given by Equation IV.35), the dimensionless form of the energy equation is as follows :

$$\begin{aligned}&\frac{\partial\Theta}{\partial t} + \frac{1}{r}\frac{\partial}{\partial r}(q_r\Theta) + \frac{1}{r}\frac{\partial}{\partial\theta}(q_\theta\Theta) + \frac{\partial}{\partial z}(q_z\Theta) - q_z\frac{\partial}{\partial z}\left(\frac{T_p}{T_{ref}}\right) = \frac{1}{\mathrm{Re}_s\mathrm{Pr}_s}\\ &\left[\frac{1}{r}\frac{\partial}{\partial r}\left(r\frac{\partial\Theta}{\partial r}\right) + \frac{1}{r^2}\frac{\partial^2\Theta}{\partial\theta^2} + \frac{\partial^2\Theta}{\partial z^2}\right]\end{aligned} \tag{IV.36}$$

By filtering Equation IV.36, the filtered energy equation is written :

$$\begin{aligned}&\frac{\partial\bar{\Theta}}{\partial t} + \frac{1}{r}\frac{\partial}{\partial r}\left(\bar{q}_r\bar{\Theta}\right) + \frac{1}{r}\frac{\partial}{\partial\theta}\left(\bar{q}_\theta\bar{\Theta}\right) + \frac{\partial}{\partial z}\left(\bar{q}_z\bar{\Theta}\right) - \bar{q}_z\frac{\partial}{\partial z}\left(\frac{T_p}{T_{ref}}\right) = \frac{1}{\mathrm{Re}_s\mathrm{Pr}_s}\\ &\left[\frac{1}{r}\frac{\partial}{\partial r}\left(r\frac{\partial\bar{\Theta}}{\partial r}\right) + \frac{1}{r^2}\frac{\partial^2\bar{\Theta}}{\partial\theta^2} + \frac{\partial^2\bar{\Theta}}{\partial z^2}\right] - \frac{1}{r}\frac{\partial\bar{\tau}_{\Theta r}}{\partial r} - \frac{1}{r}\frac{\partial\bar{\tau}_{\Theta\theta}}{\partial r} - \frac{1}{r}\frac{\partial\bar{\tau}_{\Theta z}}{\partial r}\end{aligned} \tag{IV.37}$$

Where the sub-grid terms or sub-grid heat fluxes are defined by :

$$\bar{\tau}_{r\Theta} = \overline{q_r\Theta} - \bar{q}_r\bar{\Theta}, \bar{\tau}_{\theta\Theta} = \overline{q_\theta\Theta} - \bar{q}_\theta\bar{\Theta}, \bar{\tau}_{z\Theta} = \overline{q_z\Theta} - \bar{q}_z\bar{\Theta} \tag{IV.38}$$

The simulation Prandtl number is given by :

$$\mathrm{Pr}_s = \frac{K_t}{\alpha\rho R^{n-1}{U_{cL}}^{1-n}} \tag{IV.39}$$

With K_t the consistency at temperature $\langle T_p \rangle$, the tensors $\bar{\tau}_{r\Theta}$, $\bar{\tau}_{\theta\,\Theta}$ and $\bar{\tau}_{z\Theta}$ are the sub-grid heat flux tensors.

The dimensionless equations governing the turbulent flow of the thermally-dependent Ostwald de Waele fluids $(Pn > 0)$ are written as follows :

Continuity equation :

$$\frac{\partial \bar{q}_r}{\partial r} + \frac{\partial \bar{q}_\theta}{\partial \theta} + r\frac{\partial \bar{q}_z}{\partial z} = 0 \tag{IV.40}$$

Momentum equations :

$$\begin{aligned}\frac{D\bar{q}_z}{Dt} = \frac{\partial \bar{p}}{\partial z} + \frac{1}{\mathrm{Re}_s}\left[\frac{1}{r}\frac{\partial}{dr}\left(r\overline{\dot{\gamma}^{n-1}}e^{Pn.\bar{\Theta}}\frac{\partial \bar{q}_z}{dr}\right) + \frac{1}{r^2}\frac{\partial}{d\vartheta}\left(r\overline{\dot{\gamma}^{n-1}}e^{Pn.\bar{\Theta}}\frac{\partial \bar{q}_z}{d\theta}\right)\right. \\ \left. + \frac{\partial}{\partial z}\left(r\overline{\dot{\gamma}^{n-1}}e^{Pn.\bar{\Theta}}\frac{\partial \bar{q}_z}{dz}\right)\right] - \frac{1}{r}\frac{\partial \bar{\tau}_{rz}}{\partial r} + \frac{1}{r^2}\frac{\partial \bar{\tau}_{\theta z}}{\partial \theta} + \frac{\partial \bar{\tau}_{zz}}{\partial z}\end{aligned} \tag{IV.41}$$

$$\begin{aligned}\frac{D\bar{q}_r}{Dt} = -r\frac{\partial \bar{p}}{\partial r} + \frac{1}{\mathrm{Re}_s}\left[\frac{\partial}{dr}\left(r\overline{\dot{\gamma}^{n-1}}e^{Pn.\bar{\Theta}}\frac{\partial \bar{q}_z/r}{dr}\right) - \left(\overline{\dot{\gamma}^{n-1}}\frac{\partial \bar{q}_r}{r^2}e^{Pn.\bar{\Theta}}\right) - \frac{2}{r^2}\left(\overline{\dot{\gamma}^{n-1}}e^{Pn.\bar{\Theta}}\frac{\partial \bar{q}_\theta}{d\theta}\right) + \right. \\ \left. \frac{1}{r^2}\frac{\partial}{\partial \theta}\left(\overline{\dot{\gamma}^{n-1}}\frac{\partial \bar{q}_r}{d\theta} + \bar{T}_{\theta r}\right) + \frac{\partial}{\partial z}\left(\overline{\dot{\gamma}^{n-1}}e^{Pn.\bar{\Theta}}\frac{\partial \bar{q}_r}{dr}\right)\right] - \frac{\partial}{\partial r}\left(\frac{\partial \bar{\tau}_{rr}}{r}\right) - \frac{\partial \bar{\tau}_{\theta r}}{\partial \theta} - \frac{\partial \bar{\tau}_{rz}}{\partial z} + \frac{\partial \bar{\tau}_{\theta\theta}}{r^2}\end{aligned} \tag{IV.42}$$

$$\begin{aligned}\frac{D\bar{q}_\theta}{Dt} = -\frac{\partial \bar{p}}{\partial \theta} + \frac{1}{\mathrm{Re}_s}\left[\frac{\partial}{dr}\left(r\overline{\dot{\gamma}^{n-1}}e^{Pn.\bar{\Theta}}\frac{\partial \bar{q}_\theta/r}{dr}\right) - \left(\overline{\dot{\gamma}^{n-1}}e^{Pn.\bar{\Theta}}\frac{\partial \bar{q}_\theta}{r^2}\right) + \frac{1}{r^2}\frac{\partial}{\partial \theta}\left(\overline{\dot{\gamma}^{n-1}}e^{Pn.\bar{\Theta}}\frac{\partial \bar{q}_\theta}{d\theta}\right) + \right. \\ \left. \frac{\partial}{\partial z}\left(\overline{\dot{\gamma}^{n-1}}e^{Pn.\bar{\Theta}}\frac{\partial \bar{q}_\theta}{dz}\right) + \frac{2}{r^2}\left(\overline{\dot{\gamma}^{n-1}}e^{Pn.\bar{\Theta}}\frac{\partial \bar{q}_r}{d\theta}\right)\right] - \frac{\partial}{\partial r}\left(\frac{\partial \bar{\tau}_{r\theta}}{r}\right) - \frac{1}{r^2}\frac{\partial \bar{\tau}_{\theta\theta}}{\partial \theta} - \frac{\partial \bar{\tau}_{\theta z}}{\partial z} - \frac{\partial \bar{\tau}_{\theta r}}{r}\end{aligned} \tag{IV.43}$$

Energy equation :

$$\begin{aligned}\frac{\partial \bar{\Theta}}{\partial t} + \frac{1}{r}\frac{\partial}{\partial r}\left(\bar{q}_r\bar{\Theta}\right) + \frac{1}{r}\frac{\partial}{\partial \theta}\left(\bar{q}_\theta\bar{\Theta}\right) + \frac{\partial}{\partial z}\left(\bar{q}_z\bar{\Theta}\right) - \bar{q}_z\frac{\partial}{\partial z}\left(\frac{T_p}{T_{ref}}\right) = \frac{1}{\mathrm{Re}_s\mathrm{Pr}_s}\left[\frac{1}{r}\frac{\partial}{\partial r}\left(r\frac{\partial \bar{\Theta}}{\partial r}\right) + \right. \\ \left. \frac{1}{r^2}\frac{\partial^2 \bar{\Theta}}{\partial \theta^2} + \frac{\partial^2 \bar{\Theta}}{\partial z^2}\right] - \frac{1}{r}\frac{\partial \bar{\tau}_{\Theta r}}{\partial r} - \frac{1}{r}\frac{\partial \bar{\tau}_{\Theta\theta}}{\partial r} - \frac{1}{r}\frac{\partial \bar{\tau}_{\Theta z}}{\partial r}\end{aligned} \tag{IV.44}$$

The sub-grid heat flux in the energy equation is modeled by :

$$\tau_{\Theta j} = -\alpha_t\frac{\partial \bar{\Theta}}{\partial x_j} \tag{IV.45}$$

$$\tau_{\Theta z} = -\alpha_t\frac{\partial \bar{\Theta}}{\partial z}, \tau_{\Theta r} = -\alpha_t\frac{\partial \bar{\Theta}}{\partial r}, \tau_{\Theta\theta} = -\alpha_t\frac{\partial \bar{\Theta}}{\partial \theta} \tag{IV.46}$$

With α_t is the turbulent thermal diffusivity coefficient defined by :

$$\alpha_t = \frac{\nu_t}{\mathrm{Pr}_t} \tag{IV.47}$$

Where Pr_t is the turbulent Prandtl number calculated by :

$$\mathrm{Pr}_t = \frac{\langle v'_r v'_z \rangle \frac{\partial T}{\partial r}}{\langle v'_r T \rangle \frac{\partial v_z}{\partial r}} \tag{IV.48}$$

IV.4 Results and discussion

IV.4.1 Hydrodynamic study of turbulent power-law fluids flow

IV.4.1.1 Mean normalized shear-rate and viscosity

The present subsection seeks to reveal the effect of the flow behavior index and Reynolds number on the rheological behavior by analyzing and discussing the evolution of the apparent fluid viscosity and the shear-rate of the Pseudoplastic and Dilatant fluids for various Reynolds values. The normalized apparent viscosity distributions of Pseudoplastic and Dilatant fluids along the pipe radius (R) versus the distance from the wall in wall units Y^+ are depicted in Figure IV.2. Figure IV.2a illustrates the flow behavior index effects on the shear-rate profiles at a simulation Reynolds number of 4000 and over a wide behavior index range of (0.75, 1 and 1.2), while that Figure IV.2b illustrates the Reynolds number effects on the shear-rate profiles for flow behavior index of 0.75, 1 and 1.2 over a Reynolds number range of (4000, 8000 and 12000).

Figure IV.2 demonstrates that the shear-rate is approximately linear and constant along the viscous sublayer $(0 \leq Y^+ \leq 5)$ for all flow behavior indices and each Reynolds number. Beyond $(Y^+ = 5)$, the shear-rate profiles begin to decline gradually as one moves away from the wall (Y^+) where this trend is more obvious in the buffer region $(5 \leq Y^+ \leq 30)$ for all considered cases. This reduction in the shear-rate away from the pipe wall towards the logarithmic region $(30 \leq Y^+ \leq 200)$ is related to the reduction in the viscous force far away from the near wall region towards the core flow region.

As shown in Figure IV.2, the shear-rate distributions seem strongly affected by the flow behavior index and the Reynolds number along the sublayer and buffer regions ; this effect seems less significant in the logarithmic region. The shear-rate profiles of Pseudoplastic lie above those of

Dilatant fluid along the pipe radius for three Reynolds number values (4000, 8000 and 12000), as shown in Figure IV.2b. It can be said that the decreased flow behavior index results in a marked increase in the shear-rate distributions over the three regions (sublayer, buffer, and logarithmic), especially in the near-wall region ; this trend is more pronounced as the Reynolds number increases.

On the other hand, the shear-rate profiles of Pseudoplastic and Dilatant fluids for the high Reynolds numbers (12000 and 8000) lie above those of Reynolds of 4000 along the pipe radius, where this trend is more obvious in the vicinity of the pipe wall for all flow behavior indices. The increased Reynolds number induces a marked increase in the shear-rate over the three regions, especially in the viscous sublayer.

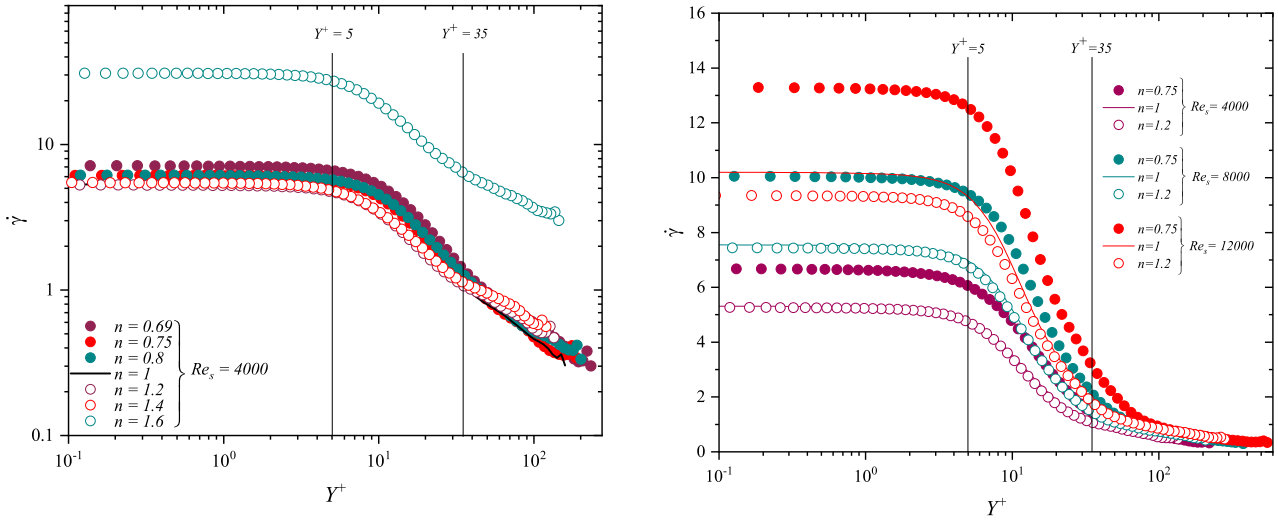

(a) **(b)**

Figure IV.2 – Shear-rate profile.

Figure IV.3 demonstrates the apparent normalized viscosity of the shear-thinning and shear-thickening fluids along the pipe radius against the distance from the wall in wall units (Y^+) at simulation Reynolds numbers of (4000, 8000 and 12000). As illustrated in Figure IV.3, no significant noteworthy differences are observed between the normalized apparent viscosity profile of Pseudoplastic and Dilatant fluids in the vicinity of the pipe wall where the apparent viscosity is independent of the flow behavior index and the Reynolds number near the wall region ; the apparent velocity profiles of the Pseudoplastic and Dilatant fluids collapse very well with each other in the viscous sublayer $(0 \leq Y^+ \leq 5)$. As shown in Figure IV.2, the apparent viscosity is identical and equal to the apparent viscosity at the pipe wall (η_w) over the viscous sublayer

$(0 \leq Y^+ \leq 5)$, for all flow behavior indices and Reynolds numbers. Beyond $(Y^+ = 5)$, the apparent viscosity profiles begin to deviate gradually from each other with the distance from the wall (Y^+) ; this deviation is more pronounced far away from the wall towards the core region, where the influence of the flow behavior index on the apparent viscosity distribution becomes more significant in the logarithmic region. The viscosity of the Pseudoplastic fluid increases gradually with the wall distance towards the core region, where this increase is more apparent as the flow behavior index decreases for all Reynolds numbers. It can be said that the reduced flow behavior index results in a marked increase in the apparent viscosity far away from the near-wall region. As shown in Figure IV.2, the shear-rate decreases gradually with the wall distance far away from the pipe wall towards the core region ; this reduction results in a gradual increase in the apparent viscosity of the Pseudoplastic fluid beyond the sublayer region where the Pseudoplastic fluid tends to behave like a solid when approaching to the pipe centre.

On the contrary, the apparent viscosity Dilatant decreases gradually with the wall distance far from the pipe wall for all Reynolds numbers ; this trend is more pronounced as the flow behavior index. The increased flow behavior index induces a noticeable reduction in the apparent viscosity far from the near wall region, especially in the logarithmic region. As shown in Figure IV.2, the decreased shear-rate far away from the vicinity of the wall induces a marked decrease in the apparent viscosity of the Dilatant fluid with the wall distance towards the logarithmic region.

On the other hand, it is apparent in Figure IV.3 that no significant noteworthy differences are observed between the normalized apparent viscosity profile of various Reynolds numbers (4000, 8000 and 12000) along the pipe radius ; the viscosity profiles are nearly consistent with each other along the pipe radius for each Reynolds number. It can be said that the apparent viscosity of the Pseudoplastic and Dilatant seem independent of the Reynolds number over the

Figure IV.4 presents the distribution of apparent fluid viscosity normalized by viscosity at the wall (η_w), against the shear-rate scaled by the shear-rate at the pipe wall $(\dot{\gamma}_w)$ at simulation Reynolds number of 4000, 8000 and 12000 and over a wide behavior index range of (0.75, 1 and 1.2). As shown in Figure IV.4, the Newtonian fluid's apparent viscosity is constant along the pipe radius and equal to the wall viscosity, so it is independent of shear flow rates and Reynolds number. The apparent viscosity of the Pseudoplastic and Dilatant fluids are strongly related to the shear-rate over the three regions (sublayer, buffer, and logarithmic). The apparent viscosity varies gradually with the shear-rate along the pipe radius for all flow behavior indices.

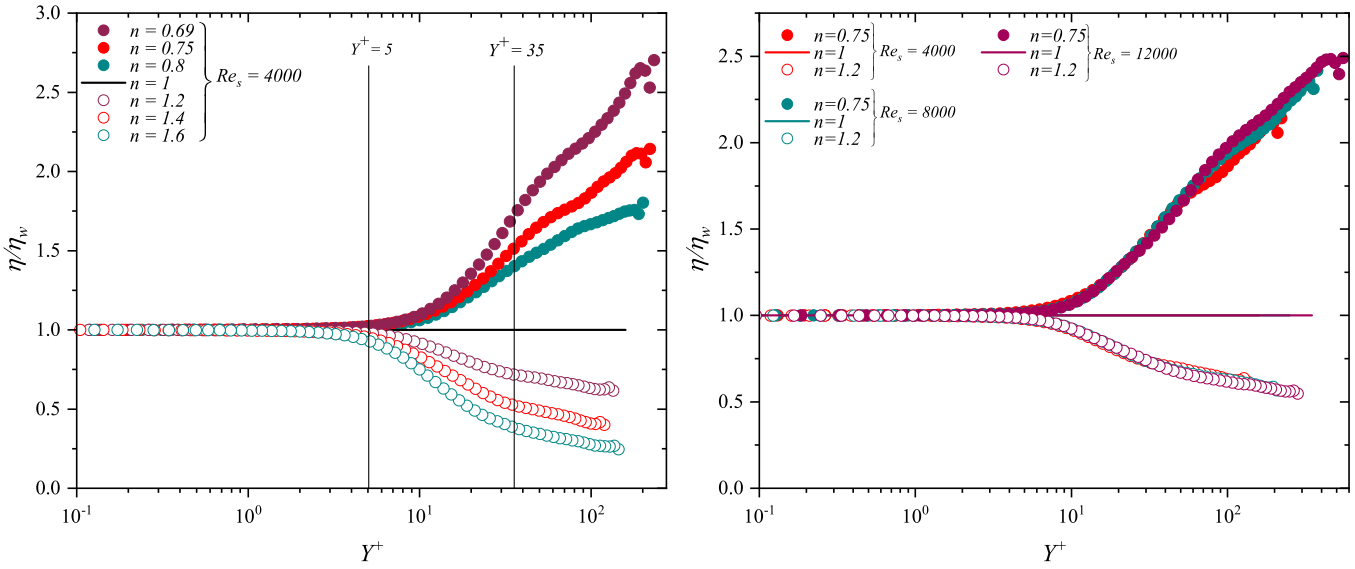

(a) **(b)**

Figure IV.3 – Apparent viscosity profile versus Y^+ in LES.

As shown in Figure IV.4, the apparent viscosity of the Pseudoplastic fluid is inversely proportional to the shear-rate ; the increased shear-rate leads to a decrease in the apparent viscosity of the Pseudoplastic where this trend is more apparent as the flow behavior decreases for all Reynolds numbers. It should also be noted that this finding confirms the association between the apparent fluid viscosity and the shear-rate of the Pseudoplastic fluids where $\eta = K\dot{\gamma}^{n-1}$. On the contrary, the apparent viscosity of the Dilatant fluid is directly proportional to the shear-rate. The viscosity profiles increase gradually with the increase in the shear-rate, where this trend is more apparent as the flow behavior decreases for all Reynolds numbers. This finding confirms the association between the apparent fluid viscosity and the shear-rate of the Dilatant fluids where $\eta = K\dot{\gamma}^{n-1}$. It is clearly apparent in Figure IV.3. that no significant noteworthy differences are observed between the apparent viscosity profile of the Pseudoplastic and Dilatant fluids for the Reynolds number range (4000, 8000 and 12000) along the pipe radius. It can be said that the relation between the apparent viscosity and shear-rate is nearly independent of the Reynolds number over the three regions (sublayer, buffer, and logarithmic).

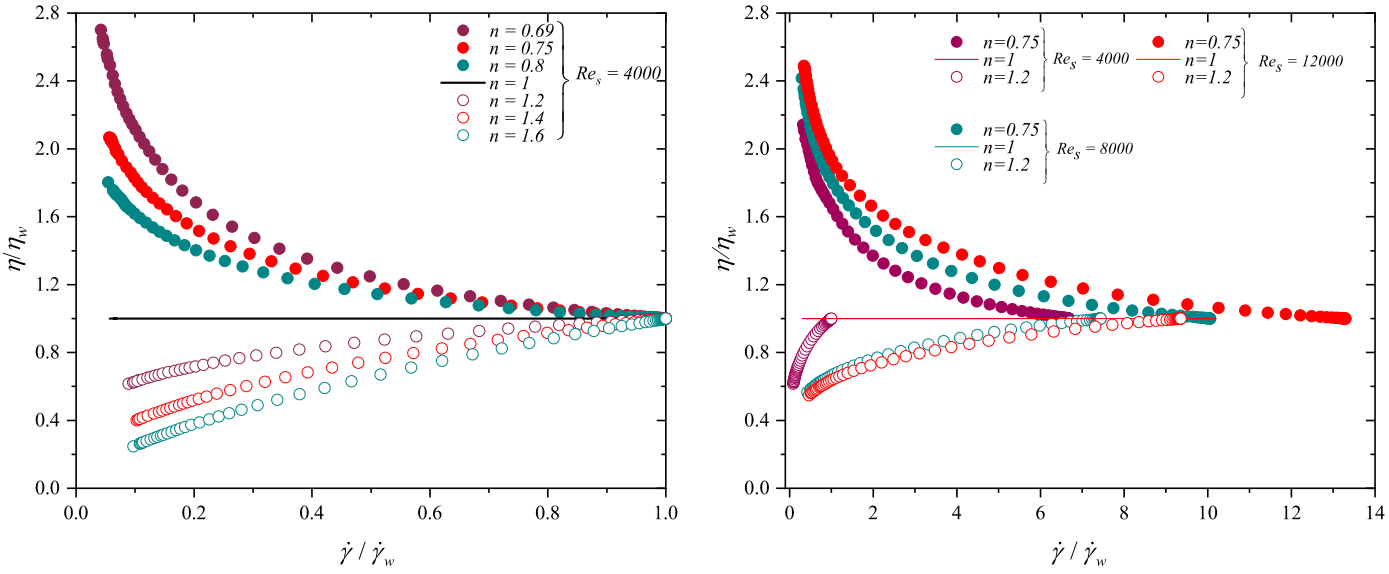

(a) **(b)**

Figure IV.4 – Apparent viscosity versus shear-rate.

IV.4.1.2 Turbulent axial velocity profile in LES

The reliability and accuracy of the predicted results and numerical procedure are examined by comparing the present findings to those available in the literature. The validation study compares the axial velocity of Pseudoplastic $(n = 0.75)$ and Newtonian fluid through stationary pipe to those of experimental *PIV*, and *LES*. Figure IV.5a reasonably compares the turbulent axial velocity profiles of the Newtonian $(n = 1)$ fluid through an axially stationary pipe with the *LES* of Abdi et al. (2019) [42] at the simulation Reynolds number of 4000, experimental *PIV* of Eggels (1994) [43]. It can be seen from that no significant differences were found between the present predicted velocity profile of Pseudoplastic and Newtonian fluids through stationary $(N = 0)$ with those of the literature along the radius pipe, where the streamwise velocity profiles turn out to be in excellent agreement with Abdi et al. (2019) [42], experimental *PIV* of Eggels (1994) [43]. Moreover, these profiles collapse very well with the universal law $(U^+ = Y^+)$ in the vicinity of the wall and $(U^+ = 2.5 \ln Y^+ + 5.5)$ in the logarithmic region.

Figure IV.5b compares the turbulent axial velocity profiles of the shear-thinning $(n = 0.75)$ fluid through a stationary $(N = 0)$ with *LES* of Abdi et al. (2019) [42] at the simulation Reynolds number of 4000 and experimental data of Rudman et al. (2004) [45] for a generalized Reynolds number. As shown in Figure IV.5b, the predicted turbulent axial velocity profile of

Pseudoplastic fluid is very similar to those found by Abdi et al. (2019) [42] and Rudman et al. (2004) [45] along the three layers.

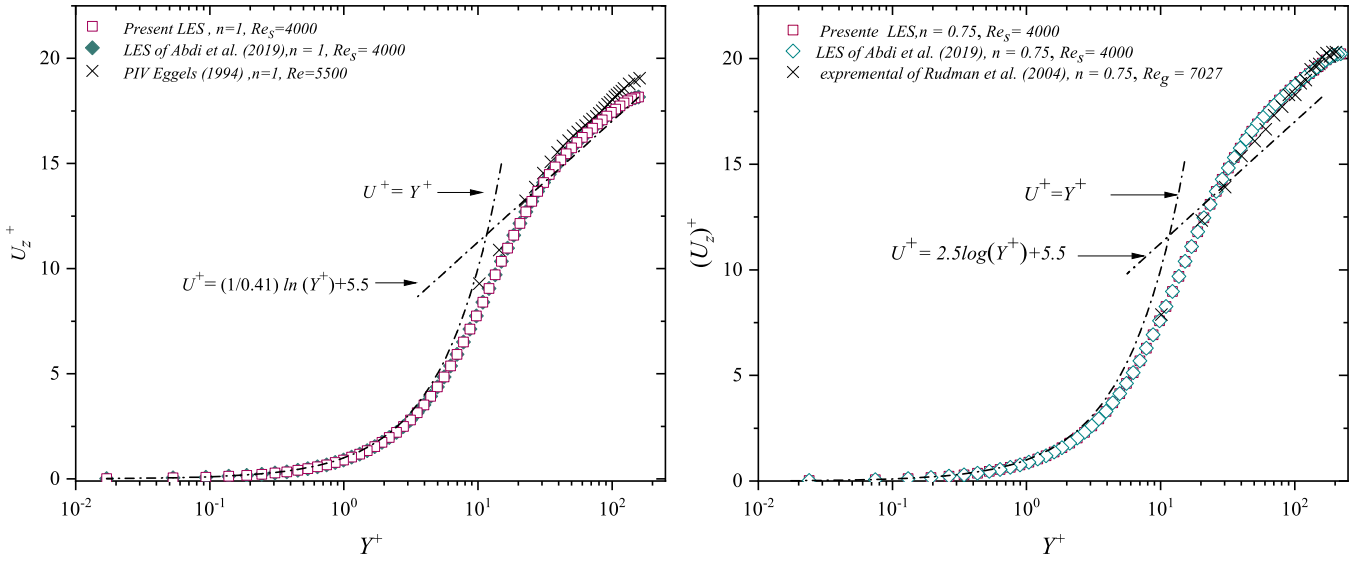

(a) **(b)**

Figure IV.5 – Validation of turbulent axial velocity in LES.

The present subsection aims to explore the effects of the rheological behavior of the power-law fluid on the flow pattern and turbulence features by critically examining the effects of the flow behavior index and Reynolds number on the hydrodynamic and the turbulence characteristics, especially in the core region and the vicinity of the wall. The present study assesses to reveal the effects of the flow behavior of Pseudoplastic and Dilatant fluids and Reynolds number on the turbulent and mean axial velocity profiles over a wide behavior index range of (0.75, 1 and 1.2) for three Reynolds number values (4000, 8000 and 12000).

Figure IV.6 illustrates the turbulent axial velocity profiles along the pipe radius (R), scaled by the friction velocity $(U_\tau = \sqrt{\tau_W/\rho})$ against the distance from the wall in wall units Y^+. The dashed lines represent the universal velocity distributions in the viscous sublayer $(0 \leq Y^+ \leq 5)$ and the logarithmic layer $(30 \leq Y^+ \leq 200)$. It can be seen from Figure IV.6 that the axial velocity is nearly independent of the flow behavior index (n) and the Reynolds number in the near-wall region for all considered cases. In the viscous sublayer , the turbulent axial velocity profiles of Pseudoplastic $(n < 1)$, Newtonian $(n = 1)$, and Dilatant $(n > 1)$ fluids are almost identical are consistent with each along the viscous sublayer for the three Reynolds number (4000, 8000 and 12000). Moreover, these profiles collapse very well with the universal

law $(U^+ = Y^+)$ in the vicinity of the wall $(0 \leq Y^+ \leq 5)$ denoting a linear axial velocity distribution over the viscous sublayer for all considered cases. The linear distribution of the turbulent axial velocity in the near-wall region results because the molecular viscous force is the dominant force compared to the turbulent one in this region.

As shown in Figure IV.6, the effects of the flow behavior index and Reynolds number become to be significant with the wall distance (Y^+) in the buffer region $(5 \leq Y^+ \leq 30)$. Beyond approximately $(Y^+ = 10)$, the velocity profiles begin to deviate slightly from each other with the wall distance far away from the near-wall region towards the core region. This deviation is more pronounced far from the wall towards the core region, where the influence of the flow behavior index on the axial velocity distribution becomes more significant in the logarithmic region $(30 \leq Y^+ \leq 200)$. As shown in Figure IV.6, a stronger dependence of the axial and radial velocity profiles on the flow behavior index and Reynolds number is marked outer the buffer region $(5 \leq Y^+ \leq 30)$. The turbulent axial velocity profiles of the Pseudoplastic and Dilatant fluids deviate pronouncedly from each other in the logarithmic region for all Reynolds numbers ; this discrepancy is due to the flow behavior index effects in the core region where the turbulent viscous force is the dominant force compared to the molecular one. It should be noted that the deviation in the axial velocity profile is more pronounced for the high Reynolds number $(Re = 12000)$, where the increased Reynolds number leads to deviating the axial velocity profile significantly in the core region.

The Newtonian fluid's turbulent mean axial velocity profile collapses totally with the universal logarithmic law $U^+ = 2.5lnY^+ + 5.5$ in the logarithmic layer. The turbulent axial velocity profiles of the Pseudoplastic fluid are somewhat larger than the Newtonian fluid and lie above the universal logarithmic law over the logarithmic layer, While the profiles of the shear-thickening lie down the universal logarithmic law in the core region. It can be seen from Figure IV.6 that the axial velocity profiles of the Pseudoplastic fluids are more important than those of Dilatant fluids. As depicted in Figure IV.6, the velocity profile increases gradually with the wall distance towards the core region ; this increase in these profiles seems more noticeable as the flow behavior index decreases in the logarithmic region. The reduced flow behavior index results in a marked increase in the axial velocity profile along the pipe radius, especially in the logarithmic region for the three Reynolds number values (4000, 8000 and 12000). As shown in Figure IV.6b, the increased Reynolds number increases the velocity profile as the flow behavior index is reduced.

It is interesting to note that this discrepancy in the turbulent axial velocity, especially far away from the near-wall region, is due to the influence of the flow behavior index and Reynolds number on the shear-rate distribution and the fluid viscosity along the pipe radius. For Pseudoplastic fluid, the decreased flow behavior induces a pronounced increase in the apparent viscosity beyond the buffer region ($Y^+ = 5$) towards the core region Figure IV.4a, resulting in a pronounced decrease in the shear-rate along the logarithmic region (Figure IV.2a). Consequently, results in a noticeable increase in the axial velocity profile in the core region, this trend is more pronounced as the flow behavior index decreases.

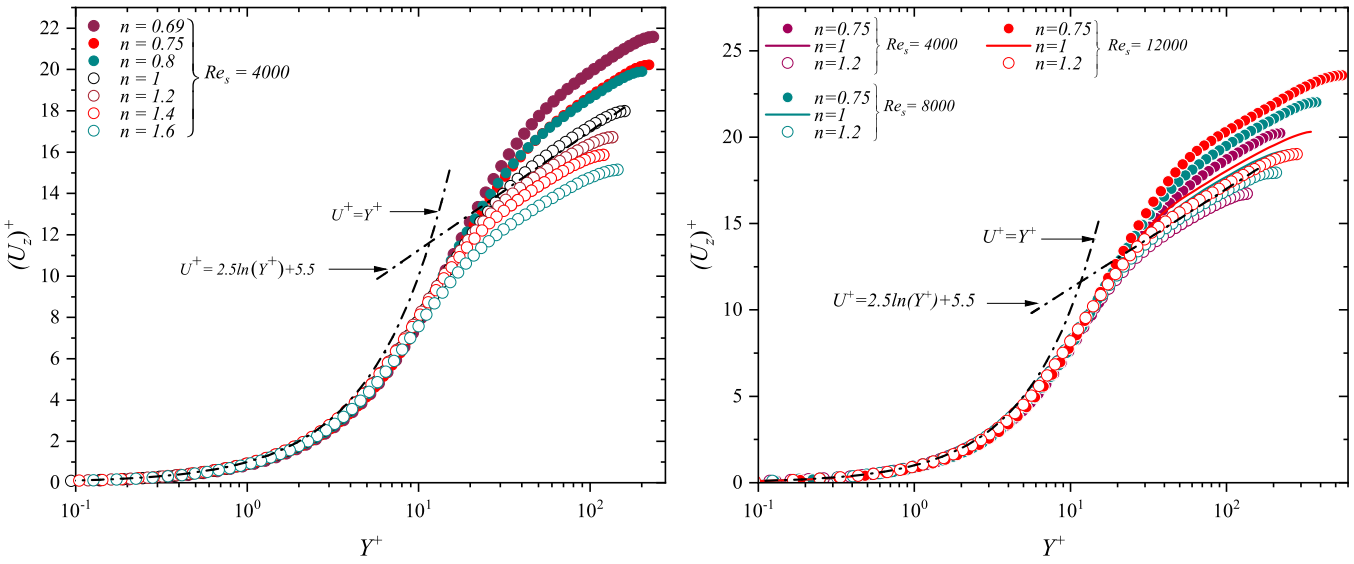

(a) **(b)**

Figure IV.6 – Turbulent axial velocity profiles in LES.

As depicted in Figure IV.4a, the apparent viscosity of the Dilatant fluid decreases gradually with the wall distance towards the core region, resulting in a noticeable increase in the shear-rate of the Dilatant fluid over the logarithmic region (Figure IV.3a) and, consequently, results in a pronounced decrease in the turbulent axial velocity profile in the core region (Figure IV.6), this trend is more apparent as the flow behavior index increases. As for the Reynolds number effects, the increased Reynolds number results in a marked decrease in the apparent viscosity (Figure IV.4b), resulting in a noticeable reduction in the shear-rate of the Pseudoplastic fluid (Figure IV.3b) and, consequently, results in a pronounced increase in the axial velocity profile of the Pseudoplastic fluid in the core region (Figure IV.6b). On the contrary, the increased Reynolds number induces in an evident decrease in the apparent viscosity of the Dilatant fluid (Figure IV.4b), resulting in an apparent increase in the shear-rate (Figure IV.3b) and consequently,

results in a pronounced decrease in the axial velocity profile along the logarithmic region (Figure IV.6b).

Figure IV.7 presents the streamwise velocity profiles along the pipe radius of Pseudoplastic and Dilatant fluids, in addition to the analytical velocity profile in the laminar regime for both fluids scaled by the analytical laminar centreline velocity ($U_{cL} = (3n+1)\,U_b/\,(n+1)$), against the distance from the wall (y), normalized by the pipe radius, over a wide behavior index range of (0.75, 1 and 1.2) for three Reynolds number values (4000, 8000 and 12000). As shown in Figure IV.7, the mean axial velocity profile of the Pseudoplastic and Dilatant fluids is similar to the laminar profile where a parabolic shape characterises these profiles ; the velocity profile in the laminar flow is pronouncedly higher than the others in the turbulent flow.

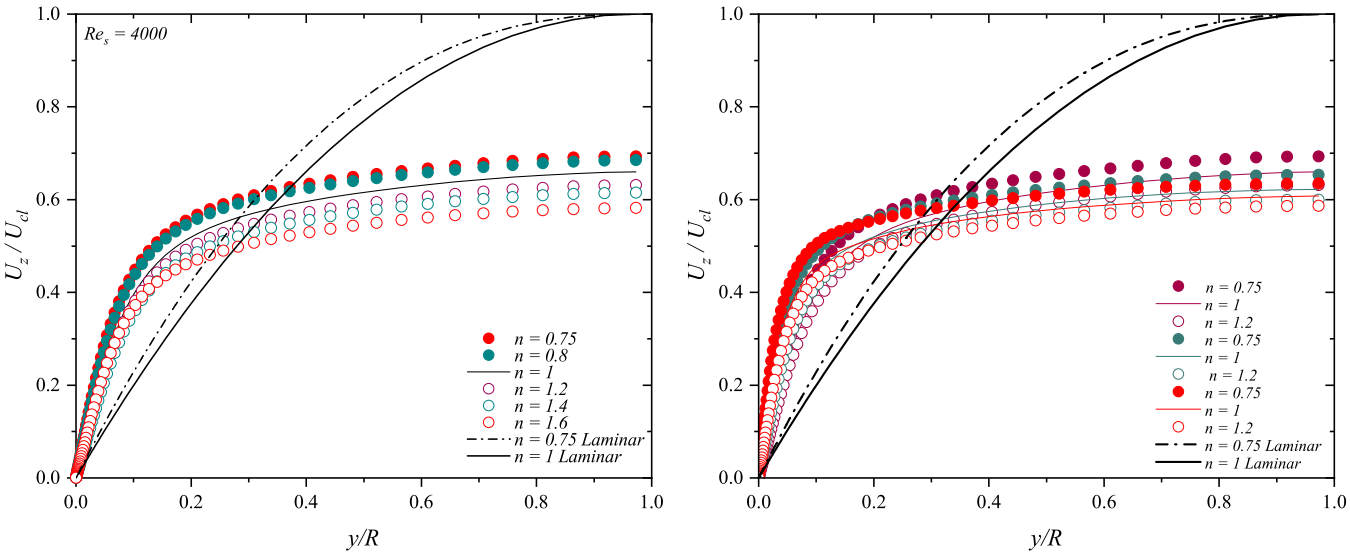

(a) **(b)**

Figure IV.7 – Turbulent axial velocity profils versus y/R in LES.

As discussed in Figure IV.6, the flow behavior index and Reynolds number significantly affect on the axial velocity distribution along the pipe radius espically in the core region where the decreased flow behavior index results in marked increase in the velocity in the logarithmic region and this trend is more obvious as the Reynolds number increases. As mentioned above, the deviations in the axial velocity profiles are due to the effects of the flow behavior index and Reynolds number on the apparent viscosity and the shear-rate distribution along the logarithmic region Pseudoplastic and Dilatant fluids.

IV.4.1.3 Turbulence intensities of velocity fluctuations in LES

Figure IV.8a and Figure IV.8b compare the normalized root mean square (RMS) of the axial, radial and tangential velocity fluctuations of the shear-thinning $(n = 0.75)$ and Newtonian fluids along the pipe radius for the stationary pipe. These profiles have been compared reasonably with the LES of Abdi et al. (2019) [42] at the simulation Reynolds number of 4000. As shown in Figure IV.8, the predicted RMS profiles of the shear-thinning are in excellent agreement with those of Abdi et al. (2019) [42] along the pipe radius in the three sublayers.

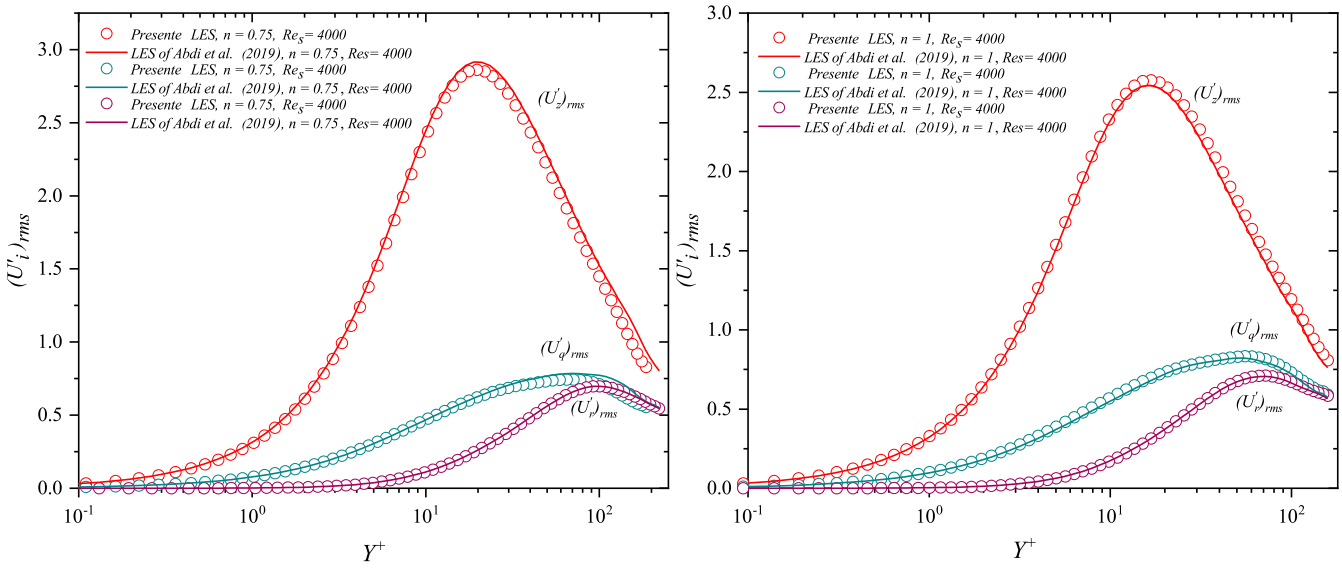

(a) **(b)**

Figure IV.8 – Validation of turbulence intensities in velocity fluctuations in LES.

The current subsection aims to describe the turbulence feature of the Pseudoplastic and Dilatant fluids by analyzing and discussing the effects of the flow behavior index of the Pseudoplastic and Dilatant fluids in addition to the effects of the Reynolds number on the generation and transport mechanism of turbulence intensities of the velocity fluctuation from the wall vicinity towards the core region.

Figure IV.9, Figure IV.10, and Figure IV.11 illustrate the flow behavior index and Reynolds number effects on the turbulence intensities of the velocity fluctuations over a wide behavior index range of (0.75, 1 and 1.2) for three Reynolds number values of (4000, 8000 and 12000). The Figure IV.9, Figure IV.10, and Figure IV.11 depict, respectively the root mean square (RMS) distribution of the axial, radial, and tangential velocity fluctuations of Pseudoplastic

and Dilatant fluids, scaled by the friction velocity $U_\tau = \sqrt{\tau_W/\rho}$ along the pipe radius (R), versus the distance from the wall in wall units Y^+. The flow behavior index and the Reynolds number affects significantly on the turbulence intensities of the axial, radial, and tangential velocity fluctuations along the pipe radius, especially in the logarithmic region. The generation and transport mechanism of turbulence intensities of the velocity fluctuation from the wall vicinity towards the core region strongly depends on the flow behavior index and Reynolds number.

It can be seen from Figure IV.9 that the RMS of the axial velocity fluctuations increases gradually with the wall distance far away from the pipe wall towards the core region ; this increase is more obvious beyond the buffer region until reach its peak at a large wall distance, these velocity fluctuations begin to drop rapidly and fall off to lower values in the core region for all considered cases. This means that the axial velocity fluctuations are generated in the vicinity of the wall and transported towards the buffer region $(5 \leq Y^+ \leq 30)$; these axial fluctuations become to vanish gradually at a large wall distance for all flow behavior indices and Reynolds numbers. As shown in Figure IV.9, the RMS axial velocity fluctuations profiles are nearly independent of the flow behavior index and Reynolds number near-wall region, where these profiles are almost identical and consistent with each other along the viscous sublayer $(0 \leq Y^+ \leq 5)$, meaning that the axial velocity fluctuations generation is independent of the flow behavior index and Reynolds number. These profiles deviate significantly from each other beyond the buffer region, and this deviation becomes more distinct with the distance from the wall (Y^+), for all Reynolds numbers. As shown in Figure IV.9, the RMS of the axial velocity fluctuations profiles of the Pseudoplastic lie above those of Dilatant fluids, where the turbulence intensities of the axial velocity fluctuations of Pseudoplastic fluid are somewhat higher than the corresponding RMS for Dilatant fluids for three values of Reynolds numbers. As depicted in Figure IV.9b, the RMS axial velocity fluctuations profiles of the high Reynolds number lie above those of lower values. As the Reynolds number increases, the RMS profiles become larger with the wall distance, especially in the buffer region, for all flow behavior indices.

It can be said that decreased flow behavior index results in a noticeable increase in the turbulence intensities of the axial velocity fluctuations along the pipe radius, especially in the buffer region, resulting in a noticeable enhancement in the generation and transport mechanism of turbulence intensities of the velocity fluctuation from the wall vicinity towards the core region, and this trend is more pronounced as the Reynolds number increases. This enhancement is attributed to the effects of the flow behavior index and the turbulent axial velocity distributions along the pipe radius. As discussed above (Figure IV.6), the increased flow behavior index of the

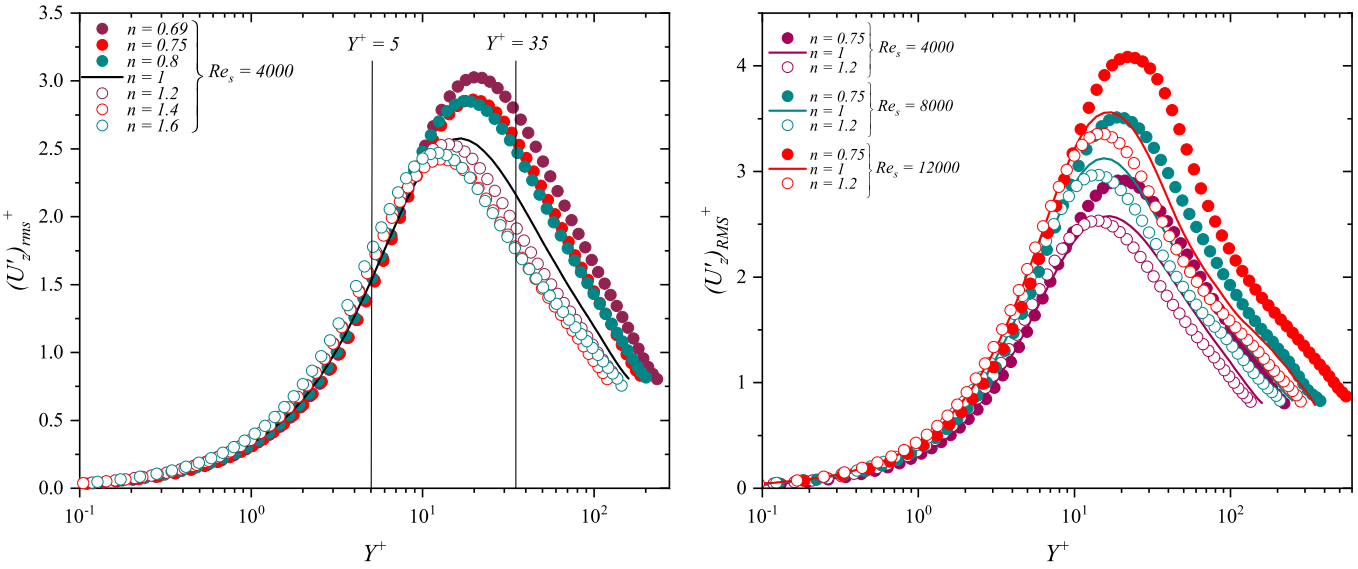

(a) **(b)**

Figure IV.9 – RMS of axial velocity in LES.

Pseudoplastic and Dilatant fluid results in a noticeable increase in the axial velocity in the core region, resulting in a marked improvement in the generation and transport mechanism of turbulence intensities of the velocity fluctuation from the wall vicinity towards the core region, and this trend is more pronounced as the Reynolds number increases. It can be seen from Figure IV.10 that the turbulence intensities of the radial velocity fluctuations are identical and consistent with each other in the viscous sublayer ; these profiles are nearly linear and equal to zero value along the near-wall region $(0 \leq Y^+ \leq 5)$ up to approximately $Y^+ = 3$, for all flow behavior indices and Reynolds numbers. The RMS profiles of the radial component begin to deviate from each other out of the viscous sublayer, where this deviation becomes more distinct away from the wall towards the core region with wall distance. As shown in Figure IV.10, the radial turbulence intensity profiles begin to decrease noticeably after reaching their peak values in the logarithmic region $(30 \leq Y^+ \leq 200)$ for all considered cases.

The profiles of the Pseudoplastic lie down those of the Dilatant fluids along the pipe radius, where the decreased flow behavior index induces a noticeable decrease in the RMS of the radial component beyond the buffer region for all Reynolds numbers. It can be said that the increased flow behavior index results in a pronounced enhancement in the transport mechanism of turbulence intensities from the axial velocity fluctuation to the radial ones beyond the buffer region, and this trend is more pronounced as the Reynolds number decreases. As shown in

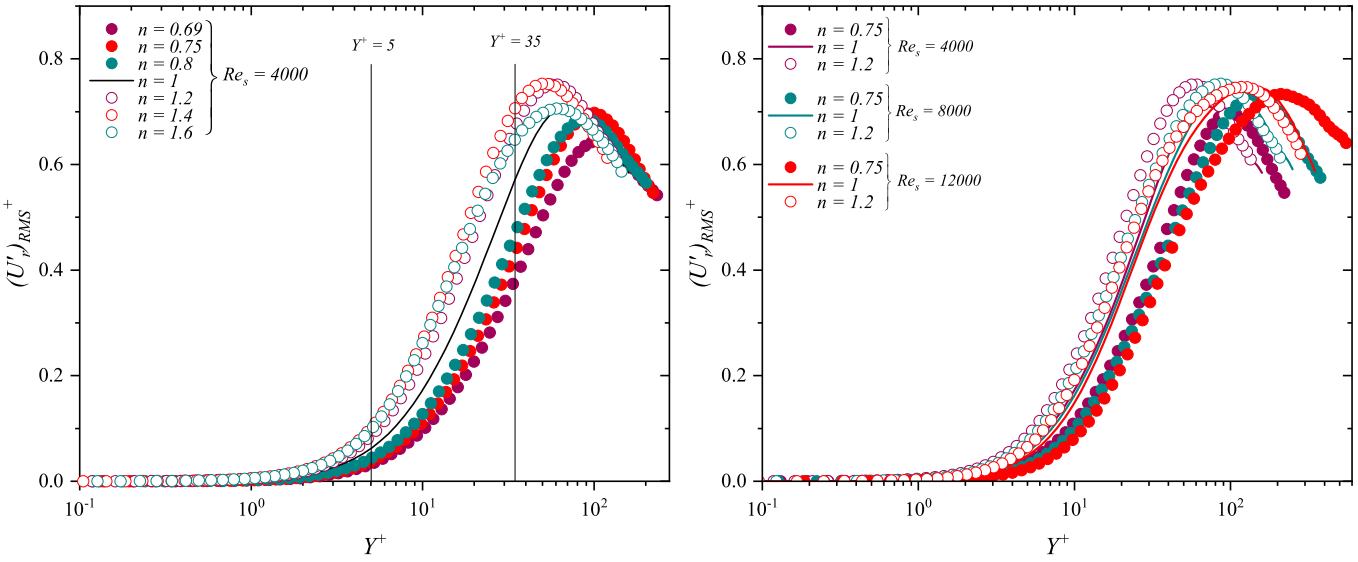

(a) **(b)**

Figure IV.10 – RMS of the radial velocity in LES.

Figure IV.11, the turbulence intensities of the tangential velocity fluctuations of the Dilatant fluids are somewhat higher than the *RMS* profile of the Pseudoplastic fluids along the pipe radius, especially in the buffer region for all Reynolds numbers. The increased flow behavior index results in a pronounced enhancement in the turbulence intensities of the tangential velocity fluctuations along the radial coordinates. This means that the increased flow behavior index induces an apparent enhancement in the transport mechanism of turbulence intensities from the axial velocity fluctuation to the tangential ones beyond the buffer region. This trend is more pronounced as the Reynolds number decreases.

IV.4.1.4 Kinetic energy

Figure IV.12 presents the turbulent kinetic energy of the Pseudoplastic and Dilatant fluids along the pipe radius, versus the distance from the wall in wall units Y^+, over a wide range of flow behavior indices (0.75, 1 and 1.2) for three Reynolds number values (4000, 8000 and 12000). As shown in Figure IV.12, the kinetic energy of turbulent fluctuations shows roughly the same pattern in turbulence intensities of the axial velocity fluctuations. There is no difference between the kinetic energy profiles and they are consistent with each other in the viscous sublayer for all flow behavior indices and Reynolds numbers; these profiles are nearly linear and equal to zero value near-wall region as a result of the absence of the axial, radial, and tangential velocity

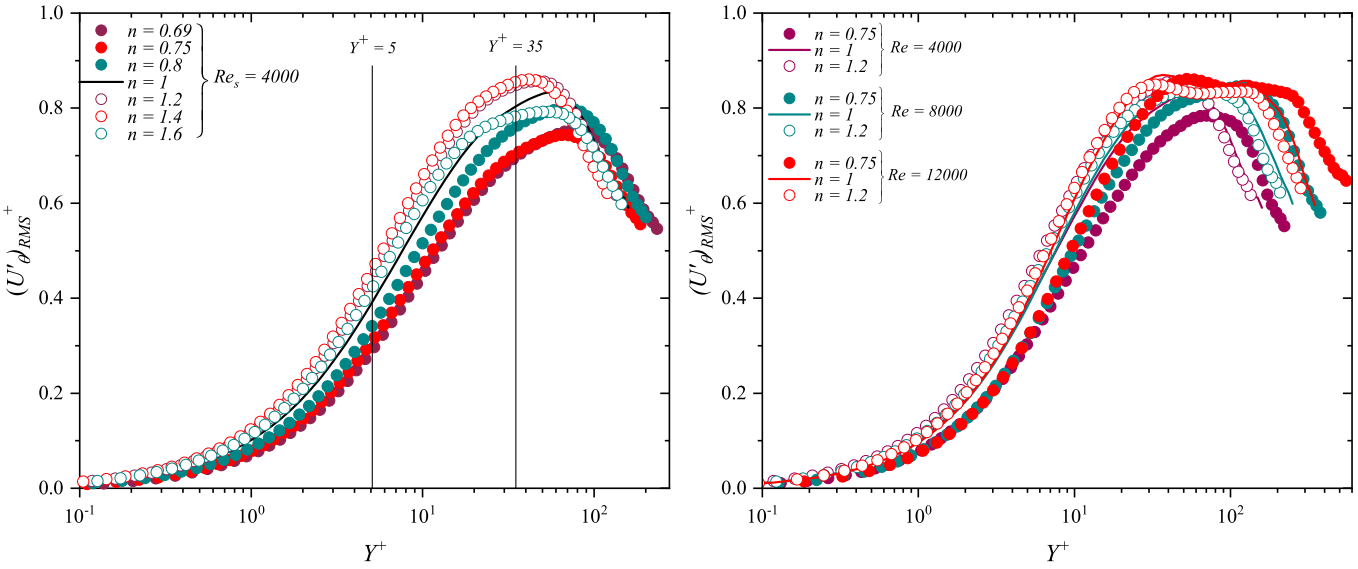

(a) **(b)**

Figure IV.11 – RMS of the tangential velocity in LES.

fluctuations in the wall vicinity. Beyond $Y^+ = 1$, the kinetic energy profiles begin to increase gradually with the wall distance far away from the pipe wall towards the pipe centre as a result of enhancement in the axial velocity fluctuations generation and in the transport of the radial and tangential velocity fluctuations from the axial ones along the pipe radius for all considered cases (Figure IV.9, Figure IV.10 and Figure IV.11). Beyond approximately $(Y^+ = 20)$, the turbulent kinetic energy profiles of the Pseudoplastic and Dilatant fluids reach their peak values; these profiles drop and fall off rapidly to the zero value in the buffer region as a result of the vanish of the axial, radial, and tangential turbulence intensities far away from the pipe wall for all Reynolds numbers. This attenuation is due to the reduction in the generation and transport of the turbulence intensities of the velocity fluctuations, and this trend is more obvious as the Reynolds number decrease.

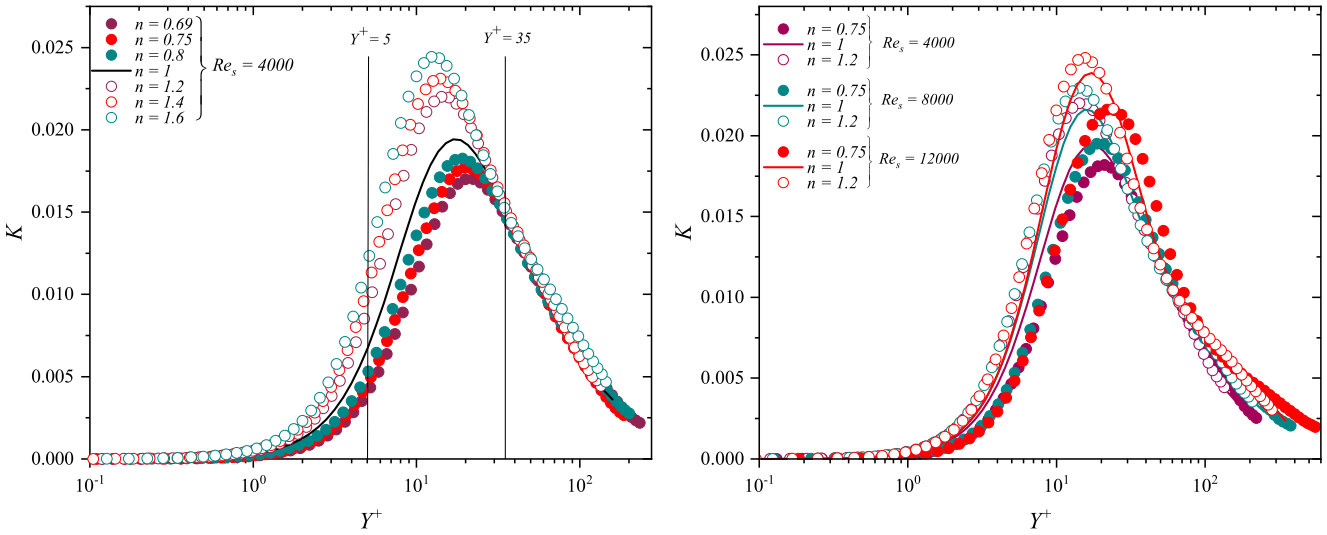

(a) **(b)**

Figure IV.12 – Turbulent kinetic energy.

IV.4.2 Turbulent forced convection of Ostwald de Waele fluids

The subject matter of the present section is that of establishing a better understanding of the rheological and thermal behavior of forced convection turbulent flow of the Ostwald de Waele fluids. Figures IV.13 shows the dimensionless temperature $(\Theta')^+$ distributions of the shear-thinning $(n = 0.75)$ and Newtonian $(n = 1)$ fluids at simulation Reynolds and Prandtl numbers of 4000 and 1, respectively. It should be noted that the dimensionless temperature is the mean temperature $(\Theta = (\langle T_p(z)\rangle - T(\theta, r, z, t))/T_{ref})$ scaled by the friction temperature (T_τ). As shown in the mean axial velocity profiles (Figures IV.6-IV.8), the temperature profiles of shear-thinning and Newtonian fluids are consistent with each other in the viscous sublayer, indicating that the influence of the flow behavior index on the fluid temperature is limited in this flow region. Moreover, there is a clear trend of increase in the temperature profile $(\Theta')^+$ along the radial direction where the temperature profile $(\Theta')^+$ begins to enhance gradually wall with the wall distance far away from the pipe. It can be seen from Figure IV.13 that the profiles of the shear-thinning and Newtonian fluids begin to deviate slightly from each other with the wall distance (Y^+) further away from the pipe wall towards the core region, indicating that the effects of the flow behavior index on the temperature distribution become significant further away from the viscous sublayer, where the temperature profiles are more affected by the flow behavior index in the buffer $(5 \leq Y^+ \leq 30)$ and logarithmic region $(30 \leq Y^+ \leq 200)$.

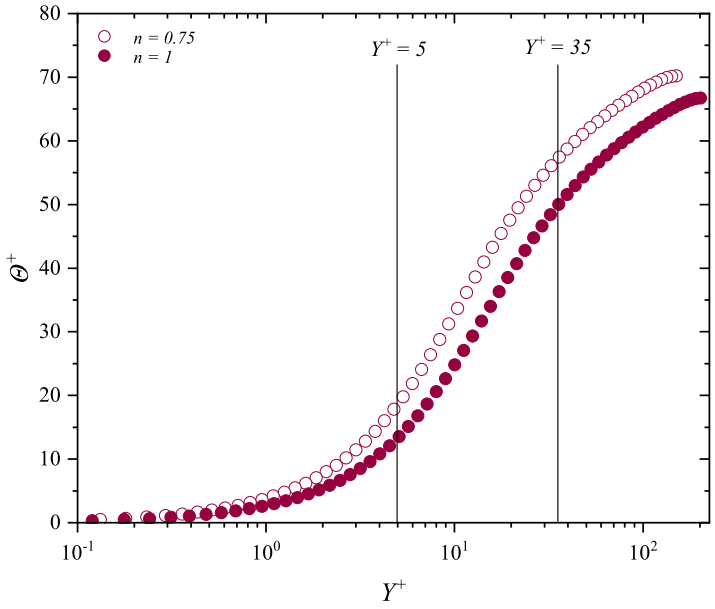

Figure IV.13 – Effect of (n) on the mean temperature profiles.

Figure IV.14 demonstrates the turbulent heat flux of the shear-thinning $(n = 0.75)$ and Newtonian $(n = 1)$ fluids against the distance from the wall (Y^+) in wall units. It is observed that the turbulent axial and radial heat fluxes of shear-thinning fluid behave differently compared to those of a Newtonian fluid. It can be noted that the axial and radial heat fluxes profiles of the shear-thinning and Newtonian fluids are identical and equal to the zero in the viscous sublayer $Y^+ < 1$, which indicates that the absence of the fluctuations in this region where the shear-stress is the dominant force in this region. In turn, these heat flux profiles enhance gradually further away from the wall towards the central region before reaching the peak location. The heat flux components start to damp progressively in the logarithmic region. The axial and radial velocity and temperature fluctuations decrease gradually until they fall off to zero value in the core region. It can be said that the axial velocity and temperature fluctuations generated at the vicinity of the wall exactly in the viscous sublayer and propagated to the logarithmic layer, these fluctuations begin to vanish in the remaining region after reaching their maximum values.

Figure IV.14a shows the turbulent axial heat flux distributions of the shear-thinning and Newtonian fluids, the profiles of the shear-thinning fluids are somewhat larger than those of the Newtonian fluid along the pipe radius, especially in the logarithmic region. It can be said that the decreased flow behavior index (n) induces a slight growth in the axial velocity and the

temperature fluctuations intensity, and consequently, in the turbulent axial heat flux along the radial direction. It is worth noting that the decreased flow behavior index results in an enhancement in the generation of the axial velocity fluctuations and temperature fluctuations along the pipe radius, where the decrease in the flow index also leads to ameliorating the transport of the axial velocity and temperature fluctuations from the wall vicinity towards the core region.

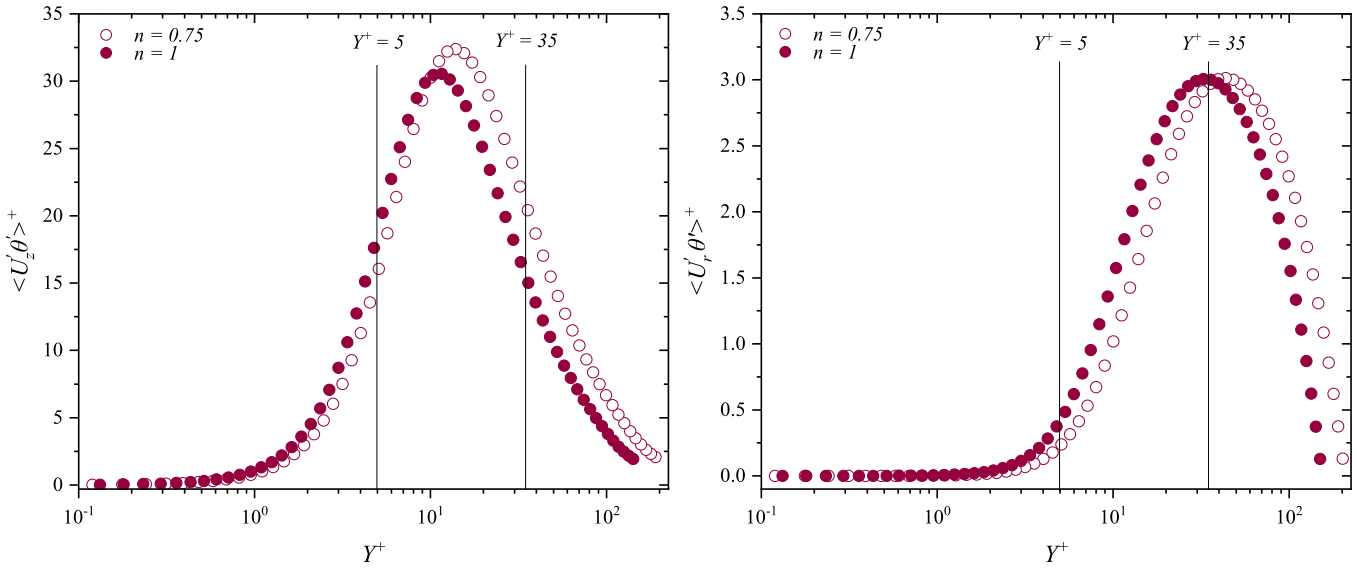

Figure IV.14 – Effect of (n) on the profiles of the turbulent heat flux.

As shown in Figure IV.14b, the radial heat flux profiles begin to deviate from each other further away from the pipe wall with the wall distance ; the radial heat flux of the shear-thinning fluid is somewhat larger than that of the Newtonian fluid along the pipe radius ; this trend is clearer in the logarithmic region. It is worth noting that this deviation is attributed to the influence of the flow behavior index on the radial velocity fluctuations, where the decreasing flow behavior index yields an attenuation in the radial fluctuation which reduces the fluctuations transfer from the axial to the radial velocity fluctuations. The radial fluctuations intensity plays an essential role in the turbulent transport of the momentum and heat transfer between the near-wall layer and the flow core region. The correlations between the axial and wall-normal velocities and between the axial velocity and temperature directly impact the transfer rates of the transported radial turbulent heat flux and turbulent momentum flux via the radial velocity fluctuations.

IV.5 Conclusion

The flow behavior index and Reynolds number were investigated to describe the rheological, hydrodynamic, and thermal behaviors as turbulence features.

The major conclusions of this research will be summarized :

- The decreased flow behavior index and increased Reynolds number markedly increased the shear-rate distributions, resulting in a marked decrease in the Dilatant fluid apparent viscosity for all Reynolds numbers.

- For Pseudoplastic fluid, the decreased flow behavior induced a pronounced increase in the apparent viscosity beyond the buffer region, resulting in a pronounced decrease in the shear-rate along the logarithmic layer. Consequently, this resulted in a noticeable increase in the axial velocity profile in the core region ; this trend was more pronounced as the flow behavior index decreased. On the contrary, the apparent viscosity of the Dilatant fluid decreased gradually beyond the buffer region, resulting in a noticeable increase in the shear-rate over the logarithmic layer and, consequently, this resulted in a pronounced decrease in the turbulent axial velocity profile in the core region ; this trend is more apparent as the flow behavior index increased.

- As for the Reynolds number effects, the increased Reynolds number resulted in a marked decrease in the apparent viscosity, resulting in a noticeable reduction in the shear-rate of the Pseudoplastic fluid and consequently, this resulted in a pronounced increase in the axial velocity profile of the Pseudoplastic fluid in the core region. On the contrary, the increased Reynolds number induced an evident decrease in the apparent viscosity of the Dilatant fluid, resulting in a noticeable increase in the shear-rate and, consequently, a pronounced reduction in the axial velocity profile along the logarithmic region.

- The decreased flow behavior index resulted in a noticeable increase in the turbulence intensities of the axial velocity fluctuations along the buffer region, resulting in a noticeable enhancement in the generation and transport mechanism of turbulence intensities of the velocity fluctuation from the wall vicinity towards the core region. This trend was more pronounced as the Reynolds number increased.

GENERAL CONCLUSION

GENERAL CONCLUSION

The present investigation aimed to examine the influence of the Reynolds number and the flow behavior index on the mean flow characteristics to provide an accurate, complete, and detailed description of the flow patterns and rheological behavior of the Ostwald de Waele fluids with using DNS and LES approaches.

A DNS was carried out to study the fully developed turbulent flow of Pseudoplastic $(n = 0.75)$, Newtonian $(n = 1)$, and Dilatant $(n = 1.2)$ fluids through an isothermal axially cylindrical pipe at a simulation Reynolds number of 6500. The finite difference scheme performed the numerical integration with the second-order accuracy in space and time, and a numerical resolution of $(129 \times 129 \times 193)$ gridpoints in axial, radial, and circumferential directions. The second study reported fully developed turbulent flow forced convection of a thermally independent Ostwald de Waele fluids through a heated cylindrical pipe using LES with an extended Smagorinsky model. This investigation was conducted on various flow behavior indices (0.75, 1 and 1.2) and Reynolds numbers (4000, 8000 and 12000) at a fixed simulation Prandtl number of 1. The numerical resolution was chosen to be 65^3 gridpoints in axial, radial, and circumferential directions, respectively, with a domain length of $20R$ in the axial direction. A uniform heat flux was imposed on the wall as a thermal boundary condition.

The major conclusions of this research will be summarized as follows :

- The DNS results indicated that the streamwise velocity increased gradually from the wall towards the core region with the wall distance with decreasing flow behavior index. The DNS results also suggested that the increased flow behavior index induced a pronounced enhancement in the generation of the axial velocity fluctuations and also led to ameliorating the transport of the axial velocity fluctuations from the wall vicinity towards the core region. On the other hand, the increased flow behavior index ameliorated the transport

mechanism of the radial and tangential velocity fluctuations from the axial velocity fluctuations and the transport from the wall vicinity towards the core region.

- The *LES* results suggested that the decreased flow behavior of Pseudoplastic fluid induced a pronounced increase in the apparent viscosity beyond the buffer region towards the core region, resulting in a pronounced decrease in the shear-rate along the logarithmic region. Consequently, this resulted in a noticeable increase in the axial velocity profile in the core region, and this trend was more pronounced as the flow behavior index decreased. The *LES* results also showed that the increased flow behavior index resulted in a noticeable increase in the axial velocity in the core region, resulting in a marked improvement in the generation and transport mechanism of turbulence intensities of the velocity fluctuation from the wall vicinity towards the core region. This trend was more pronounced as the Reynolds number increased. The decreased flow behavior index resulted in a pronounced suppression in the turbulent kinetic energy along the pipe radius, this attenuation was due to the reduction in the generation and transport of the turbulence intensities of the velocity fluctuations far away from the wall towards the buffer region, and this trend was more obvious as the Reynolds number decreased.

  Our articles of this study are summarizing in the following paragraphs :

- Abdi et al. 2023 [46] performed a numerical analysis of the fully developed turbulent flow of Pseudoplastic and Dilatant fluids in an isothermal stationary pipe using a Large Eddy Simulation, and a conventional dynamic model was presented in this work over a wide range of flow behaviour indices 0.75, 0.8, 1, 1.2, 1.4 and 1.6 at a simulation Reynolds number of 12000.
- Abdi et al. 2023 [47] carried out a *LES* investigation for three simulation Reynolds numbers ($Res = 4000, 8000\ and\ 12000$). The flow behaviour indices used in this research primarily examined Pseudoplastic, Newtonian and Dilatant fluids were 0.75 (shear-thinning), 1 and 1.4 (shear-thickening), respectively.

Further research could also be conducted to describe the rheological behavior of Bingham and Herschel-Bulkley fluids. It is necessary to conduct further studies to understand the effects of the Prandtl and Pearson numbers on the flow pattern and rheological behavior of the Ostwald de Waele fluids.

BIBLIOGRAPHY

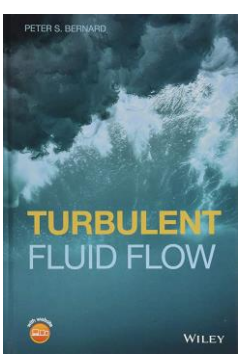

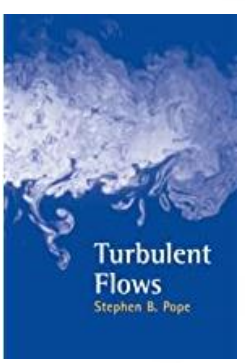

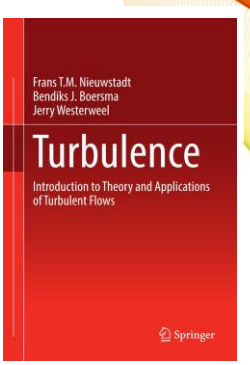

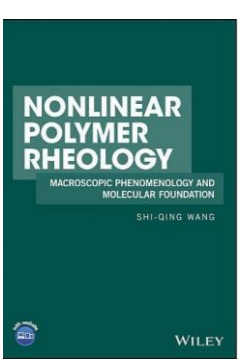

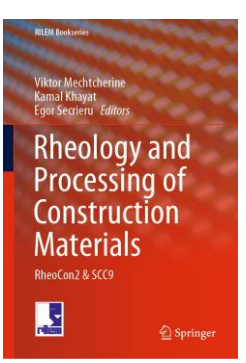

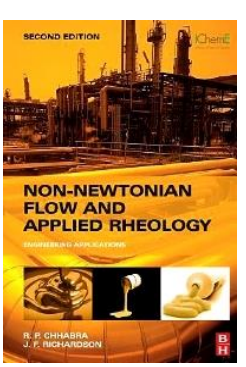


Desalination and Water Treatment
www.deswater.com

Effect of Reynolds number on turbulence characteristics of turbulent Ostwald-de Waele fluids

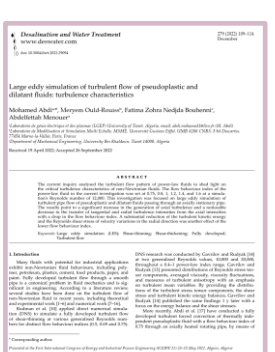
Desalination and Water Treatment
www.deswater.com

Large eddy simulation of turbulent flow of pseudoplastic and dilatant fluids: turbulence characteristics

BIBLIOGRAPHY

[1] HOSSEIN Mirsaeedghazi, Zahra Emam-Djomeh, SMA Mousavi, et al. Rheometric measurement of dough rheological characteristics and factors affecting it. *International Journal of Agriculture and Biology*, 10(1) :112–119, 2008.

[2] Anuj Kumar Sharma, Arun Kumar Tiwari, and Amit Rai Dixit. Rheological behaviour of nanofluids : A review. *Renewable and Sustainable Energy Reviews*, 53 :779–791, 2016.

[3] IHS ESDU 97034 : Non-Newtonian fluids : Guide to classification and characteristics. URL https://www.esdu.com/cgi-bin/ps.pl?sess=unlicensed{_}1200108130610bdj{&}t=doc{&}p=esdu{_}97034a.

[4] Emile Van Den Heever. *Rheological model influence on pipe flow predictions for homogeneous non-Newtonian fluids*. PhD thesis, Cape Peninsula University of Technology, 2013.

[5] Mohamed Abdi. *Simulation numérique à grande échelle (LES) de l'écoulement turbulent pleinement développé d'un fluide non newtonien dans une conduite cylindrique en rotation*. PhD thesis, University of Science and Technology of Oran Mohamed Boudiaf, 2020.

[6] Miroslav Grmela. Multiscale equilibrium and nonequilibrium thermodynamics in chemical engineering. In *Advances in Chemical Engineering*, volume 39, pages 75–129. Elsevier, 2010.

[7] Anthony Harold Peter Skelland. Non-newtonian flow and heat transfer(book on quantitative relationships for non- newtonian systems, considering classification and fluid behavior of materials with anomalous flow properties). *NEW YORK, JOHN WILEY AND SONS, INC., 1967. 469 P*, 1967.

[8] Taha Sochi. Flow of non-newtonian fluids in porous media. *Journal of Polymer Science Part B : Polymer Physics*, 48(23) :2437–2767, 2010.

[9] Fridtjov Irgens. *Rheology and non-newtonian fluids*, volume 1. Springer, 2014.

[10] Malvern Instruments. A basic introduction to rheology. *Malvern Instruments Limited : Worcestershire, UK*, 2016.

[11] Christophe Ancey. Introduction to fluid rheology. *LHE École Polytechnique Fédérale de Lausanne*, 2005.

[12] Amir A Aliabadi. Introduction to modelling and simulation. In *Turbulence : A Fundamental Approach for Scientists and Engineers*, pages 191–194. Springer, 2022.

[13] Ulka Gaitonde, Y Gong, and FX Tanner. Quality criteria for large eddy simulation. *First Year Transfer Report, School of MACE, University of Manchester*, 2008.

[14] SA Thorpe. Transitional phenomena and the development of turbulence in stratified fluids : A review. *Journal of Geophysical Research : Oceans*, 92(C5) :5231–5248, 1987.

[15] Kemal Hanjalić and Brian Launder. *Modelling Turbulence in Engineering and the Environment : Rational Alternative Routes to Closure*. Cambridge University Press, 2022.

[16] Eugene De Villiers. The potential of large eddy simulation for the modeling of wall bounded flows. *Imperial College of Science, Technology and Medicine*, 2006.

[17] Peter A Davidson, Yukio Kaneda, and Katepalli R Sreenivasan. *Ten chapters in turbulence*. Cambridge University Press, 2012.

[18] Peter Alan Davidson. *Turbulence in rotating, stratified and electrically conducting fluids*. Cambridge University Press, 2013.

[19] Matthew T Pittard. *Large eddy simulation based turbulent flow-induced vibration of fully developed pipe flow*. Brigham Young University, 2003.

[20] Václav Uruba. Turbulence handbook for experimental fluid mechanics professionals. *Skovlunde : Dantec Dynamic*, 2012.

[21] Pierre Sagaut and Claude Cambon. *Homogeneous turbulence dynamics*, volume 10. Springer, 2008.

[22] Pierre Sagaut, Marc Terracol, and Sebastien Deck. *Multiscale and multiresolution approaches in turbulence-LES, DES and Hybrid RANS/LES Methods : Applications and Guidelines*. World Scientific, 2013.

[23] J Singh, M Rudman, and HM Blackburn. The influence of shear-dependent rheology on turbulent pipe flow. *Journal of Fluid Mechanics*, 822 :848–879, 2017.

[24] Günther Grötzbach. Spatial resolution requirements for direct numerical simulation of the rayleigh-bénard convection. *Journal of computational physics*, 49(2) :241–264, 1983.

[25] PS Gnambode, P Orlandi, Meryem Ould-Rouiss, and Xavier Nicolas. Large-eddy simulation of turbulent pipe flow of power-law fluids. *International Journal of Heat and Fluid Flow*, 54 : 196–210, 2015.

[26] Donald Matos and Cristian Valerio. *Fluid Mechanics and Pipe Flow : Turbulence, Simulation and Dynamics*. Nova Science Publishers, Incorporated, 2009.

[27] Volker John. *Large eddy simulation of turbulent incompressible flows : analytical and numerical results for a class of LES models*, volume 34. Springer Science & Business Media, 2003.

[28] Marcel Lesieur. Introduction to turbulence in fluid mechanics. *Turbulence in Fluids : Fourth Revised and Enlarged Edition*, pages 1–23, 2008.

[29] Patrick Loulou, Robert D Moser, Nagi N Mansour, and Brian J Cantwell. Direct numerical simulation of incompressible pipe flow using a b-spline spectral method. Technical report, 1997.

[30] Murray Rudman and Hugh M Blackburn. Large eddy simulation of turbulent pipe flow. In *Second International Conference o CFD in the Minerals and Process Industries CSIRO, Melbourne, Australia*, pages 6–8, 1999.

[31] Kenji Nishibori, Koji Kikuyama, and Mitsukiyo Murakami. Laminarization of turbulent flow in the inlet region of an axially rotating pipe : fluids engineering. *JSME International journal*, 30 (260) :255–262, 1987.

[32] MR Malin and BA Younis. The prediction of turbulent transport in an axially rotating pipe. *International communications in heat and mass transfer*, 24(1) :89–98, 1997.

[33] AA Feiz, M Ould-Rouis, and Guy Lauriat. Large eddy simulation of turbulent flow in a rotating pipe. *International journal of heat and fluid flow*, 24(3) :412–420, 2003.

[34] Takashi Ohta and Masahito Miyashita. Dns and les with an extended smagorinsky model for wall turbulence in non-newtonian viscous fluids. *Journal of Non-Newtonian Fluid Mechanics*, 206 : 29–39, 2014.

[35] Jacobus Gerardus Maria Eggels. Direct and large eddy simulation of turbulent flow in a cylindrical pipe geometry. 1995.

[36] DW Dodge and AB Metzner. Turbulent flow of non-newtonian systems. *AIChE journal*, 5(2) : 189–204, 1959.

[37] Andrey A Gavrilov and Valeriy Ya Rudyak. Reynolds-averaged modeling of turbulent flows of power-law fluids. *Journal of Non-Newtonian Fluid Mechanics*, 227 :45–55, 2016.

[38] DC Bogue and AB Metzner. Velocity profiles in turbulent pipe flow. newtonian and non-newtonian fluids. *Industrial & Engineering Chemistry Fundamentals*, 2(2) :143–149, 1963.

[39] MR Malin. Turbulent pipe flow of power-law fluids. *International communications in heat and mass transfer*, 24(7) :977–988, 1997.

[40] MR Malin. Turbulent pipe flow of herschel-bulkley fluids. *International communications in heat and mass transfer*, 25(3) :321–330, 1998.

[41] AA Gavrilov and V Ya Rudyak. Direct numerical simulation of the turbulent energy balance and the shear stresses in power-law fluid flows in pipes. *Fluid Dynamics*, 52 :363–374, 2017.

[42] Mohamed Abdi, Meryem Ould-Rouiss, and Abdelkader Noureddine. Les of turbulent flow of the non-newtonian fluid : The mean flow quantities. In *The First International Conference on Materials, Environment, Mechanical and Industrial Systems, ICMEMIS'19*, 2019.

[43] JGM Eggels, F Unger, MH Weiss, J Westerweel, RJ Adrian, R Friedrich, and FTM Nieuwstadt. Fully developed turbulent pipe flow : a comparison between direct numerical simulation and experiment. *Journal of Fluid Mechanics*, 268 :175–210, 1994.

[44] Lotfi Redjem Saad. *Simulations numériques des transferts de chaleur turbulents par convection forcée dans des conduites cylindriques et des espaces annulaires.* PhD thesis, 2008. URL http://www.theses.fr/2008PEST0234/document.

[45] Murray Rudman, Hugh Maurice Blackburn, Lachlan JW Graham, and L Pullum. Turbulent pipe flow of shear-thinning fluids. *Journal of non-newtonian fluid mechanics*, 118(1) :33–48, 2004.

[46] Mohamed Abdi, Meryem Ould-Rouiss, Fatima Zohra Nedjda Bouhenni, and Abdelfettah Menouer. Large eddy simulation of turbulent flow of pseudoplastic and dilatant fluids : turbulence characteristics. *DESALINATION AND WATER TREATMENT*, 279 :109–114, 2022.

[47] Mohamed Abdi, Meryem Ould-Rouiss, Lalia Abir Bouhenni, Nour Elhouda Beladjine, and Belhouari Abdelkarim Bekhtaoui. Effect of reynolds number on turbulence characteristics of turbulent ostwald-de waele fluids. *DESALINATION AND WATER TREATMENT*, 279 :173–177, 2022.